ANALYSIS OF FUNCTIONAL NEAR INFRARED SPECTROSCOPY SIGNALS

by

Ceyhun Burak Akgül

B.S., Electrical and Electronics Engineering, Boğaziçi University, 2002

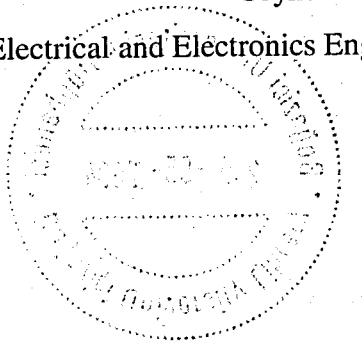

Submitted to the Institute for Graduate Studies in
Science and Engineering in partial fulfillment of
the requirements for the degree of
Master of Science

Bogazici University Library

39001102161992

Graduate Program in Electrical and Electronics Engineering

Boğaziçi University

2004

To My Family

To Lumina Mea

ACKNOWLEDGEMENTS

I am grateful to Prof. Bülent Sankur for not only being my thesis supervisor but also for his wisdom he never kept away from me. We share the credits equally for having brought such a work to light. One should regret a lot, if he or she didn't get the chance to acquaint with his academic and intellectual knowledge.

I would like to thank Dr. Ata Akın for introducing me to cognitive neuroscience and for constantly encouraging me throughout the thesis work. His ability to bridge the gaps between signal processing and the physiology of the human brain have made this work sound and strong.

I would like to thank my mother, my father and my sister thousands of times for everything. I hope I deserve to claim their name.

I would like to thank one last person, for she always was and will be with me.

ABSTRACT

ANALYSIS OF
FUNCTIONAL NEAR INFRARED SPECTROSCOPY SIGNALS

In recent years, positron emission tomography (PET) and functional magnetic resonance imaging (fMRI) have facilitated the monitoring of the human brain non-invasively, during functional activity. Nevertheless, the use of these systems remain limited since they are expensive, they cannot provide sufficient temporal detail and they are not very comfortable for the patient or the volunteer whose brain is monitored. Functional near infrared spectroscopy (fNIRS), on the other hand, is an emerging non-invasive modality which may be a remedy for the failures of the existing technologies. However, properly designed data analysis schemes for fNIRS have been missing. In this M.S. thesis, we intend to introduce a collection of signal processing methods in order to treat fNIRS data acquired during functional activity of the human brain. Along extensive hypothesis tests that characterized the statistical properties of the empirical data, we have described the signals in the time-frequency plane and partitioned the signal spectrum into several dissimilar subbands using an hierarchical clustering procedure. The proposed subband partitioning scheme is original and can easily be applied to signals other than fNIRS. In addition to these, we have adapted two different exploratory data analysis tools, namely, independent component analysis (ICA) and waveform clustering, to fNIRS short-time signals in order to learn generic cognitive activity-related waveforms, which are the counterparts of the brain hemodynamic response in fMRI. The periodicity analysis of the signals in the 30-250 mHz range validates that fNIRS measures indeed functional cognitive activity. Furthermore, as extensive ICA and waveform clustering experiments put into evidence, cognitive activity measured by fNIRS, reveals itself in a way very similar to the one measured by fMRI. These findings indicate that, in the near future, fNIRS shall play a more important role in explaining cognitive activity of the human brain.

ÖZET

YAKIN KIZILÖTESİ SPEKTROSKOPİ İŞARETLERİNİN ANALİZİ

Geçtiğimiz yıllarda, pozitron yayınımı tomografisi (PET) ve işlevsel manyetik rezonans görüntüleme (fMRI), insan beyninin işlevsel etkinlik sırasında gözlenmesini kolaylaştırmıştır. Yine de, pahalı olmaları, yeterince zamansal çözünürlük sağlayamamaları ve beyni gözlenen hasta ya da gönüllü için yeterince rahat olmamaları nedeniyle bu sistemlerin kullanımı sınırlı kalmıştır. Diğer yandan, işlevsel yakın kızılötesi spektroskopi (fNIRS), varolan teknolojilerin yetersizliklerine çözüm olabilecek bir yöntem olarak ortaya çıkmaktadır. Ne var ki, fNIRS için tasarlanmış veri analizi yöntemlerinin eksikliği çekilmektedir. Bu yüksek lisans tezinde, insan beyninin işlevsel etkinliği sırasında alınan fNIRS verilerine yönelik bir işaret işleme yöntemleri bütününün ortaya çıkarılması amaçlanmaktadır. Deneysel verilerin istatistiksel özelliklerini nitelendirmek için yapılan kapsamlı testlerin yanı sıra, işaretler zaman-frekans düzleminde betimlenmiş ve işaret spektrumu, sıradüzensel topaklandırma kullanılarak, birbirlerinden farklı altbantlara bölünmüştür. Önerilen alt bantlara ayırma yöntemi özgündür ve fNIRS işaretlerinden farklı işaretlere de kolaylıkla uygulanabilir. Bunlara ek olarak, fMRI yöntemindeki beyin hemodinamik yanıtının karşılığı olan bilişsel etkinlik-ilişkili dalga biçimlerini öğrenmek için, bağımsız bileşenler analizi (BBA) ve dalga biçimi topaklandırma gibi iki ayrı açınsayıcı veri analizi aracı kısa-zamanlı fNIRS işaretlerine uygulanmıştır. İşaretlerin 30-250 mHz frekans aralığındaki dönemlilik analizi, fNIRS'nin gerçekten de işlevsel etkinliği ölçtüğünü geçerlemektedir. Bununla birlikte, kapsamlı BBA ve dalga biçimi topaklandırma deneylerinin ortaya koyduğu üzere, fNIRS tarafından ölçülen bilişsel etkinlik, fMRI'de ölçülene çok benzer bir şekilde ortaya çıkmaktadır. Bu bulgular, fNIRS yönteminin yakın bir gelecekte insan beyninin bilişsel etkinliğinin açıklanmasında şu andakinden daha önemli bir rol oynayacağını göstermektedir.

TABLE OF CONTENTS

LIST OF FIGURES

LIST OF TABLES

LIST OF SYMBOLS / ABBREVIATIONS

$\mathbf{A}$	Mixing matrix
$\mathbf{a}_i$	i^{th} column of the mixing matrix $\mathbf{A}$ or the i^{th} ICA basis vector
$B_n(t,f)$	Power spectral density at the n^{th} frequency band as a function of time t
C	Concentration *-first use*
C	Number of clusters *-second use*
C_{in}	Count of the periodicities inside the expected range
C_{out}	Count of the periodicities outside the expected range
$d(Q_c, Q_l)$	Distance between clusters Q_c and Q_l
E	Weighted energy of the signal $x(t)$
F_s	Sampling frequency
$\mathbf{h}$	Vector notation of $h(t)$
$\mathbf{h}_o$	Optimal Gamma fit
$h(t)$	Brain hemodynamic response modeled as Gamma function
H_0	Null hypothesis
H_1	Alternative hypothesis
$I_L(\lambda)$	Transmitted light intensity at wavelength λ
$I_n(t)$	Signal power at the n^{th} frequency band as a function of time t
$I(t)$	Total signal power as a function of time t
I_0	Weighted energy of the signal $x_0(t)$
$I_0(\lambda)$	Incident light intensity at wavelength λ
$J_{QoC}(C)$	Quality of clustering index as a function of the number of clusters C
$J_1(P_0)$	Least-square periodicity estimation functional as a function of period P_0
$K(\lambda)$	Pathlength correction factor as a function wavelength λ
L	Length of the path that the light travels in the brain tissue
m	Dimensionality of the vectors $\mathbf{x}$
n	Dimensionality of the vectors $\mathbf{s}$, dimensionality of the vectors $\mathbf{y}$ or the number of estimated ICA basis vectors

$OD(\lambda)$	Optical density at wavelength λ
p	False alarm probability of the hypothesis test
P	Fishers's combined test-statistic
$\overline{P}_{detectors}(j)$	Mean inside periodicity for the j^{th} subject averaged over photodetectors
$\overline{P}_{subjects}(k)$	Mean inside periodicity for the k^{th} photodetector averaged over subjects
$\hat{P}_0$	Period estimate
Q	Set of clusters
$\mathbf{q}_c$	Centroid of the cluster Q_c
Q_c	c^{th} Cluster
Q^m	Set of centroidal relative power time-series for the the m^{th} signal
R^m	Set of relative power time-series for the m^{th} signal
$\mathbf{R}_n^m$	$R_n^m(t)$ in vector form
$R_n^m(t)$	Time-series of the relative power for the n^{th} band of the m^{th} signal
$R_n(t)$	Time-series of the relative power at the n^{th} frequency band
$\mathbf{s}$	Independent component vector
S_{in}	Cumulative score of the periodicities inside the expected range
$s_{k_0}^{j_0}(t)$	HbO_2 signal from subject j_0, photodetector k_0
S_{out}	Cumulative score of the periodicities outside the expected range
$S(Q_c)$	Within-cluster distance for cluster Q_c
$s(t)$	A generic HbO_2 signal
$S(\tau, f)$	Short-time Fourier transform of a HbO_2 signal
T	Estimated delay in response to target stimulus
T_s	Sampling period
$\mathbf{x}$	A generic m-dimensional data vector consisting of sequential HbO_2 samples
X	A generic dataset that consists of multiple realizations of $\mathbf{x}$
X^{j_0}	All the vectors from Γ^{j_0}
$X_{k_0}^{j_0}$	All the vectors from signal $s_{k_0}^{j_0}(t)$
$\mathbf{x}_{k_0}^{j_0}(i)$	A HbO_2 vector from the signal $s_{k_0}^{j_0}(t)$, target location i

$X_{left}^{j_0}$	All the vectors from *left* photodetectors of subject j_0
$X_{mid-left}^{j_0}$	All the vectors from *mid-left* photodetectors of subject j_0
$X_{mid-right}^{j_0}$	All the vectors from *mid-right* photodetectors of subject j_0
$X_{right}^{j_0}$	All the vectors from *right* photodetectors of subject j_0
X_{k_0}	All the vectors from Γ_{k_0}
$x(t)$	Filtered version of a generic HbO_2 signal
$x_0(t)$	Periodic component of the signal $x(t)$
Y	Cubic B-spline representation of X
$\mathbf{y}(i)$	Cubic B-spline representation of $\mathbf{x}(i)$
α	Significance level of the hypothesis test
γ	Critical value of the hypothesis test
Γ	All the HbO_2 signals in the dataset
Γ^{j_0}	All the HbO_2 signals from a given subject j_0
Γ_{k_0}	All the HbO_2 signals from a given photodetector k_0
Δf	Frequency sampling of the time-frequency representation
$\Delta[Hb]$	Change in the concentration of deoxygenated hemoglobin
$\Delta[HbO_2]$	Change in the concentration of oxygenated hemoglobin
Δt	Time resolution of the time-frequency representation
$\varepsilon(\lambda)$	Absorption coefficient as a function of wavelength λ
κ	Kurtosis (time or ensemble average)
λ	Wavelength *-first use*
λ	Regularization parameter *-second use*
μ	Mean (time or ensemble average)
ξ	An hypothesis test-statistic
$\overline{\rho}_{pq}$	Averaged normalized correlation coefficient between the bands p and q
σ^2	Variance (time or ensemble average)
τ	Skewness (time or ensemble average) *-first use*
τ	Time-constant of the Gamma function *-second use*

BHR	Brain Hemodynamic Response
BOLD	Blood Oxygen Level Dependent
cdf	cumulative distribution function
CLT	Central Limit Theorem
DFT	Discrete Fourier Transform
ecdf	empirical cumulative distribution function
ECM	Expectation Conditional Maximization
EEG	Electroencephalogram
fMRI	Functional Magnetic Resonance Imaging
fNIRS	Functional Near Infrared Spectroscopy
HbO_2	Oxygenated Hemoglobin
HbR	Deoxygenated Hemoglobin
HF	High Frequency
J-B	Jarque-Bera
ICA	Independent Component Analysis
i.i.d.	independent identically distributed
ITI	Inter-Target Interval
K-S	Kolmogorov-Smirnov
LF	Low Frequency
LSPE	Least-Square Periodicity Estimation
MSE	Mean-Squared Error
PCA	Principal Component Analysis
PET	Positron Emission Tomography
SOM	Self-Organizing Map
STFT	Short-Time Fourier Transform
TCDS	Transcranial Doppler Sonography
TFR	Time-Frequency Representation
VLF	Very Low Frequency
WFT	Windowed Fourier Transform

1. INTRODUCTION

Cognitive neuroscience is the study of the human mind which is able to perfom a variety of tasks including simple ones such as perceiving a color and much more sophisticated ones as learning, recall and love. Rather than being reserved as a singular discipline, cognitive neuroscience borrows questions from pyschology, psychiatry, linguistics or arts and tries to answer them. The abstract concept of mind links to physical reality by the organ we call brain. The latter is maybe the most complex system we know. Its capabilities as well as its disfunctions have consequences which are scaled by its complexity for both the individual and the society.

Excluding studies in special subject populations such as neurological patients and children with developmental disoders, cognitive neuroscientists use computer-based experimental procedures in healthy adult volunteers in order to explore the brain responses to a variety of stimulated cognitive tasks [1]. The advents of positron emission tomography (PET) and functional magnetic resonance imaging (fMRI) boosted the interest in cognitive neuroscience since people in the field can now collect data associated with the human brain function [2]. PET and fMRI together constitute established functional neuroimaging modalities. They greatly facilitated studies in localizing various brain areas responsible of attention, perception, language processing and generation, memory mechanisms and emotions [3]. A recent technique in the field is the functional near infrared spectroscopy (fNIRS) which has its own advantages and disadvantages compared to PET or fMRI and yet is in the process of clinical validation [2, 4, 5]. Nevertheless, fNIRS is a promising brain monitoring modality and constitutes the source of this thesis. The current work attempts to propose a general framework in treating fNIRS data from a signal processing perspective.

In this introductory chapter, the two functional neuroimaging techniques PET and fMRI are briefly reviewed (Section 1.1) and essential ideas and motivation behind fNIRS study is exposed (Sections 1.2 and 1.3). The final section of this chapter is devoted to what is covered in the thesis report.

1.1. Functional Neuroimaging Techniques

PET and fMRI are classified as indirect methods in assessing the human brain function since they rely on some hemodynamic changes, such as the changes in cerebral blood flow, cerebral blood volume or availability of oxygen, which are consequent to neuronal activity. They are both non-invasive in that the recordings are done through the intact human scalp.

PET uses different isotopes to determine the physiological parameters of cerebral blood flow and cerebral blood volume. It has the advantage of allowing the calibration of the physiological variables in terms of absolute physical quantities such as metabolic rates in milligram of a substance consumed per minute per unit volume of tissue. The main disadvantage is reliance on radioactivity [3].

The way fMRI monitors changes in local brain activity is by measuring signals that depend on the differential magnetic properties of oxygenated and deoxygenated hemoglobin, termed as the blood oxygen level dependent (BOLD) signal. The latter gives a measure of changes in oxygen availability [3]. Since magnetic resonance images reveal excellent anatomical detail, particularly of soft tissues, it is possible to generate functional activity maps with good spatial resolution through the assessment of the BOLD signal.

How do we relate the physiological quantities measured by PET or fMRI with the brain function or specifically to say with the neuronal activity? The answer lies in the energy metabolism of the brain. In simple terms, the latter requires a steady supply of oxygen that metabolizes glucose to provide energy. The demand for glucose and oxygen by neuronal tissues, which may be more pronounced in a particular brain region due to a particular cognitive task at a particular time, is responded by the increase in cerebral blood flow to this localized brain region. Similarly, another good indicator of oxygen availability is the quantity of hemoglobin which is the physiological component responsible of oxygen transport. Accordingly, these hemodynamic changes, i.e., the changes in cerebral blood volume, cerebral blood flow, deoxyhemoglobin (HbR) or oxyhemoglobin (HbO_2), enable us to measure the functional brain activity indirectly.

1.2. Functional Near Infrared Spectroscopy

Functional near infrared spectroscopy is the assessment of physiological changes associated with brain activity by exploiting the optical properties of the brain tissue. Near infrared light in the range of 650-950 nm can pass through the skull and reach the cerebral cortex up to a depth of 3 cm (see Figure 1.1 (a)) [2, 6]. It is weakly absorbed by the tissue and at variable amounts by HbR and HbO_2 depending on the concentration levels of these agents. Basically due to the significant difference in the near infrared light absorption spectra of HbR and HbO_2 (see Figure 1.1 (b)), it is possible to compute the changes in their concentration levels using the intensity of detected light.

The concentrations of HbR and HbO_2 can be computed using the modified Beer-Lambert law [4, 5]. Consider an ideal setting where the concentration of a light absorbing component in a non-absorbing medium is C. The incident light, with intensity I_0 and wavelength λ, travels a distance L in this medium. The ordinary Beer-Lambert law yields the intensity I_L of the transmitted light as a function of the wavelength λ by

$$I_L = I_0 e^{-\varepsilon(\lambda)CL} \tag{1.1}$$

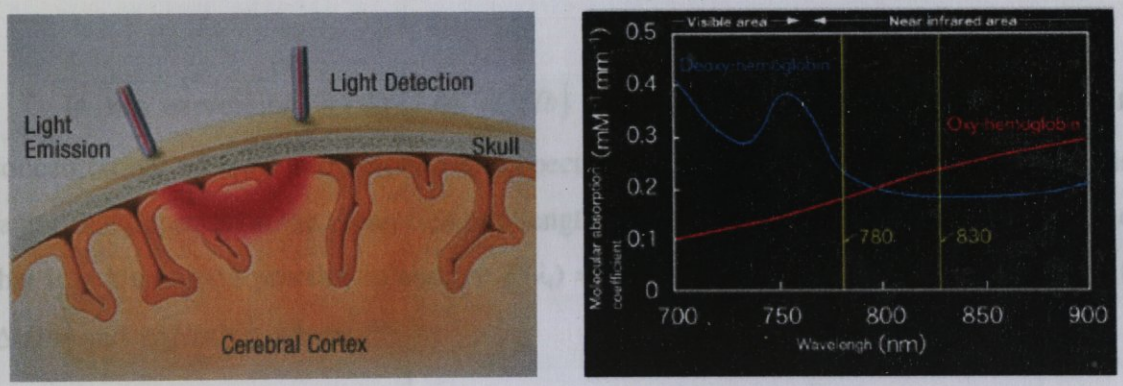

(a) (b)

Figure 1.1. (a) The principle of near infared spectroscopy (b) Light absorption spectra of HbR and HbO_2 in the near infrared range

[From http://www.hitachimed.com/products/optical_measurement.asp]

where $\varepsilon(\lambda)$ is the absorption coefficient of the component at wavelength λ. If we somehow are able to measure the optical density of the medium at wavelength λ during the process, we can then compute the concentration C of the absorbing component by using the following relation

$$OD(\lambda) = \log(I_0 / I_L) = \varepsilon(\lambda) CL \tag{1.2}$$

where $OD(\lambda)$ is the measured optical density. In case there are multiple absorbing components, the relation (1.2) can be exploited using light at multiple wavelengths. This observation leads to the application of modified Beer-Lambert law in order to measure the change in the concentrations of two absorbing physiological components *HbR* and HbO_2 present in the brain tissue which is a nearly non-absorbing medium as far as considered wavelengths lie within the near-infrared range. Suppose that we have measured the optical densities of a particular brain region at wavelengths λ_1 and λ_2. Neglecting the amount of the light absorbed by components other than *HbR* and HbO_2, (1.2) can be generalized one step further into

$$OD(\lambda_1) = \left\{ \varepsilon_{Hb}(\lambda_1) \Delta[Hb] + \varepsilon_{HbO_2}(\lambda_1) \Delta[HbO_2] \right\} K(\lambda_1) \tag{1.3}$$

$$OD(\lambda_2) = \left\{ \varepsilon_{Hb}(\lambda_2) \Delta[Hb] + \varepsilon_{HbO_2}(\lambda_2) \Delta[HbO_2] \right\} K(\lambda_2) \tag{1.4}$$

In the expressions (1.3)-(1.4), $\Delta[Hb]$ and $\Delta[HbO_2]$ denote the changes in the concentrations of *HbR* and HbO_2 with respect to their initial levels and $K(\lambda_i)$, $i = 1, 2$ is a factor that depends on the mean free pathlength traveled by the light at wavelength λ_i, note that it is a common practice to assume $K(\lambda_i) = K$ for $i = 1, 2$. Solving these equations for $\Delta[Hb]$ and $\Delta[HbO_2]$, we get

$$\Delta[Hb] = \frac{OD(\lambda_1) - \dfrac{\varepsilon_{HbO_2}(\lambda_1)}{\varepsilon_{HbO_2}(\lambda_2)} OD(\lambda_2)}{K\left[\varepsilon_{Hb}(\lambda_1) - \varepsilon_{Hb}(\lambda_2) \dfrac{\varepsilon_{HbO_2}(\lambda_1)}{\varepsilon_{HbO_2}(\lambda_2)} \right]} \tag{1.5}$$

$$\Delta[HbO_2] = \frac{OD(\lambda_1) - \frac{\varepsilon_{Hb}(\lambda_1)}{\varepsilon_{Hb}(\lambda_2)} OD(\lambda_2)}{K\left[\varepsilon_{HbO_2}(\lambda_1) - \varepsilon_{HbO_2}(\lambda_2)\frac{\varepsilon_{Hb}(\lambda_1)}{\varepsilon_{Hb}(\lambda_2)}\right]} \tag{1.6}$$

Once the changes in the concentrations of HbR and HbO_2 are determined, other quantities of physiological relevance, such as total blood volume change $\Delta[BV]$ and oxygenation $\Delta[O_2]$, can be deduced through the following equations

$$\Delta[BV] = \Delta[Hb] + \Delta[HbO_2] \tag{1.7}$$

$$\Delta[O_2] = \Delta[HbO_2] - \Delta[Hb] \tag{1.8}$$

A typical fNIRS device consists of light sources and photodetectors together with additional units: a transmitter circuit that controls the timing and intensity of light sources, a receiver circuit that collects reflected light from tissues and sends it to the control unit which is responsible of the synchronized operation of the whole system. Three distinct fNIRS measurement methods are available: continuous wave, frequency domain and time-resolved. Continuous wave fNIRS devices, in particular, are prefered for neuroimaging /brain monitoring studies [2].

The continuous wave principle is relatively simple. Each source brightens a particular brain region by emitting light at (at least two) different wavelengths, e.g. 730 nm and 850 nm, on a timely basis. Reflected photons are integrated at corresponding photodetectors that convert the received light intensity into electrical signals out of which optical density signals are derived. Using two such signals, known absorption coefficients and the pathlength factor K, $\Delta[Hb]$ and $\Delta[HbO_2]$ time-series can be calculated through equations (1.5) and (1.6).

1.3. Motivation behind fNIRS Study

In order to rationalize the use of the fNIRS technique in neuroimaging applications, we certainly have to refer to its similarities with the fMRI. Driving point is based on the observation that both modality, although in much different ways, measure a correlate of oxygen availability in a particular brain region. It is an established fact that a reduction in *HbR* concentration increases the BOLD signal of fMRI [7]. On the other hand, using the modified Beer-Lambert law, one can obtain the changes in the concentrations of *HbR* and HbO_2 from raw fNIRS measurements. Hence it would not be unwise to conjecture that there should exist some correlation between the hemoglobin signals (*HbR* and HbO_2) obtained using fNIRS and the fMRI-BOLD signal if we were able to perform simultaneous recordings in both modality. Hopefully, this conjecture turns out to be a truth demonstrated in a recent study [8], i.e., simultaneous BOLD and fNIRS recordings do exhibit strong correlations indeed. Accordingly, the problems associated with the analysis of fNIRS time-series happen to be very similar to those encountered in fMRI.

Let us now turn our attention to computer aided experiments during which the brain of a human subject is monitored by an fMRI device. The objective of such an experiment consists of measuring the BOLD responses in each of the 3D brain volumes, or voxels, fMRI. The human subject is supposed to respond to a series of stimuli which is carefully designed in order to study a particular brain system (e.g. memory, language, vision) [9]. The measured BOLD responses are localized, i.e., associated with a particular voxel, and hence can be used to generate functional activity maps of the human brain as shown in Figure 1.2 [10]. Quantification of BOLD responses is formalized under the name of *activity detection* since the end goal is to retrieve information concerning neuronal activity stimulated by cognitive or behavioural tasks [11]. Activity detection constitutes one of the two major problems in fMRI data analysis and is strongly related to the other, namely *the estimation of the brain hemodynamic response* (BHR) *function.*

The most basic assumption in fMRI data analysis is that there should be some correlation between sensory stimulus, usually called *stimulus paradigm* or *onsets*, and the acquired fMRI time-series. At the early stages, the fMRI problem was solely defined as to

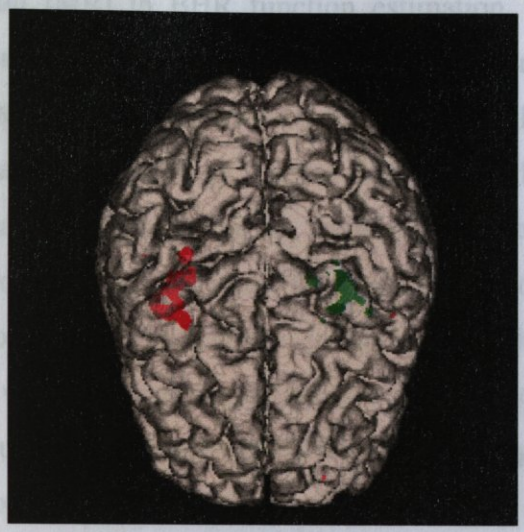

Figure 1.2. A fMRI activity map that results from an experiment involving hand movement: areas active during right hand movement (green) and areas active during left hand movement (red) [From http://www.imt.liu.se/mi/Research/fMRI/]

detect significant activation regions assuming a linear system modeling "the neural channel" which delays and disperses the sensory input [10], i.e., the latter is reflected to fMRI-BOLD response after being reshaped by the BHR function which stands for the impulse response of "the neural channel". This assertion follows from neurovascular coupling according to which hemodynamic events, such as the BOLD response, have time scales of several seconds whereas neuronal events, which are fired by sensory stimuli, happen in a few milliseconds [9]. Excluding the most recent studies [9, 14-16], researchers assumed a fixed form for the BHR with a few parameters to set, such as Gaussian and Gamma filters [10, 12, 13]. However, the relation between neuronal activity and the BOLD response is not completely characterized and still remains as a research topic [17-19]. Accordingly, accurate estimation of the BHR function should be considered as a first step for accurate activity detection. Within the last few years indeed, BHR function estimation has received particular interest in fMRI data analysis [9, 15, 16].

Having stated the two major problems in fMRI data analysis, namely (i) activation detection and (ii) BHR estimation, we can now reconsider them in view of fNIRS. Diffuse optical methods, e.g. fNIRS, yields measurements that have poorer spatial resolution (3 cm at minimum) than fMRI [2]. However they, at least potentially, can provide higher temporal detail in the investigation of physiological rythms hence they are expected to be

more advantageous than fMRI in BHR function estimation. In addition, the fact that physiological components such as HbR, HbO_2, blood volume and oxygenation are readily obtained from raw fNIRS measurements constitutes a quality that can be used to understand better the baseline physiology. On the other hand, while poor spatial resolution of fNIRS leads to localization problems, an additional shortcoming happens to be the lacking of accurate computation schemes for hemoglobin concentrations. The latter inconvenience is due to many simplifications, including those in photon diffusion models and tissue geometries, which are considered in deriving the modified Beer-Lambert law. Hopefully, simultaneous fMRI-BOLD and fNIRS recordings have the potential to overcome both limitations [8].

There is a wide variety of fNIRS instruments currently in use for commercial and research purposes [2]. Although their specifications differ to some extent, they all rely on the principles described in previous sections. On-going fNIRS research is concentrated on hardware development and system characterization. However, a unified framework in treating fNIRS data from a signal processing perspective is still lacking in contrast to the abundant literature in fMRI data analysis. In order to introduce the fNIRS technique, maybe not as an alternative but a useful complement to fMRI, to the service of the clinical neuroscientist, development of signal processing techniques proper to fNIRS is compulsory. In this view, this thesis aims to fill in the gaps and to motivate further research in fNIRS data analysis.

1.4. Scope of the Thesis

The subsequent chapters in this report is devoted to an understanding of fNIRS signals. Issues such as statistical and spectral characterizations as well as activity estimation are visited. The present work is indebted a lot, in many respects, to fMRI data analysis but only from a conceptual viewpoint.

In Chapter 2, we provide specifications on the fNIRS device and acquired data as well as the details of the cognitive protocol. We treat statistical characterization by means of stationarity and Gaussianity tests.

Chapter 3 is reserved for time-frequency characterization where an original spectral band selection methodology is proposed. Using the results of band selection and prior knowledge on the data acquisition protocol, we expose evidences on the presence of cognitive activity in fNIRS signals.

Chapter 4 deals with the non-parametric estimation of cognitive activity-related fNIRS waveforms, i.e., the counterpart of BHR function estimation in fMRI. We consider two approaches, namely independent component analysis and clustering. The former has been proven to be a powerful methodology in applications where very little prior information on the data is available. It has been successfully applied to separate EEG and fMRI sources. In the second clustering approach, we represent waveforms with B-spline coefficients and cluster them to identify the functional behaviours in the data.

In the concluding Chapter 5, we discuss the findings of the thesis and future prospects.

2. STATISTICAL CHARACTERIZATION

In this chapter, we intend to present the characterization of fNIRS data in statistical terms. In particular, we address the following questions:

(i) How are data acquired? Can we use any domain knowledge to handle the data?
(ii) Does the signal result from a stationary process? If not, can we divide the signal into short-time segments, so that at least some weaker stationarity criteria are satisfied such as wide-sense stationarity?
(iii) Is the signal process Gaussian? If not, what can one say about its distribution?

The following sections treat these questions separately in order to provide a statistical characterization of fNIRS signals.

2.1. The fNIRS Device and Data

Functional NIRS data are collected by a system developed at Dr. Britton Chance's laboratory at University of Pennsylvania. The system houses a probe with four three-wavelength light emitting diodes and 12 photodetectors.

The probe is placed on the forehead and a sports bandage is used to secure it on its place and eliminate background light leakage. Functional NIRS measurements are taken from four quadruples of photodetectors, i.e., 16 in total, which are equidistantly placed on the forehead during a cognitive (e.g. target categorization) task (see Figure 2.1). At the center of every quadruple, there is a source that emits light at three different wavelengths of 730 nm, 805 nm and 850 nm.

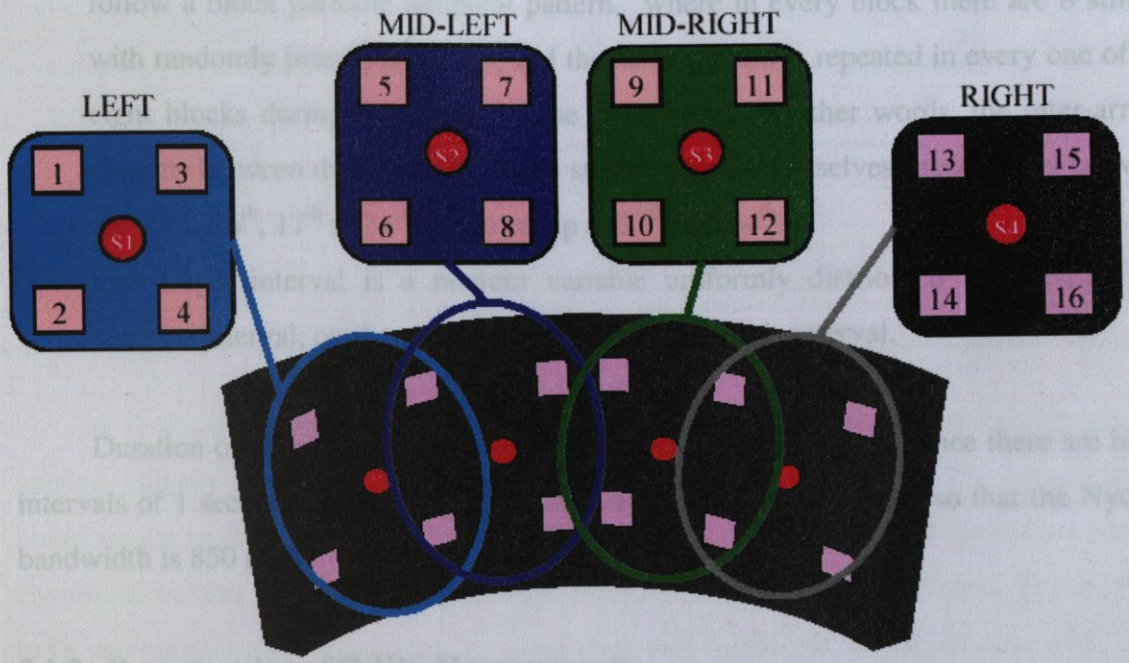

Figure 2.1. Source-detector configuration on the brain probe and nomenclature of photodetectors

2.1.1. Cognitive Protocol

Target categorization or "oddball task" is a simple discrimination task in which subjects are presented with two stimuli or classes of stimuli in a Bernoulli sequence in the center of the screen. The probability of one stimulus is less than the other (e.g., 20 per cent of trials for the "target" or "oddball" stimulus, versus 80 per cent of trials for the "typical" or "context" stimulus); the participants have to press a button when they see the less frequent of the two events. Stimulus categories are varied, beginning with the letters "XXXXX" versus the letters "OOOOO". 1024 stimuli are presented 1500 ms apart (total time, 25 minutes); a target is presented on 64 trials, with a minimum of 12 context stimuli in between to allow for the hemodynamic response to settle [20]. The subjects are asked to press the left button on a mouse when they see "OOOOO" and right button when they see the target "XXXXX". This timing parameter is used as the behavioural reaction parameter tracking the performance of the subjects. Five male subjects with an age range of 22-50 are recruited for the preliminary test. We have the following additional specifications for target stimuli.

(i) During the course of a given experiment, there are 64 target stimuli. The stimuli follow a block periodic temporal pattern, where in every block there are 8 stimuli with randomly jittered locations, and the same pattern is repeated in every one of the eight blocks during the course of the experiment. In other words, the inter-arrival patterns between the 1^{st} and 8^{th} target stimuli repeat themselves successively between the 9^{th} to 16^{th}, 17^{th} to 24^{th} and so on up to 57^{th} and 64^{th}.

(ii) Inter-target interval is a random variable uniformly distributed on the (30, 50) samples interval, or alternately on the (18, 29) seconds interval.

Duration of stimuli of both context and target types is 500 ms, hence there are blank intervals of 1 second. Recording is done at a sampling rate of 1.7 Hz, so that the Nyquist bandwidth is 850 mHz.

2.1.2. Preprocessing of fNIRS Measurements

Raw measurements consist of the optical density signals at different wavelengths, as explained in Section 1.2. It was also argued that a modified version of the Beer-Lambert law could be used to determine the concentrations of hemoglobin agents from these optical density signals [4]. Notice, however, that only two of them are required in the computation of hemoglobin components. To be more specific, measurements that belong to 730 nm and 850 nm are used to obtain these components.

The first step in preprocessing is to assess the quality of measurements and decide which one to discard. In fact, some of the photodetector outputs were not usable, due to either severe motion artifacts or occasional defects of the sensors. We did not apply any outlier elimination and denoising algorithm since the measurements were not particularly noisy.

Normally, one should have 16×3 optical density signals per subject (or experiment), i.e., 80×3 in total. After discarding faulty detectors, there remained 72×3 such signals. We did not observe any regular pattern on the spatial arrangement of rejected detectors (Table 2.1), i.e., in different experiments, different ones yielded corrupted measurements.

Table 2.1. Indices of rejected photodetectors

Subject		Indices of rejected photodetectors
Index	Alias	
1	AA005	9
2	GY002	1 to 4
3	KI003	1, 13 and 16
4	KP001	-none-
5	MJ007	-none-

A few comments are in order on the graphical depiction of primary signal sources (optical density signals) and the secondary signal sources, that is, the physiological components, such as *HbR* and HbO_2. From Figure 2.2, one can see that the optical density signals as well as hemoglobin component signals exhibit a very slow trend. These trends have an antagonistic behaviour for *HbR* and HbO_2, that is a rise in the *HbR* level correspond to a fall in the HbO_2. This observation is compatible with the brain hemodynamics and already reported in [4]. Furthermore, this trend is actually a nuisance quantity from the perspective of measuring cognitive activity and should be removed for all practical purposes. The trend removal is performed by a simple moving average filtering: a frame of support 500 samples (corresponding to 4.9 minutes of data) is slided continuously over the time-series and the mean value of the samples inside the frame is subtracted from the actual value at the frame position. Such a scheme effectively blocks the slow signal (below 3 mHz) which is responsible of the trend (Figure 2.3). In summary, preprocessing fNIRS time-series involves the following.

(i) Discarding signals from defective photodetectors (see Table 2.1.).
(ii) Computation of the hemoglobin component signals by applying the modified Beer-Lambert law on the optical density signals that correspond to 730 nm and 850 nm wavelength.
(iii) Trend removal by moving average filtering.

One might ask which hemoglobin component should be used for further analyses. The study on simultaneous recordings of fMRI-BOLD and fNIRS [8] demonstrates that the changes in oxygenated hemoglobin and the simultaneously acquired BOLD exhibit the

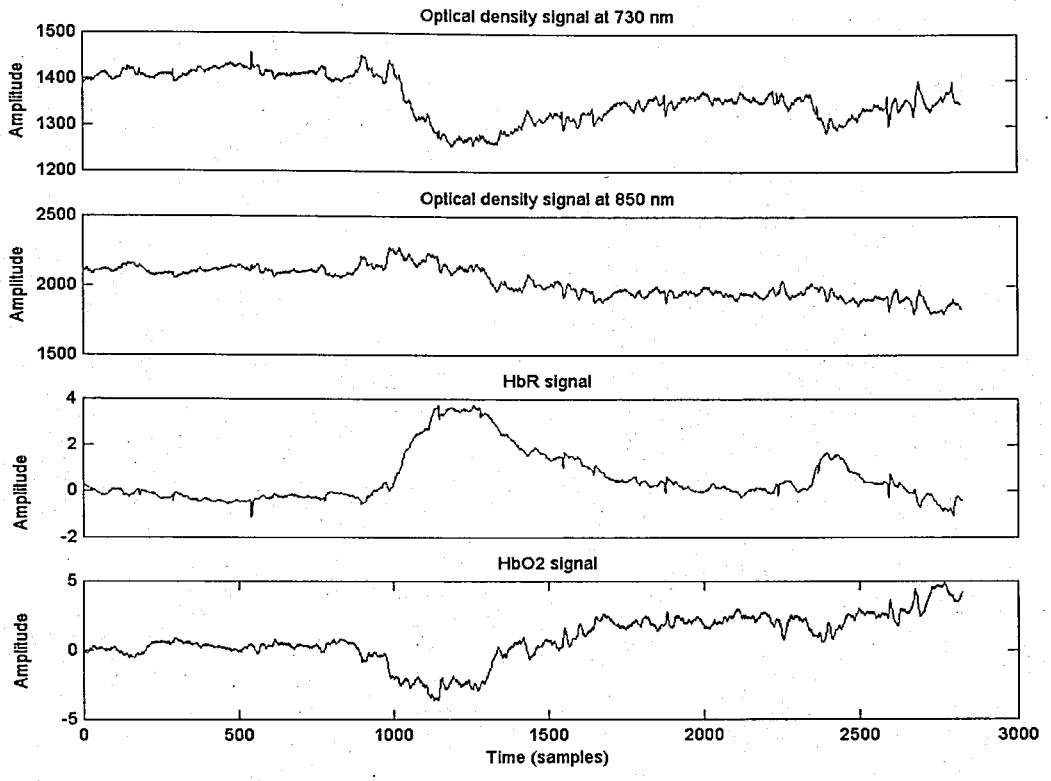

Figure 2.2. Optical density and hemoglobin component signals

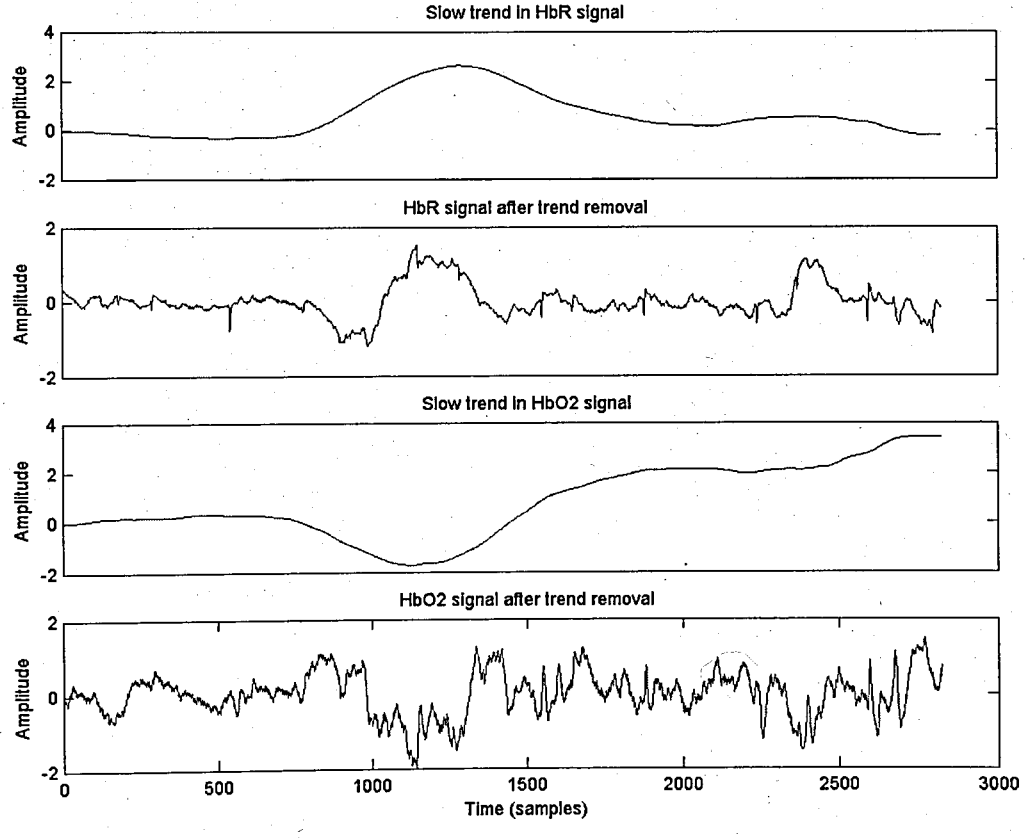

Figure 2.3. Hemoglobin component signals with trend and after trend removal

strongest correlation compared with other components such as deoxygenated hemoglobin and total hemoglobin. In this work, motivated by the fMRI studies, we consider henceforth oxygenated hemoglobin, i.e., HbO_2 signals.

2.2.3. Nomenclature of the Dataset

Each HbO_2 signal in the data set can be refered by two indices: the subject index and the index of the phodetector from which it is obtained. Denoting a HbO_2 signal by $s(t)$, the following notation is adopted.

$s_{k_0}^{j_0}(t)$: HbO_2 signal from subject j_0, photodetector k_0.

$\Gamma^{j_0} = \left\{ s_k^{j_0}(t) \,\middle|\, 1 \le k \le K,\ j_0 \text{ fixed} \right\}$: All the signals from a given subject j_0.

$\Gamma_{k_0} = \left\{ s_{k_0}^{j}(t) \,\middle|\, 1 \le j \le J,\ k_0 \text{ fixed} \right\}$: All the signals from a given photodetector k_0.

$\Gamma = \left\{ s_k^j(t) \,\middle|\, 1 \le k \le K, 1 \le j \le J \right\} = \bigcup_{j=1}^{J} \Gamma^j = \bigcup_{k=1}^{K} \Gamma_k$: All the signals in the dataset from any photodetector or subject.

$j = 1,..., j_0,..., J$ (total number of subjects J is 5)

$k = 1,..., k_0,..., K$ (total number of photodetectors for a given subject K is 16)

Recall that some of the photodetectors are not usable (as tabulated in Table 2.1), hence although the detector index runs from one to 16, we obviously skip over the defective ones.

2.2. Statistical Characterization

This section deals with the statistical characterization of the fNIRS-HbO_2 signals in terms of stationarity and Gaussianity (see Appendix A, for details of the statistical tools).

2.2.1. Stationarity of fNIRS-HbO_2 Signals

Stationarity of a process in the strict sense stands for the time-invariance of the n^{th} order joint probability distribution of the process samples. However, from a practical point

of view, it is usually very difficult and not necessary to prove strict-sense stationarity. A common practice is to use a graphical depiction of the moving time-average estimates of the central moments up to order four. The less pronounced are the time variations in these moments, the more there is ad hoc evidence about the stationarity of the underlying process. For instance, we say that the signal satisfies the wide-sense stationarity criteria, whenever the mean and the variance do not change over time. Furthermore, if it is known that the signal is from a Gaussian process, this implies strict-sense stationarity. Note that hereafter stationarity will refer to wide-sense stationarity unless otherwise stated.

In the case the process cannot be proven to be stationary, one still would be interested in the stationarity of the short-time signal segments. Short-time stationarity can also be investigated with graphical techniques [21]. In Figure 2.4, variation of the central moments up to order four are shown for a representative HbO_2 signal. Accordingly, N-sample segments are extracted from the signal with 75 per cent overlap and the moments are computed. We choose two segment lengths, $N = 200$ and $N = 400$ samples, corresponding, respectively, to two minutes and four minutes of data. Notice that, the skewness τ is a measure of the symmetricity of the underlying distribution. For symmetric distributions, such as the Gaussian, it vanishes. On the other hand, the kurtosis κ measures the "tailedness" of the underlying distribution. For random samples with $\kappa > 0$, the underlying distribution is heavy-tailed and said to be super-Gaussian; for those with $\kappa < 0$ the underlying distribution turns out to have flat tails and it is referred as sub-Gaussian. As the context implies, Gaussian distribution is the limiting case and has zero kurtosis. The time-average estimates of these moments, for an N-sample fNIRS-HbO_2 segment with first and last time indices t_1 and t_2 such that $t_2 - t_1 + 1 = N$, can be computed as

(i) *Mean* $\mu = \frac{1}{N}\sum_{t=t_1}^{t_2} s(t)$

(ii) *Variance* $\sigma^2 = \frac{1}{N}\sum_{t=t_1}^{t_2}[s(t)-\mu]^2$

(iii) *Skewness* $\tau = \frac{1}{\sigma^3 N}\sum_{t=t_1}^{t_2}[s(t)-\mu]^3$

(iv) *Kurtosis*[1] $\kappa = \frac{1}{\sigma^4 N}\sum_{t=t_1}^{t_2}[s(t)-\mu]^4 - 3$

It is known that an accurate estimation of skewness and kurtosis requires relatively large number of samples, and they are also very sensitive to outliers. Furthermore, the signal samples are not necessarily identically distributed, hence the estimates for skewness and kurtosis kurtosis should be interpreted with caution.

From Figure 2.4, we see that the signal fails to be stationary in the long run, however over short intervals there are intervals of stationarity in the wide sense. We notice these quiet regions in the first 500 and last 1000 samples of the record, while in the central regions all moments vary. These observations suggest that HbO_2 signals are globally non-stationary, but also would allow for short-time processing under the assumption of stationarity.

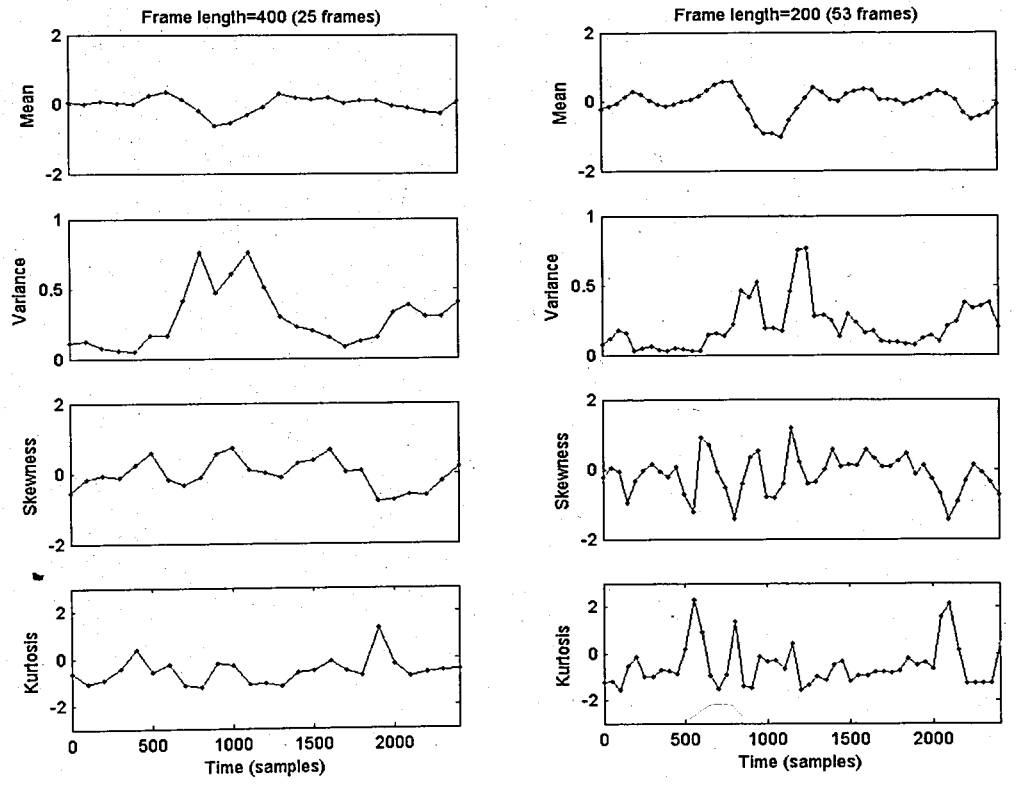

Figure 2.4. Profiles of the statistics for a typical HbO_2 signal up to fourth order

[1] The expression stands actually for the normalized kurtosis and in statistical texts it is defined without the additive constant.

Table 2.2. Run test results for short-time HbO_2 frames
(out of 3600 records, significance level $\alpha = 0.01$)

Frame length N	**Number of times the stationarity hypothesis is retained**	**Test statistic** ξ		**The range of** ξ **for the stationarity hypothesis to be retained**
		Mean	**Std. Dev.**	
400	1	39	28	177-224
200	19	22	16	84-117
100	82	14	9	39-62
50	326	9	6	17-34
30	793	7	4	9-22

We can show the non-stationary behaviour of the HbO_2 signals more formally, using statistical tests. The run test is a non-parametric, distribution-free test which is suitable for this purpose [22], based on counting the number of sign reversals around the median of a signal. This test compares a statistic ξ, which is one plus the number of sign reversals around the median, against tabulated values and returns a binary answer on the stationarity of the tested signal: either retain the stationarity hypothesis or reject it. For the sake of generality, N-sample frames from each of the signals in the fNIRS-HbO_2 dataset are randomly selected. The number of frames per signal is set to 50, yielding 72×50 = 3600 records to test. The number of samples per frame N takes the values of 400, 200, 100, 50 and 30. In Table 2.2 is shown the number of frames marked as stationarity in the run test for each selection of N. The significance level α of the tests is set to 0.01. Table 2.2 also shows that HbO_2 signals, definitely, are non-stationary unless short observation window is chosen. The mean test statistic ξ (decimal parts are removed) becomes close to the expected range only for small values of N (e.g. 30 and 50), hence for short-time analyses, one can choose frame lengths in the order of 30 and 50 samples.

We observe in Figure 2.4, that skewness is not zero and that kurtosis is not directly proportional to the variance. These imply that the fNIRS-HbO_2 process is non-Gaussian. In the next subsection, the non-Gaussianity of HbO_2 signals is established by means of rigorous statistical hypothesis testing.

2.2.2. Gaussianity Tests for fNIRS-HbO_2 Signals

There are many simple yet powerful Gaussianity (or normality) tests in the statistics literature [23]. They generally assume independent identically distributed (i.i.d.) samples, hence they are not particularly suited for testing time-series for Gaussianity due to the correlatedness of the signal samples. Under the milder condition of whiteness, that is, we assume that samples are uncorrelated, but not independent, these tests can be used for establishing the Gaussianity (or non-Gaussianity) of the time-series with lower statistical accuracy. However, time-series are uncorrelated albeit neither. That is we cannot obtain uncorrelated samples by sequentially sampling the signals. One idea to get over these problems may be to sample the signals at random locations, instead of sequential sampling, so that correlation between samples vanishes. In the sequel, the Kolmogorov-Smirnov (*K-S*) test, and the Jarque-Bera (*J-B*) test are used following the above ideas [23, 24]. On the other hand, Gaussianity tests dedicated for time-series data do exist, like Hinich's bispectrum based test [25]. However, this approach requires the signal to be stationary.

In what follows, the results of both the *K-S* test, the *J-B* test and the Hinich test are presented. However, we first visit some graphical techniques in order to get more inside on the shape of the underlying distribution.

A very useful graphical tool is the normal probability plot [26], where an empirical cumulative distribution function (cdf) is plotted along with the theoretical Gaussian (normal) cdf (see Figure 2.5). What is special with this graph is that the Gaussian cdf plots linearly with a slope of one in the log-scale. The distance between the tick marks on the ordinate axis matches the distance between the quantiles of a normal distribution. The quantiles are close together near the median (probability of one half) and stretch out symmetrically moving away from the median. Any deviation of the empirical cdf from linearity is indicative of non-Gaussian behaviour. The top row in Figure 2.5 show test cases of sample cdf's of Gaussian and exponential distributions. We see that samples (blue data points) from the exponential distribution deviates curvilinearly from the straight line of Gaussian cdf in red. The bottom row of Figure 2.5 illustrates two cases of the sample cdf plots of actual HbO_2 data. In Figure 2.5 (c) we see a collection of samples that results

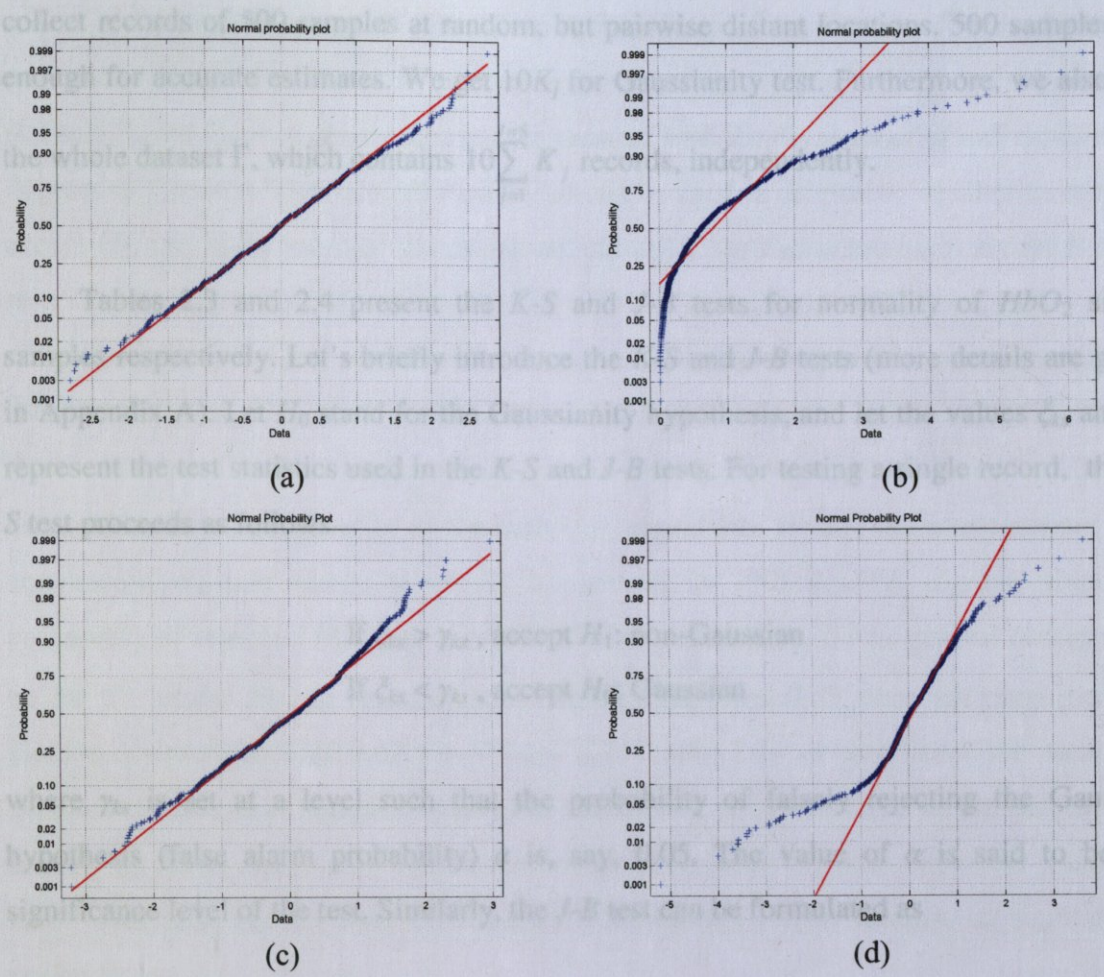

Figure 2.5. Normal plots for data from different distributions, vertical axes are read as probability (in log-scale), horizontal axes as data

in a good fit to the normal line, whereas in Figure 2.5 (d) deviations from normality (especially at the tails) are clear. The latter collection has indeed a positive kurtosis ($\approx$ 5.14), i.e., it's heavy tailed. Note that both collections are obtained from the same HbO_2 signal but at different random locations sufficiently distanced to guarantee uncorrelatedness.

After this sample illustration, we need to test over a much large number of collections, each of which should contain a large number of signal samples in its turn, and then apply a combined test statistic in order to reject or retain the Gaussianity assumption. In the following results, consider the signal sets Γ^j, the ensemble of all the HbO_2 signals, that is recordings from all detectors, from subject j, $j = 1,..., J$ with $J = 5$. As was given in Table 2.1, the number of signals K_j differs from subject to subject. For each subject j, we

collect records of 500 samples at random, but pairwise distant locations. 500 samples are enough for accurate estimates. We get $10K_j$ for Gaussianity test. Furthermore, we also test the whole dataset Γ, which contains $10\sum_{j=1}^{J=5} K_j$ records, independently.

Tables 2.3 and 2.4 present the *K-S* and *J-B* tests for normality of HbO_2 signal samples respectively. Let's briefly introduce the *K-S* and *J-B* tests (more details are given in Appendix A). Let H_0 stand for the Gaussianity hypothesis, and let the values ξ_{ks} and ξ_{jb} represent the test statistics used in the *K-S* and *J-B* tests. For testing a single record, the *K-S* test proceeds as follows

$$\text{If } \xi_{ks} > \gamma_{ks} \text{ , accept } H_1\text{: non-Gaussian}$$
$$\text{If } \xi_{ks} < \gamma_{ks} \text{ , accept } H_0\text{: Gaussian}$$

where γ_{ks} is set at a level such that the probability of falsely rejecting the Gaussian hypothesis (false alarm probability) α is, say, 0.05. The value of α is said to be the significance level of the test. Similarly, the *J-B* test can be formulated as

$$\text{If } \xi_{jb} > \gamma_{jb} \text{ , accept } H_1\text{: non-Gaussian}$$
$$\text{If } \xi_{jb} < \gamma_{jb} \text{ , accept } H_0\text{: Gaussian}$$

where γ_{jb} is set at a level such that the probability of falsely rejecting the Gaussian hypothesis α is, say, 0.05. Equivalently, these two tests can be performed using computed false alarm probability p_{ks} for *K-S* test and p_{jb} for *J-B* test as described below.

$$\text{If } p_{ks} \text{ (or } p_{jb}) < \alpha \text{ , accept } H_1\text{: non-Gaussian}$$
$$\text{If } p_{ks} \text{ (or } p_{jb}) > \alpha \text{ , accept } H_0\text{: Gaussian}$$

In order to combine test results of individual records in the signal set Γ^j, following Fisher's ideas [27], the combined test statistic P, for both *K-S* and *J-B* tests, can be computed using

$$P = -2\sum_i \log|1-2p_i| \tag{2.1}$$

where p_i denotes the computed false alarm probability of i^{th} test (on the i^{th} record) and the summation runs up to the total number of records in the signal set. The combined test statistic P_{ks} (or P_{jb}) is a chi-square random variable with 2×(the number of individual tests) degrees of freedom. The value of P_{ks} (or P_{jb}) can be used to determine whether to reject or accept H_0, i.e., if the value of the chi-square cdf at P_{ks} (or P_{jb}) is too high, accept H_0; else reject it (see Appendix A for more details on Fisher's combined test). Based on the results of Tables 2.3 and 2.4, we see that the *J-B* test has a more pronounced tendency to reject H_0 than the *K-S* test. The number of cases the *K-S* test rejected H_0 is less than the *J-B* test does; consequently, the significance level achieved by the latter is much smaller than the one achieved by the former for all the individual signal sets Γ^j and the whole dataset Γ. In conclusion, we can safely reject H_0 hypothesis for fNIRS-HbO_2 signals, since the probability of rejecting H_0 when it is indeed true is extremely low in general (except may be for Γ^2 where H_0 can be accepted at significance level 0.05 since the combined test yielded a significance of 0.02 for *K-S* test). In Table 2.4, we also show the mean and standard deviations of sample estimates of skewness τ and of kurtosis κ. We note that the underlying HbO_2 distribution can be considered as symmetric (mean skewness is around zero) with tails heavier than the Gaussian distribution (mean kurtosis is significantly positive).

Finally, let's turn to Hinich's bispectrum based Gaussianity test which is applicable for time-series. The test is based on the fact that signals from a Gaussian process have zero bispectrum. Hence if we can compute a test statistic ξ_{hin} that measures how much sample estimate of the signal bispectrum deviates from zero, we can establish whether the signal comes from a Gaussian process or not. In Hinich's test also, the test statistic ξ_{hin} is accompanied with a computed probability p_{hin} of the risk in rejecting H_0. As usual, if p_{hin} exceeds α, one can deduce that it is risky to reject H_0 and the Gaussianity of the signal is retained. As described previously, false alarm probabilities p_{hin} can be used to compute the combined test statistic P_{hin} which will be effective for testing the Gaussianity of all the records together. Note that in Hinich's test, there is no need for random sampling since it is purely designed for correlated time-series. However, stationarity of the records is necessary, i.e., the size of the individual records should be small. Accordingly, we collect 50 records of 30 sequential samples from each signal. This yields $50K_j$ cases to test for an

individual signal set Γ^j, $50\sum_{j=1}^{J=5} K_j$ cases for the whole dataset Γ. The results are shown in Table 2.5 (significance level α of the individual tests is set to 0.05 again).

Individual Hinich's tests demonstrate that a majority of short-time fNIRS-HbO_2 segments fail to come from a Gaussian process. In the overall, the Gaussianity assumption is rejected with practically no risk. These results are compatible with those of K-S and J-B tests. The unique but fundamental conclusion of this subsection is that fNIRS-HbO_2 signals are non-Gaussian.

Table 2.3. Results of Kolmogorov-Smirnov tests

		Signal Set					
		Γ^1	Γ^2	Γ^3	Γ^4	Γ^5	Γ
Number of records		150	120	130	160	160	720
Number of times H_0 retained		72	99	81	84	33	398
Number of times H_0 rejected		78	21	49	76	127	322
ξ_{ks}	**Mean**	0.08	0.05	0.06	0.06	0.10	0.07
	Std. Dev.	0.05	0.01	0.03	0.02	0.07	0.04
γ_{ks} **at** $\alpha = 0.05$		0.06	0.06	0.06	0.06	0.06	0.06
P_{ks}		161.2	196.36	138.60	121.90	44.22	696.81
Result of the combined tests (based on P_{ks})		Reject H_0 at significance 10^{-11}	Reject H_0 at significance 0.02	Reject H_0 at significance 10^{-10}	Reject H_0 at significance 10^{-25}	Reject H_0 at significance 10^{-79}	Reject H_0 at significance 10^{-67}

Table 2.4. Results of Jarque-Bera tests

		Signal Set					
		Γ^1	Γ^2	Γ^3	Γ^4	Γ^5	Γ
Number of records		150	120	130	160	160	720
Number of times H_0 retained		44	43	20	24	4	143
Number of times H_0 rejected		106	77	110	136	156	577
τ	**Mean**	-0.14	0.14	0.06	-0.34	0.05	0.00
	Std. Dev.	1.57	0.56	1.18	0.33	4.86	2.21
κ	**Mean**	3.86	1.34	3.51	0.48	33.75	8.17
	Std. Dev.	12.26	2.34	5.35	0.84	74.14	33.70
ξ_{jb}	**Mean**	3578.60	176.00	952.51	37.59	137793.41	25111.52
	Std. Dev.	17276.14	824.60	2581.39	50.67	407016.03	180234.45
γ_{jb} **at** $\alpha = 0.05$		5.99	5.99	5.99	5.99	5.99	5.99
P_{jb}		86.00	75.81	38.75	35.79	4.78	253.96
Result of the combined tests (based on P_{jb})		Reject H_0 at significance 10^{-36}	Reject H_0 at significance 10^{-25}	Reject H_0 at significance 10^{-60}	Reject H_0 at significance 10^{-91}	Reject H_0 at significance 10^{-225}	Reject H_0 at significance 10^{-286}

Table 2.5. Results of Hinich's tests

		Signal Set					
		Γ^1	Γ^2	Γ^3	Γ^4	Γ^5	Γ
Number of records		750	600	650	800	800	3600
Number of times H_0 retained		236	238	297	468	359	1583
Number of times H_0 rejected		514	362	353	332	441	2017
p_{hin}	**Mean**	0.15	0.19	0.25	0.26	0.23	0.22
	Std. Dev.	0.27	0.30	0.34	0.31	0.32	0.31
P_{hin}		450.36	482.44	483.54	939.01	717.77	3008.51
Result of the combined tests (based on P_{hin})		Reject H_0 at significance 10^{-165}	Reject H_0 at significance 10^{-83}	Reject H_0 at significance 10^{-103}	Reject H_0 at significance 10^{-43}	Reject H_0 at significance 10^{-88}	Reject H_0 at significance 0

Boğaziçi Üniversitesi Kütüphanesi

3. TIME-FREQUENCY CHARACTERIZATION

In this chapter, we analyze the fNIRS-HbO_2 signals in the time-frequency plane. We think that several physiological events are measured by fNIRS and each of them is associated with a particular frequency band of the HbO_2 signal. Identification of such bands can provide us with some general guidelines in distinguishing between the baseline and cognitive activity.

Spectral analysis of physiological signals are important in that the oscillatory dynamics in physiological systems are considered to reflect the degree of functionality. Presence of such dynamics have been observed especially in the brain by neuroimaging experts. Specifically, electroencephalogram (EEG) signals are analyzed by decomposing them into several predetermined frequency bands corresponding to different physiological activities [28]. As Başar and co-workers argue about the oscillatory dynamics in EEG: "With respect to the brain, resonance is defined as the ability of brain networks to facilitate (or activate) electrical transmission within determined frequency bands, when an external sensory stimulation signal is applied to the brain" [29]. Efforts for characterizing the components in signal spectra have usually aimed to provide a physiological correspondence to the peaks or the energy bands. EEG literature is well developed in the field of frequency analysis owing mostly to its early discovery dating back to 1900's. On the contrary, new comers in the field of neuroimaging such as fMRI, PET, transcranial doppler sonography (TCDS) and fNIRS finally have still not received their share of attention from the signal processing experts. Although several studies have proposed association mechanisms between spectral ranges and physiological activities, there is no consensus on the exact division of spectrum into bands of clinical importance.

Several researchers have decided to investigate the fMRI, PET and TCDS spectra in search of bands that can elucidate the underlying physiological dynamics where specific spectral peaks or bands are assumed to be related to a specific task [30]. The general view is that while some of the oscillatory dynamics occur independent of the task and are distributed over distinct spectral bands uncorrelated with other physiological activities (e.g. breathing, heartbeat etc.), others can be directly affected by psychological or pathological

Boğaziçi Üniversitesi Kütüphanesi

conditions (or vice versa) that exhibit themselves as a shift in performance [31]. A subset of such studies investigate the coupling mechanisms between cerebral energy metabolism and cerebrovascular dynamics (namely neurovascular coupling).

In this chapter, we first try to do an explorative study of the typical fNIRS-HbO_2 spectrum. We then present an original frequency subband partitioning methodology. The proposed subbanding scheme is general and can be applied to signals other than fNIRS-HbO_2. Finally, we prove that fNIRS measures cognitive activity, and that constitutes one of the major contributions of this work.

3.1. The Typical fNIRS-HbO_2 Spectrum

A time-frequency representation (TFR) of a non-stationary signal is especially useful in visualizing the evolution of the spectral content through time. This can for instance be achieved by the *short time Fourier transform* (STFT) or *windowed Fourier transform* (WFT) as defined below

$$S(\tau, f) = \int_{-\infty}^{\infty} s(t) w(t-\tau) e^{-j2\pi ft}\, dt \tag{3.1}$$

where $s(t)$ denotes the fNIRS signal of interest and $w_D(t)$ is a window of finite support D. The STFT in (3.1) is actually computed using the *discrete Fourier transform* (DFT), so that the TFR is discrete in both time and frequency, respectively, with time resolution Δt and frequency sampling interval Δf. A TFR is warranted since the signals are non-stationary and also because the aim is to capture and characterize local events, like cognitive activity in the course of the fNIRS process. The windowing $w_D(t)$ guarantees the local nature of the spectral analysis and its support is chosen so that within that D interval the process can be considered to be at least wide-sense stationary. To control spectral leakage and peak resolution, the window shape should be judiciously chosen [32]. Table 3.1 gives the parameters used in the TFR analysis. One should see that the frequency resolution is given by the effective window length, hence it is of the order of 50 mHz, while the one mHz frequency sampling rate Δf is obtained by padding the windowed time series with zeroes.

Table 3.1. Parameters of the TFR (sampling rate F_s=1700 mHz)

Parameter	Value	Comment
Window type	Hamming	*Hamming window has good sidelobe suppression.*
Window length D	36 samples ≈ 21 s	*An interval of such length can be considered as "stationary".*
Time resolution Δt	9 samples ≈ 5.3 s	*This guarantees at least four samples per chosen window length, which provides adequate temporal resolution.*
Frequency sampling Δf	1 mHz	*This is set in order to have sufficient number of samples in the bands as narrow as 10 mHz.*

A 3D-graph or the contours of the TFR of a time-series alone would provide us some qualitative information about the spectral content. Figures 3.1 (a) and (b) consist of such graphs obtained from a fNIRS-HbO_2 signal. Observing these, one may conclude that the time-series is essentially low-pass (main spectral content<100 mHz), that no significant events at all in the range of 200-700 mHz exist and there is some activity pattern between 700-850 mHz. Hence without objective measures, inferences we can make from a TFR remain limited. The TFR should further be exploited by deriving some quantifiable magnitudes as Blanco et al. suggested [28]. The relative power profile per band is such an objective measure and will be defined next. Let's consider a set of frequency intervals $(f_{n,l}, f_{n,h})$, n = 1,..., N that partitions the frequency axis into subbands, which are not necessarily equal. Then the evolutionary power spectral density within the n^{th} frequency band at the instant t is defined as

$$B_n(t,f) = S^*(t,f)S(t,f) \text{ in } f \in (f_{n,l}, f_{n,h}) \tag{3.2}$$

where $f_{n,l}$ and $f_{n,h}$ denote, respectively, the lower and upper limits of the band. The total power in the respective band as a function of time can now be calculated by

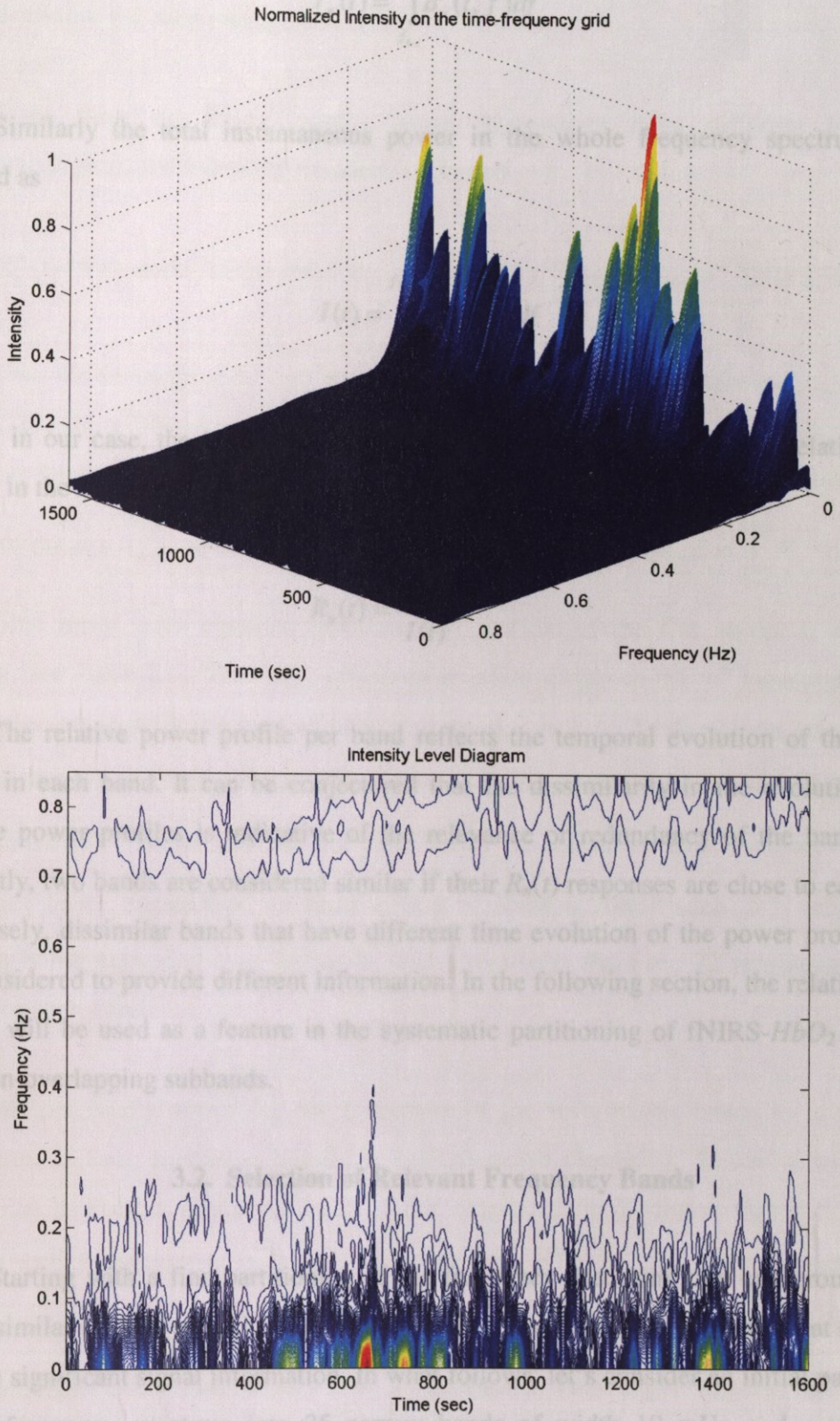

Figure 3.1. 3D normalized intensity graph (top) and intensity level diagram for the TFR of a typical fNIRS-HbO_2 signal (bottom)

$$I_n(t) = \int_{f_{n,l}}^{f_{n,h}} B_n(t,f)df \tag{3.3}$$

Similarly the total instantaneous power in the whole frequency spectrum $I(t)$ is defined as

$$I(t) = \int_{0}^{f_{Nyquist}} B_n(t,f)df \tag{3.4}$$

where, in our case, the integration goes from 0 to 850 mHz. Finally, the relative power profile in the n^{th} band as a function of time becomes

$$R_n(t) = \frac{I_n(t)}{I(t)} \tag{3.5}$$

The relative power profile per band reflects the temporal evolution of the relative power in each band. It can be conjectured that the dissimilarity in the evolution of the relative power profiles is indicative of the relevance or redundancy of the bands. More explicitly, two bands are considered similar if their $R_n(t)$ responses are close to each other; conversely, dissimilar bands that have different time evolution of the power profile, $R_n(t)$ are considered to provide different information. In the following section, the relative power profile will be used as a feature in the systematic partitioning of fNIRS-HbO_2 spectrum into non-overlapping subbands.

3.2. Selection of Relevant Frequency Bands

Starting with a fine partitioning of the frequency spectrum, one can group narrow bands similar in their evolutionary energy profiles, $R_n(t)$, into wider bands that hopefully capture significant signal information. In what follows, let's consider an initial partitioning of the frequency spectrum into 25 narrow bands of width 10 mHz and a wide high frequency band covering the 250-850 mHz range, 26 bands in total. All higher frequency bands are lumped into one 250-850 band as there is very little power in this frequency

range and the signals lacked a definitive structure. In fact, this wide band contains only nine per cent of the total average power.

Since there are many relative power time-series from different bands and detectors/subjects, the following notation is adopted

$R_n^m(t)$: time-series of the *relative power* for the n^{th} band of the m^{th} fNIRS signal

Thus the subscript n denotes the frequency band of interest, where n=1,...,N=26. For $1 \le n \le 25$, the n^{th} band covers the frequency range [(n-1)×10, n×10)] mHz, while for n=26, the band covers the 250-850 mHz range. On the other hand, the superscript m points to one of the m = 1,..., M=72 time series in the dataset Γ, note that $M = \sum_{j=1}^{J=5} K_j$. Recall that these time series were obtained from the 16 detectors of the five subjects, after some pruning (see Table 2.1). Thus the superscript m refers simply to the m^{th} measurement. The time index t runs with the lags of Δt = 9 samples, t = 1,..., T. It will be convenient to express the whole time series $R_n^m(t), t = 1,...,T$ in vector notation as $\mathbf{R}_n^m$. The T-dimensional $\mathbf{R}_n^m$ vector denotes the time series of the m^{th} detector/subject in the n^{th} frequency band. Notice that we have a total of N×M = 26×72 such $\mathbf{R}_n^m$ vectors, each detector being expanded onto 26 bands, and conversely, there are 72 representative time series for each band.

We practically search for the formation of the informative bands by a clustering procedure. In fact, a scheme based on agglomerative clustering[2] followed by majority voting can be used as described below. After obtaining the N relative power profiles per band of each measurement m, the set of N subbands $R^m = \{\mathbf{R}_n^m\}_{n=1,...,N}$ are grouped into C subbands $Q^m = \{Q_c^m\}_{c=1,...,C}$. Specifically the 26 initially chosen subbands from any detector/subject are clustered into C = 3 subbands. This target number of clusters is decided for in order to allow a possibly very low frequency band, a high frequency band and potentially a single "interesting" mid-band.

[2] For a brief summary of clustering and agglomerative approaches in particular, see Appendix B.

There are two important aspects in an agglomerative clustering algorithm: the *metric* used to compute distances and the *closeness criterion* between vectors. Here the following are adopted

(i) *One-minus-the-normalized correlation coefficient* as the distance metric:

$$d(\mathbf{R}_p^m, \mathbf{R}_q^m) = 1 - \frac{\langle \mathbf{R}_p^m, \mathbf{R}_q^m \rangle}{\|\mathbf{R}_p^m\| \cdot \|\mathbf{R}_q^m\|} \tag{3.6}$$

where $\langle .,. \rangle$ stands for the inner product of two vectors and $\|.\|$ for the Euclidean norm. The vectors involved in the computation are made zero-mean by subtracting their mean value.

(ii) *Single linkage criterion* as the closeness criterion, according to which the pair of bands (p,q) for which $d(\mathbf{R}_p^m, \mathbf{R}_q^m)$ is minimum should be merged.

The end product of clustering the R^m set is a dendrogram D^m, an hierarchical tree that helps us to visualize cluster relationships. An example is shown in Figure 3.2. The dendrogram for the m^{th} measurement D^m is pruned in order to get the clustered set Q^m. This is accomplished by simply obtaining the cutset of the dendrogram that yields the target number of C clusters. In other words, the dendrogram is cut at a distance value of the ordinate to yield the desired number of clusters, e.g., at 0.15 as shown in Figure 3.2. Within each one of the C clusters, the merged bands are similar to each other according to the chosen correlation coefficient metric, while across clusters they are dissimilar. The leaves of the dendrogram, that is the singleton clusters, which correspond to the initial bands, become thus grouped into C = 3 larger bands. Once the agglomerative clustering is accomplished we obtain M dendrograms, one for each measurement. To extract a single set of subbands from the M clusters, a voting scheme is resorted to. At this stage there are in the overall $M \times C$ = 72×3 = 216 frequency bands with differing bandwidths, out of which we try to determine the most frequently occurring ones. Therefore these 216 band patterns should be ranked based on their frequency of occurrence. To make this point clear, let's consider again the sample dendrogram in Figure 3.2, which results in the following subbands: {0-30, 30-40, 40-850}. We determine how many times each of these subband formations were generated by clustering of all the R^m measurements, each occurrence

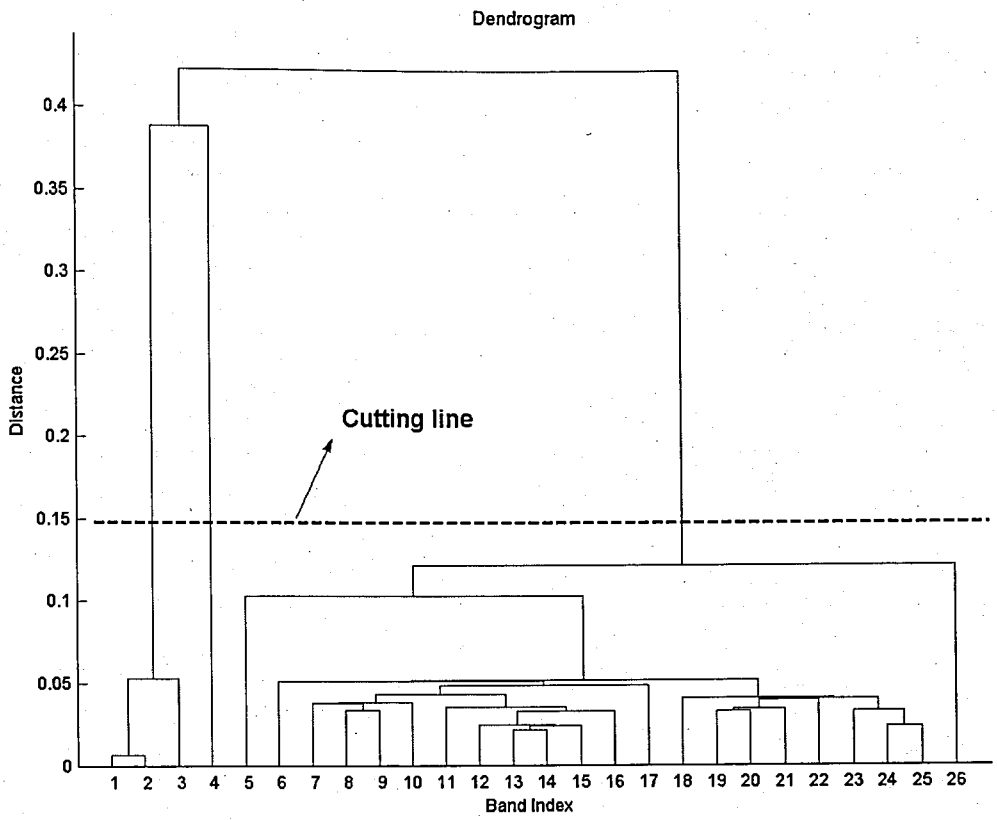

Figure 3.2. A typical dendrogram: the horizontal axis indexes the initial bands, vertical axis indicates pairwise cluster distances.

counting as a vote. Selecting the subband patterns that have received the highest number of votes (frequency of occurrence), we achieve a "canonical" partitioning of fNIRS frequency spectrum, where the resulting bands are non-overlapping and exhaustively cover the frequency interval 0-850 mHz.

As a result of band clustering and voting, nine candidate bands that shared 216 votes are obtained as shown in Table 3.2. A couple of partitionings that collectively covers the spectrum is possible (see Table 3.3). The spectrum partitioning that gets the highest number of votes happen to be the following sequence of bands: 0-30 mHz, 30-40 mHz, 40-250 mHz and 250-850 mHz. They receive in all 142 votes, i.e. 65.7 per cent of the total. We hence can argue that this partitioning is reliable in characterizing the fNIRS spectrum in terms of energy percentage profiles. Hereafter we call them as "canonical frequency bands" and denote them by letters as shown in Table 3.4.

Table 3.2. Candidate frequency bands (out of 216 cases)

Bands (mHz)	Number of votes
250-850	44
0-30	35
0-40	35
40-250	35
30-40	28
40-850	28
30-250	7
0-50	2
50-250	2

Table 3.3. Possible spectrum partitionings and their significances

Spectrum partitioning	Votes	Percentage
0-30 mHz, 30-40 mHz, 40-250 mHz, 250-850 mHz	142	65.7 %
0-40 mHz, 40-250 mHz, 250-850 mHz	114	52.8 %
0-30 mHz, 30-250 mHz, 250-850 mHz	86	39.8 %
0-40 mHz, 40-850 mHz	63	29.2 %
0-50 mHz, 50-250 mHz, 250-850 mHz	48	22.2 %

Table 3.4. Canonical frequency bands of fNIRS signals

Bands	0 -30	30-40	40-250	250-850 >>
(mHz)	*A*	*B*	*C*	*D*
Votes	35	28	35	44

Physiological interpretation of the canonical bands: In several studies, three main frequency bands of interest have been identified for cerebral hemodynamics: a very low frequency (VLF, 8-33 mHz), a low frequency (LF, 100 mHz) and a high frequency component (HF, 250 mHz) definitely in synchrony with breathing rate [33]. Similarly, it can be conjectured that each of the canonical bands is associated to one or more of the physiological activities that are assessed by hemoglobin concentrations. The very-low frequency band, namely the *A*-band, is responsible for the slow signal or the baseline signal that is thought to be reflecting the very slow vasomotor fluctuations. In fact, reports on the frequency content of such fluctuations have identified this signal as being the phasic dilation and contractions of the small regulating arteries. According to Kuo et al. "these

vasomotor waves produce fluctuations in cerebral blood volume, which are eventually reflected in the intracranial pressure" [33]. As a matter of fact, it can be thought that this band is independent of the stimulated cognitive activity. Based on the observation that typical brain hemodynamic response model functions, e.g. the centered Gamma function (Figure 3.3), exhibit significant spectral activity in the 30-50 mHz range, the very narrow *B*-band should be related to task-related cognitive activity of the subject. The larger *C*-band is also assumed to carry cognitive activity related information, most probably due to the periodicity of the target stimuli sequence. Moreover, vasomotion and breathing rate are two physiological facts that are responsible for the emerging of the *C*-band. Finally, the high frequency *D*-band reflects some weak high frequency fluctuations and confines the aliased part of the heart rate signal (~1.1 Hz).

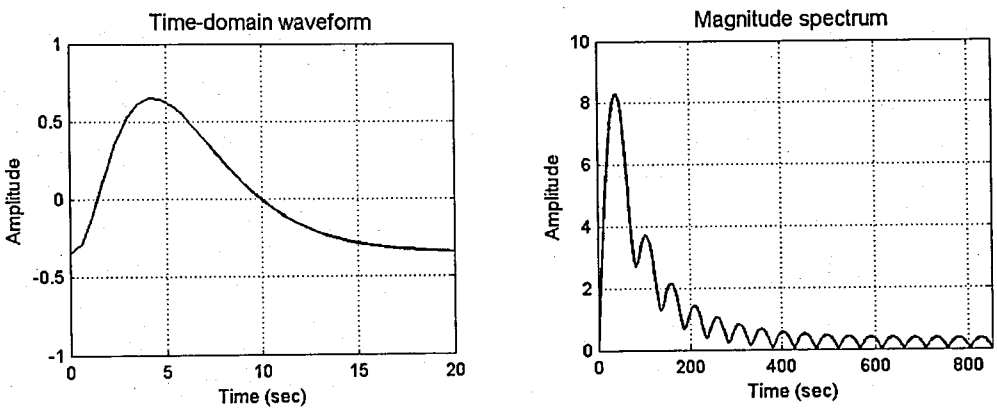

Figure 3.3. The centered Gamma function (left) and its Fourier spectrum magnitude (right), note that high frequency lobes are due to removing the DC-value of the signal

Although the canonical bands are dissimilar in terms of the chosen metric, there certainly remain some residual correlations. Hence, a quantification of the similarities between relative power profiles at these bands would be instructive. In order to track this purpose, the following is evaluated

$$\overline{\rho}_{pq} = \frac{1}{M} \sum_{m=1}^{M=72} \frac{\langle \mathbf{R}_p^m, \mathbf{R}_q^m \rangle}{\left\| \mathbf{R}_p^m \right\| \left\| \mathbf{R}_q^m \right\|} \tag{3.7}$$

where $p,q \in \{A,B,C,D\}$ and $\mathbf{R}_q^m$ is as defined previously, again the vectors in the computation of the inner-product are made zero-mean. The averaged normalized correlation coefficients $\overline{\rho}_{pq}$ take the values given in the matrix form below

$$[\overline{\rho}_{pq}] = \begin{bmatrix} & A & B & C & D \\ A & 1 & 0.50 & -0.94 & -0.51 \\ B & 0.50 & 1 & -0.45 & -0.54 \\ C & -0.94 & -0.45 & 1 & 0.29 \\ D & -0.51 & -0.54 & 0.29 & 1 \end{bmatrix}.$$

We can observe that there exists is a strong negative correlation (correlation coefficient of minus 0.94) between the *A*-band and *C*-band in terms of their relative power profiles. In other words an accumulation of power in one band (say *A*) causes a depletion of the power in the other band (*D*), and vice versa. One can envision the time series $R_A^m(t)$ and $R_C^m(t)$ being almost "antipodal" signals.

3.3. Evidence of Cognitive Activity in fNIRS-HbO_2 Signals

Since the cognitive stimuli are quasi-periodic, with inter-target intervals uniformly distributed between 18-29 seconds, we can expect some sort of periodic behavior in the signal portions that are related to cognitive activity. The frequency bands where more distinctly such periodic response emerges can be said to better reflect cognitive activity or the "brain hemodynamic response". Recall that the brain displays continuous activity patterns even in the absence of any cognitive task. The cognitive activity waveforms, if any, will be in general immersed in some baseline activity waveforms. In fact, experiments show that cognitive activity responses are very difficult to discern by observing the waveforms in the full-band signals. It follows that classical Fourier spectrum and peak picking techniques are not suitable for hunting these responses and more sophisticated statistical methods must be invoked to detect and estimate these hidden periodicities.

Thus we turn now to the time-domain signals corresponding to the fNIRS canonical bands, and investigate the time series in the bands $\{A,B,C,D\}$ for the existence of a

periodicity. The admissible periods however should be in the neighborhood of the target exposition periods used in the experimental protocol, that is in the 18-29 seconds range or its harmonic/subharmonic multiples. Notice that in frequency domain, the periodicities that we are seeking, can only be reflected in a sampling effect of the continuous spectrum. That is, if a time-domain signal is periodic with P_0 seconds, the corresponding spectrum should exhibit spectral samples that are $1/P_0$ Hz apart. In the 18-29 seconds range, the sampling of the spectrum is between 34 mHz and 59 mHz. To accommodate this range of frequencies let's consider, based on previous conjectures, the merged version of two cognitive activity related bands *B* and *C*, which covers the 30-250 mHz range. Preliminary analysis shows that the *D*-band in the 250-850 mHz range appears too random to contain any cognitive task activity. On the other hand, based on the results from previous studies [33]- [35], it is hypothesized that the *A*-band is associated with the fNIRS baseline activity unrelated to the brain hemodynamics and hence it is excluded. The time-domain signal in the *BC*-band is obtained by band-pass filtering of the fNIRS time series signals. To this effect, zero-phase finite impulse response (FIR) filters with unit gain in the passband and a 3 dB transition bandwidth of 1 mHz was useful. Notice again at this stage, one should revert to the original fNIRS signals $\{s(t)\}$ in (3.1). The corresponding band-pass filtered signals are denoted as $x(t) = s_{BC}(t)$ for simplicity.

The adopted periodicity measure is based on a classical method to estimate the pitch period in speech signals: least-square periodicity estimation (LSPE) [36]. It is simply based on the minimization of the weighted mean-squared error (MSE) between the observed signal $x(t)$ and an estimated signal $x_0(t)$ that satisfies $x_0(t) = x_0(t + kP_0)$, $t = 1,..., T$ and $k = 0,..., K = \left\lfloor T/P_0 \right\rfloor - 1$ where $\lfloor \cdot \rfloor$ denotes the floor operation. The optimal $x_0(t)$, for a given P_0, is

$$x_0(t) = \frac{\sum_k x(t + kP_0) w(t + kP_0)}{\sum_k x(t + kP_0)} \tag{3.8}$$

where $w(t)$ is the weight sequence of length T. Observe that (3.8) reduces to the following in case of all the signal samples are equally weighted, i.e., $w(t)$ is a rectangular window,

$$x_0(t) = \frac{1}{K}\sum_k x(t + kP_0) \tag{3.9}$$

It has been argued that the weight sequence should be selected so that it gets the maximum value of unity at the center of its support and so that it decays smoothly down to zero towards the extremes since the periodicity deviates more heavily at the extremes than at the center. It has originally been shown that P_0 that minimizes the weighted MSE is equivalently the one that maximizes

$$J_0(P_0) = \frac{I_0}{E} \tag{3.10}$$

where I_0 stands for the weighted energy of the estimate $x_0(t)$ and E for the weighted energy of the original signal $x(t)$. The unbiased version of (3.10) yields the J_1-index, which is expressed as

$$J_1(P_0) = \frac{I_0 - I_1}{E - I_1} \tag{3.11}$$

where $I_1(P_0) = \sum_t \frac{x^2(t)w^2(t)}{\sum_k w(t + kP_0)}$. Note that the LSPE with J_1-index is also called as the pseudo-maximum likelihood estimation of periodicities [36].

Using (3.11), one should for look for the value of $\hat{P}_0$ that maximizes the $J_1(P_0)$ functional and this value is taken as the dominant period in the signal provided the periodicity index $J_1(P_0)$ is sufficiently high. In fact, the index function can be interpreted as a confidence score that becomes one for a truly periodic signal. Since some maximizing value of $\hat{P}_0$ can always be found, for this estimate to correspond to a genuine periodicity, the confidence score should exceed a threshold. In the case of fNIRS-HbO_2, the allowed range of $\hat{P}_0$ is between P_{min} and P_{max}, as infered from the experimental protocol, in which

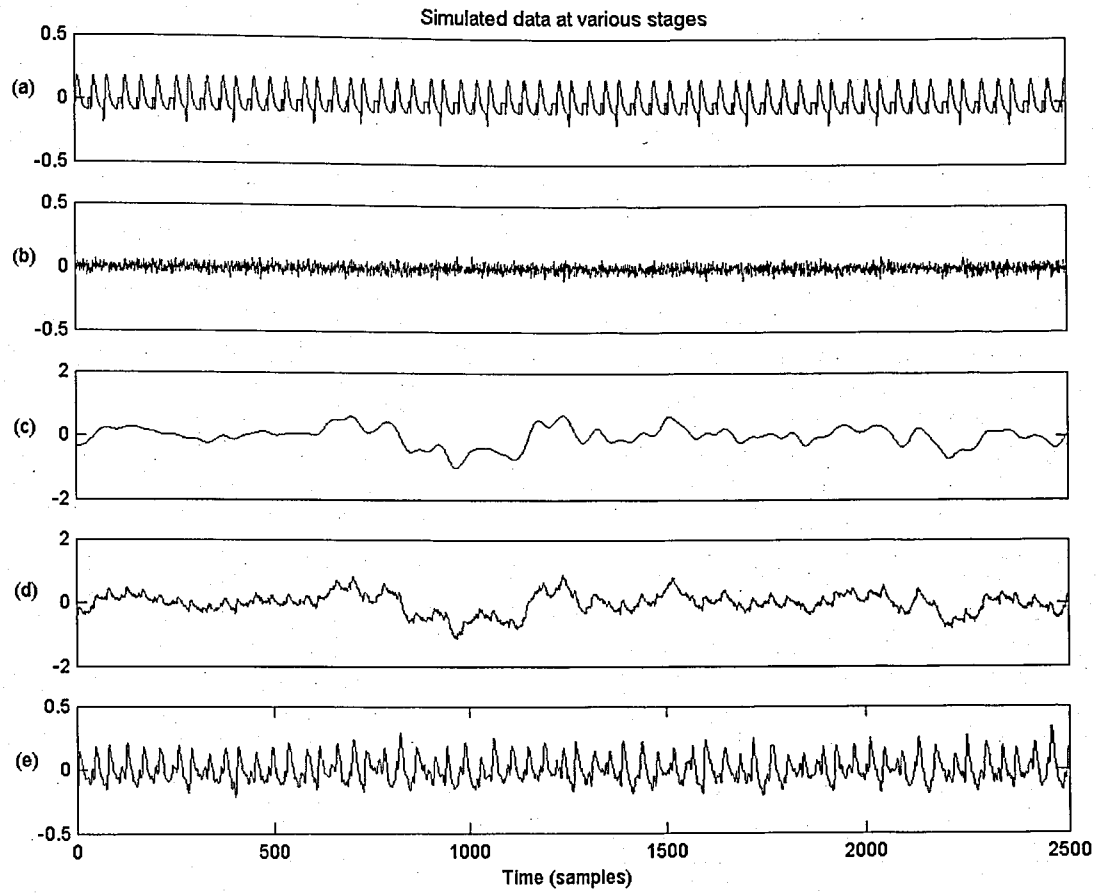

Figure 3.4. (a) Simulated quasi-periodic sequence of cognitive activity waveforms; (b) White noise sequence (SNR = 10 dB); (c) An actual *A*-band signal; (d) Superposition of the signals (a), (b) and (c); (e) Band-pass filtered version of (d) in the *BC*-band

$J_1(\hat{P}_0)$ values are computed. Let's note that, since the cognitive stimuli are not exactly periodic and since furthermore the cognitive activity signals are heavily embedded in baseline signals, we should not expect the $J_1(\hat{P}_0)$ scores to be too high, and hence heavy thresholding should be avoided. Furthermore, cognitive activity is not expected to be fired just after the target onset, that is, variable amounts of delay may obscure periodicities, if any, of the cognitive activity waveforms. In order to illustrate the viability of the LSPE algorithm, we may resort to a simulated data sequence, as shown in Figure 3.4, that consists of the superposition of a hypothetical cognitive activity waveform train embedded in white noise (so that the signal-to-noise ratio is 10 dB) with an actual signal from *A*-band. The cognitive activity waveform is modeled as the centered Gamma function which is frequently used in fMRI data analysis [10]. The average periodicity of cognitive activity

waveforms is set to 40 samples with a random jitter between (-10,10) samples in order to simulate the experimental protocol.

Two cases can be considered prior to the application of the LSPE. In the first case, unfiltered HbO_2 signal (e.g. signal (d) in Figure 3.4) is input to the algorithm; in the second case, in order illustrate the justifiability of prefiltering in the *BC*-band, the prefiltered version takes the role of input (e.g. signal (e) in Figure 3.4). The periodicity index profiles within the (20,60) samples range with and without filtering the synthesized signal, are shown in Figure 3.5. In both cases, the LSPE estimate coincides with the jittered theoretical periodicity of 40 samples, a fact that illustrates the ability of LSPE in tracking jittered periodicities in presence of noise and even additive interference. Using the prior knowledge that the *A*-band does not contain pitch-period like periodicity information, we can get much higher index (or confidence) values by prefiltering the signal in the approptiate band which is the *BC*-band.

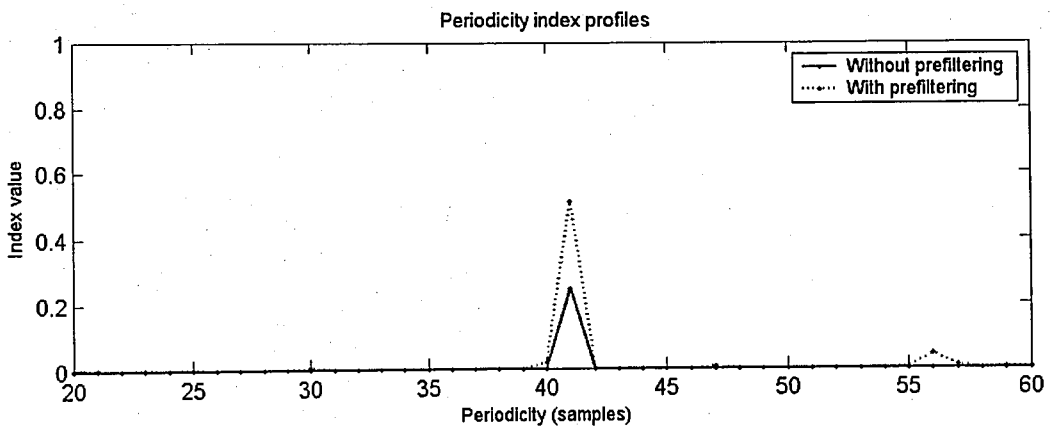

Figure 3.5 Periodicity index profiles for simulated data without prefiltering (solid line) and with prefiltering (dotted line), after local maxima selection and thresholding

On the other hand, the situation with real data is exemplified with two cases as shown in Figure 3.6. In the first case, prefiltering results in a slight increase in the J_1-index value without considerably affecting the value of the detected perodicity (see Figure 3.6 (a), the second plot below is obtained after local maxima selection and thresholding). In the second case where without prefiltering no periodicity can be detected with a high confidence, we observe that a periodicity value, with a much better confidence, emerges within the expected range (see Figure 3.6 (b)).

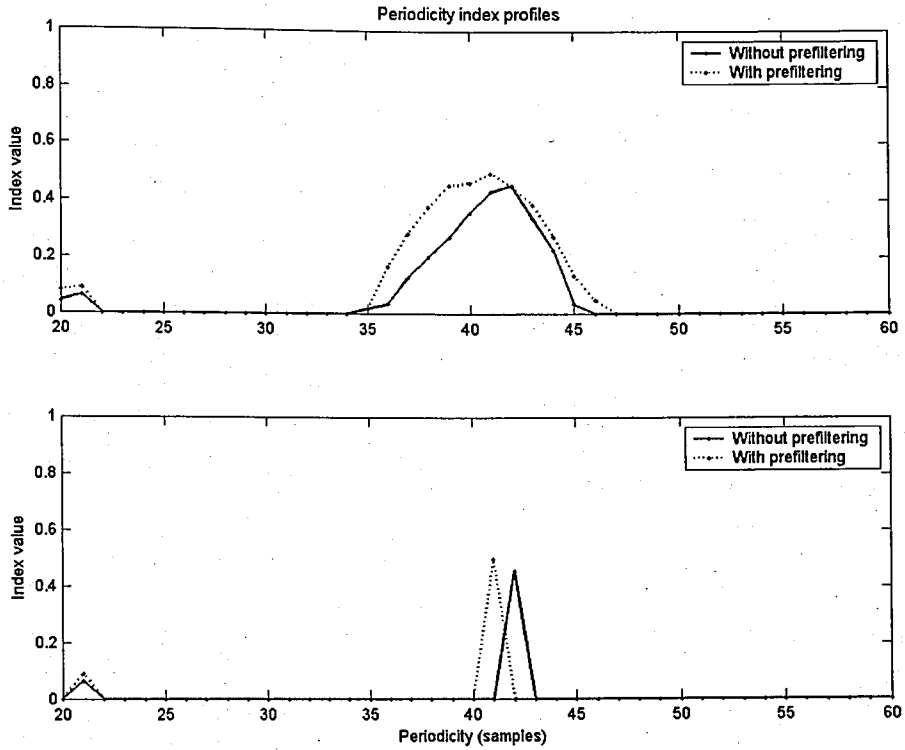

Figure 3.6. (a) Periodicity index profiles of a fNIRS-HbO_2 signal with (dotted line) and without (solid line) prefiltering

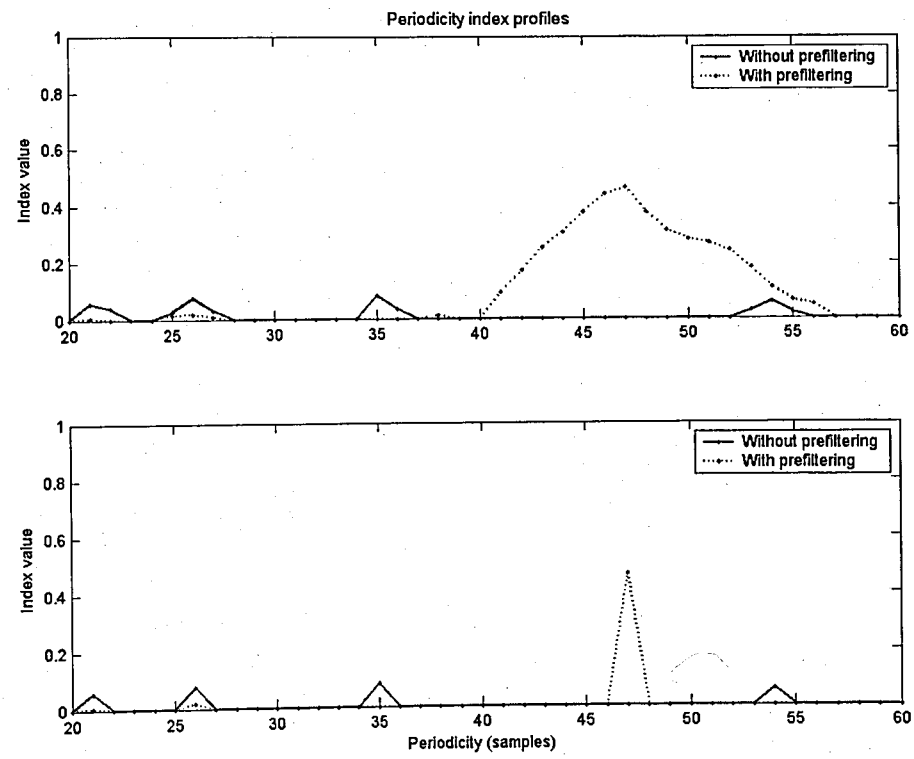

Figure 3.6. (continued) (b) Periodicity index profiles of another fNIRS-HbO_2 signal with (dotted line) and without (solid line) prefiltering

In order to process the real fNIRS-HbO_2 data, it would be wise to proceed as follows. Since the experimental protocol consists of eight identical sessions in succession, the LSPE algorithm can be run session by session, by considering each of the eight time segments of the signal $x(t)$, $t = 1,..., T$ separately. Let's denote each session by the superscript $l = 1,..., 8$ so that $\{x^l(t)\}$ stands for the l^{th} experimental segment of the 30-250 mHz band-pass filtered fNIRS signal from some subject/detector. The session-wise processing of the fNIRS signals helps also to mitigate the non-stationarity. In fact, one can view the signal portions in different sessions as independent realizations of the target-categorization experiment. We now summarize the steps involved in looking for periodicities of HbO_2 signals below.

(i) The periodicity range in which we look for periodicities is (20, 60) samples.

(ii) We look for local maxima of the $J_1(\hat{P}_0)$ function, where once a peak is found no further peak is searched within a neighborhood of (-3, 3) samples.

(iii) We set a threshold of 0.1 on the periodicity belief value $J_1(\hat{P}_0)$.

(iv) For each signal portion, we let the algorithm return the periodicity estimate with the largest J_1-index.

Those $\hat{P}_0$ values that fall within the (30, 50) samples interval are thought to belong to the single-trial cognitive activity sequence in the experiment. Those falling outside are considered as fortuitous values, indicative of the fact that detector is not capturing properly any cognitive activity signal. Since there are 8 time segments $x^l(t)$ per detector, each $x(t)$ signal returns eight period estimates, $\hat{P}_0^l, l = 1,..., 8$ along with their confidence scores. Accumulating separately the scores of the periodicities falling, respectively, inside and outside the expected range, the cumulative score of inside periodicities S_{in} and the count of inside periodicities C_{in} for a given detector and subject can be defined as

$$S_{in} = \sum_{l=1}^{8} J_1(\hat{P}_0^l)\delta(\hat{P}_0^l) \tag{3.12}$$

$$C_{in} = \sum_{l=1}^{8} \delta(\hat{P}_0^l) \tag{3.13}$$

with
$$\delta(\hat{P}_0^l) = \begin{cases} 1 & \text{if } \hat{P}_0^l \text{ is inside the expected range} \\ 0 & \text{if } \hat{P}_0^l \text{ is outside the expected range} \end{cases} \tag{3.14}$$

where l=1,...,8 is the session index. Corresponding expressions for the outside periodicities S_{out} and C_{out} are defined similarly. Furthermore, in order to investigate inter-subject and inter-detector variations of periodicities, two additional quantities are computed: periodicities falling in the proper range averaged over all subjects for a given photodetector, denoted as $\overline{P}_{subjects}(k)$, k = 1,..., 16 and inside periodicity averaged over all photodetectors for a given subject, denoted as $\overline{P}_{detectors}(j)$, j = 1,..., 5. The error bar plots corresponding to these two quantities, $\overline{P}_{subjects}(k)$, k = 1,..., 16 and $\overline{P}_{detectors}(j)$, j = 1,..., 5 are displayed in Figures 3.7 and 3.8. The bar plots of the scores S_{in} and S_{out}, and the scatter plots of the inside and outside periodicities with respect to the photodetector number for different subjects are shown in Figures 3.9-3.13. Several conclusions can be drawn from these results.

(i) The averaged estimated periodicity values match the expected value of P_0 = 40, whether the average is computed over detectors or subjects, as illustrated in Figures 3.7-3.8.

(ii) For any detector or subject there is significant dispersion of estimated periodicity values. The large spread, of the order of 10 per cent in each sense, may be due to the jitter of target instances, to the presence of remaining baseline activity, and to the limited observation interval containing at most eight target stimuli.

(iii) The above described method can be used to classify detectors (or optodes) as responsive of cognitive activity periodicity and the non-responsive ones, that is, those detectors that do not show any evidence of periodicity within the expected range. The discrimination method is based on the not-in-the-range periodicity score S_{out}, as illustrated in Figures 3.9-3.13. The reason why some detectors do not yield conjectured periodicity can be due to the lateralization effect for that subject or simply corrupted measurements. One argument that support lateralization conjecture

is that groups of adjacent detectors all succeed or fail. For example, for Subject 1, detectors 3-12 are "good" (detector 9 was not working though), while detectors 1-2 and 13-15 are "bad" (see Table 3.5 where the indices of responsive photodetectors are shown). One other reason could be due to the location of the optodes with respect to the light sources. Since the source-detector distribution determines the volume of brain being sampled, millimeter range shifts and alignments in the probe will result in a significant change in the brain volume being monitored. Finally, the corruption observed could be due to the skin effects (larger arteries on the skin surface right underneath the optode) dominating the signal.

(iv) There are also marked differences between subjects. For example, Subjects 1, 3 and 4 (especially Subject 4) yields high periodicity scores consistent across all of his/her detectors, while Subjects 2 and 5 are dubious (see Figures 3.9-3.13). Although inter-subject variation is always expected in such studies, there is no standard procedure to isolate corrupted data from statistical analysis for fNIRS signals. The periodicity analysis method provided in this work might be used as a rule of thumb in identifying the corrupted data or the patient that is not cooperating.

The results of the previous subsection together with those of the current one are significant in two aspects. First, the bands of interest in fNIRS-HbO_2 are observed to be localized in the lower part of the spectrum (<250 mHz). The selected canonical bands have a considerable frequency of occurrence hence they are reliable in time-frequency characterization. Second, periodicity detection experiments have exposed that fNIRS indeed measures cognitive activity and prefiltering in the *BC*-band is exceptionally useful. Furthermore, the proposed scheme would be useful in assessing the quality of the measurements.

Table 3.5. Responsive photodetectors such that $S_{in} > S_{out}$

Subject		Photodetector quadruples			
Index	**Alias**	**left (1-4)**	**mid-left (5-8)**	**mid-right (9-12)**	**right (13-16)**
1	**AA005**	3 and 4	5 to 8 (all)	10, 11 and 12	16
2	**GY002**	-not any-	8	9,11 and 12	13 to 16 (all)
3	**KI003**	4	5 to 8 (all)	9 to 12 (all)	15 and 16
4	**KP001**	1 to 4 (all)	5 to 8 (all)	9, 11 and 12	13 to 16 (all)
5	**MJ007**	1 to 4 (all)	5 and 7	9, 11 and 12	13 to 16 (all)

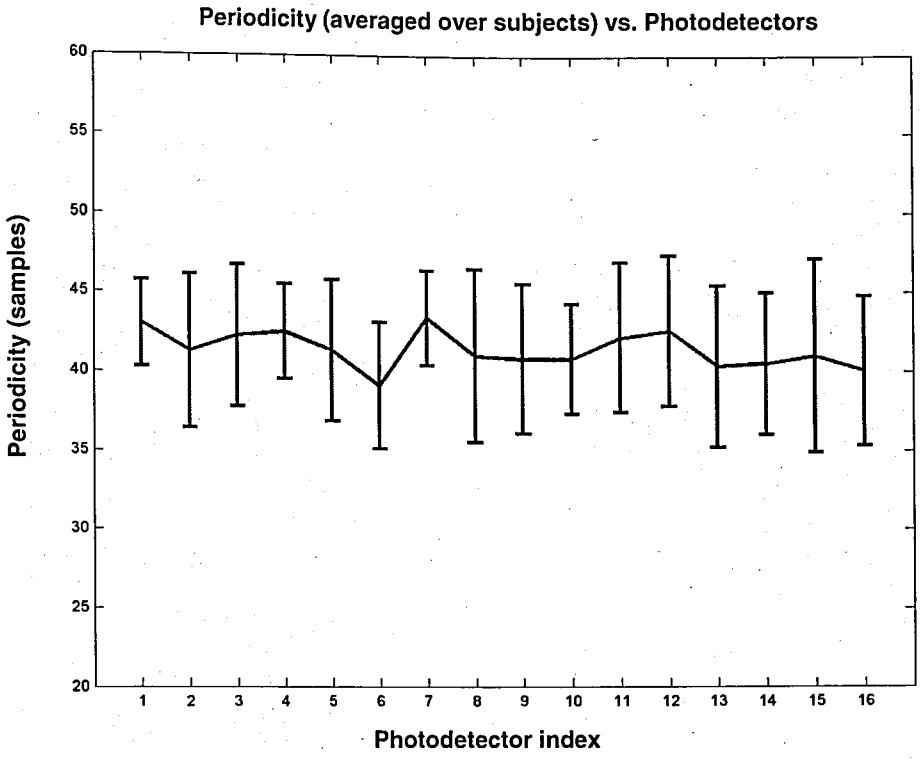

Figure 3.7. Plot of $\overline{P}_{subjects}(k)$ with inter-quartile range bars at data points

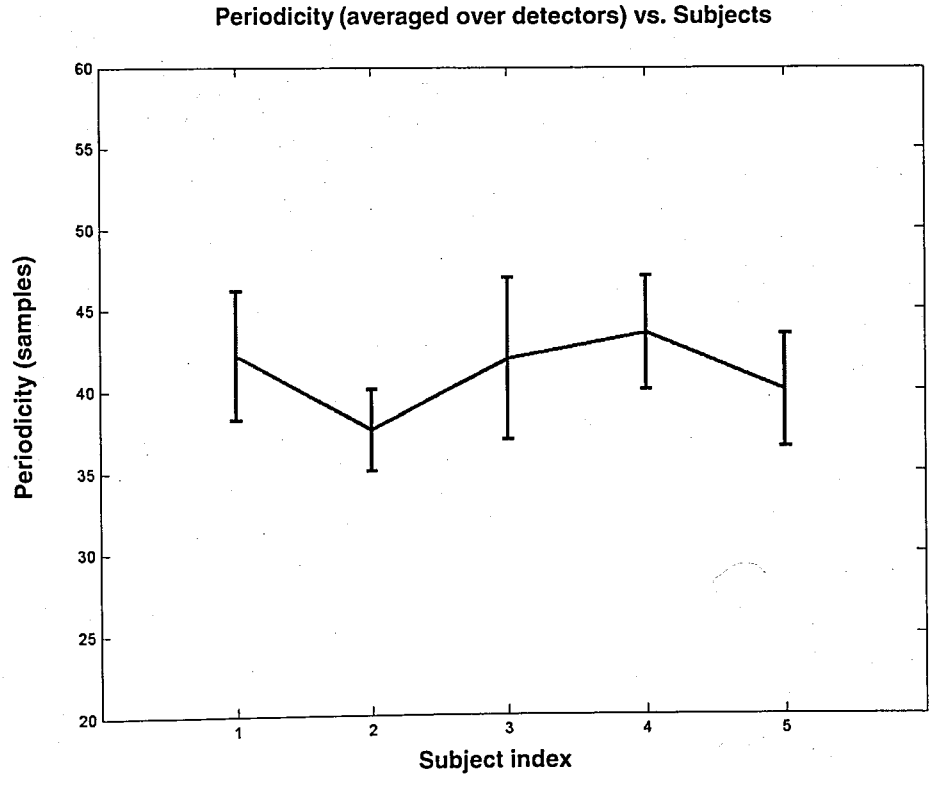

Figure 3.8. Plot of $\overline{P}_{detectors}(j)$ with inter-quartile range bars at data points

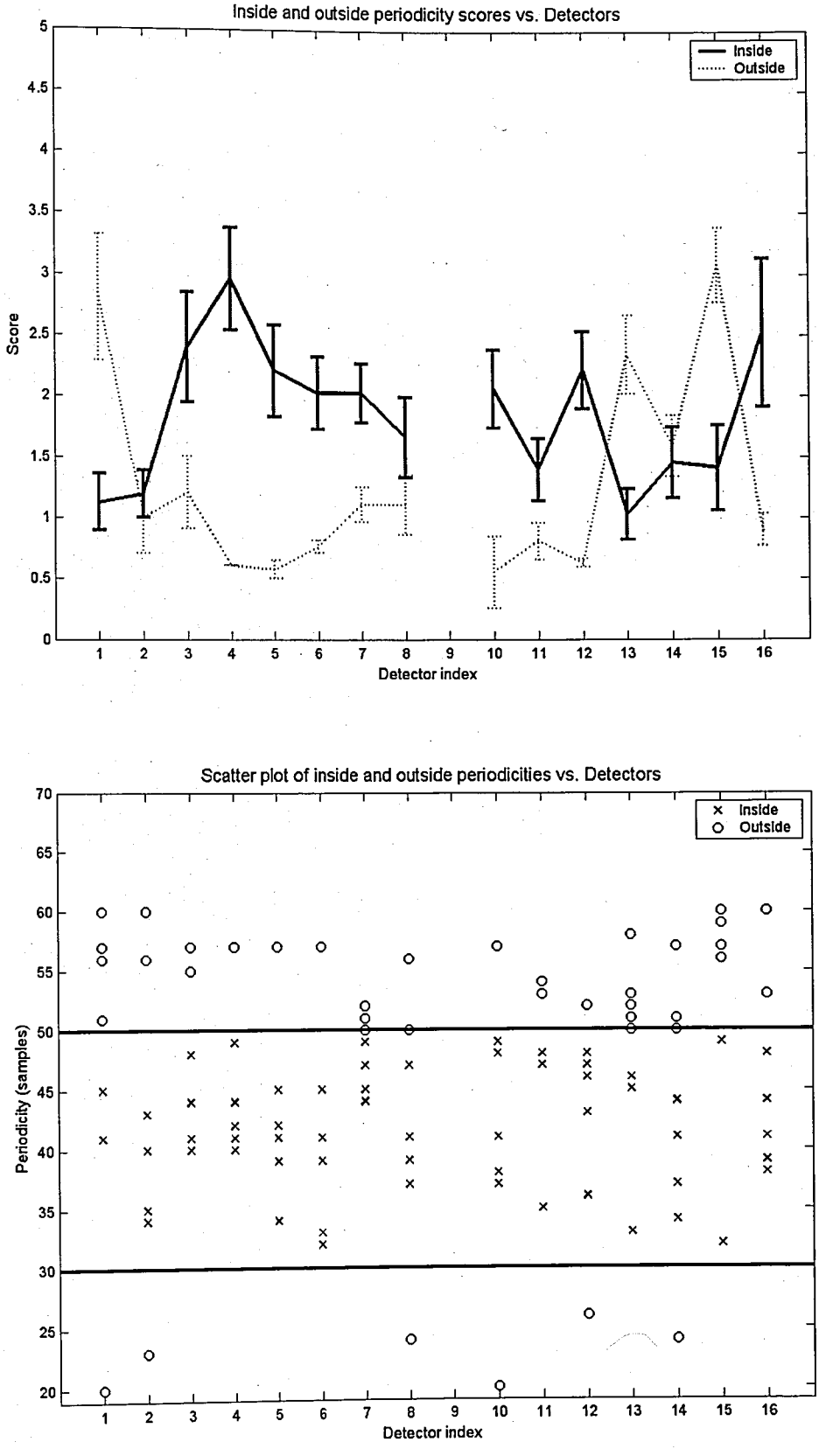

Figure 3.9. Error bar plots of scores vs. detectors with std. dev. bars at data points (top), scatter plots of periodicities vs. detectors (bottom) for Subject 1

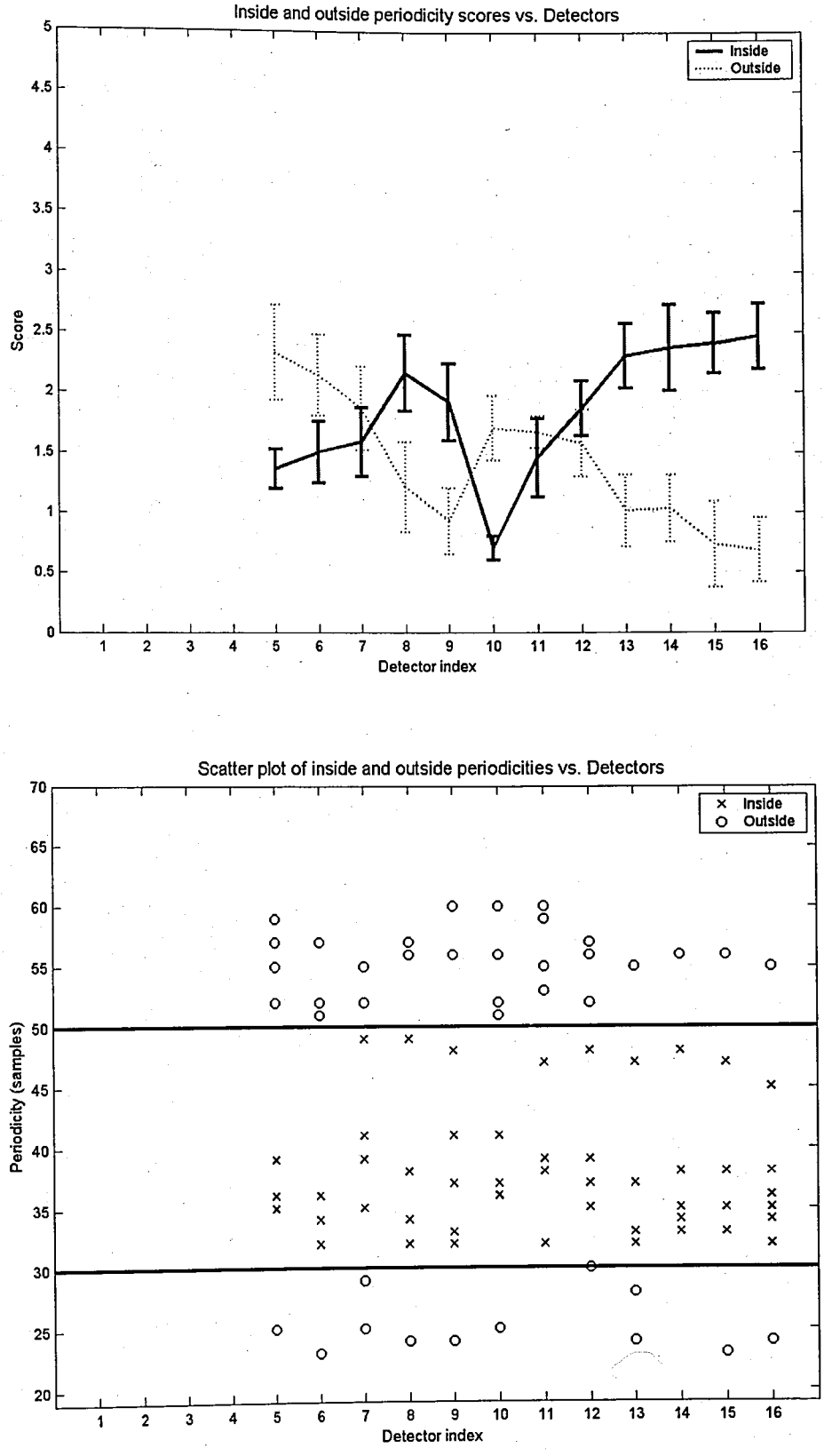

Figure 3.10. Error bar plots of scores vs. detectors with std. dev. bars at data points (top), scatter plots of periodicities vs. detectors (bottom) for Subject 2

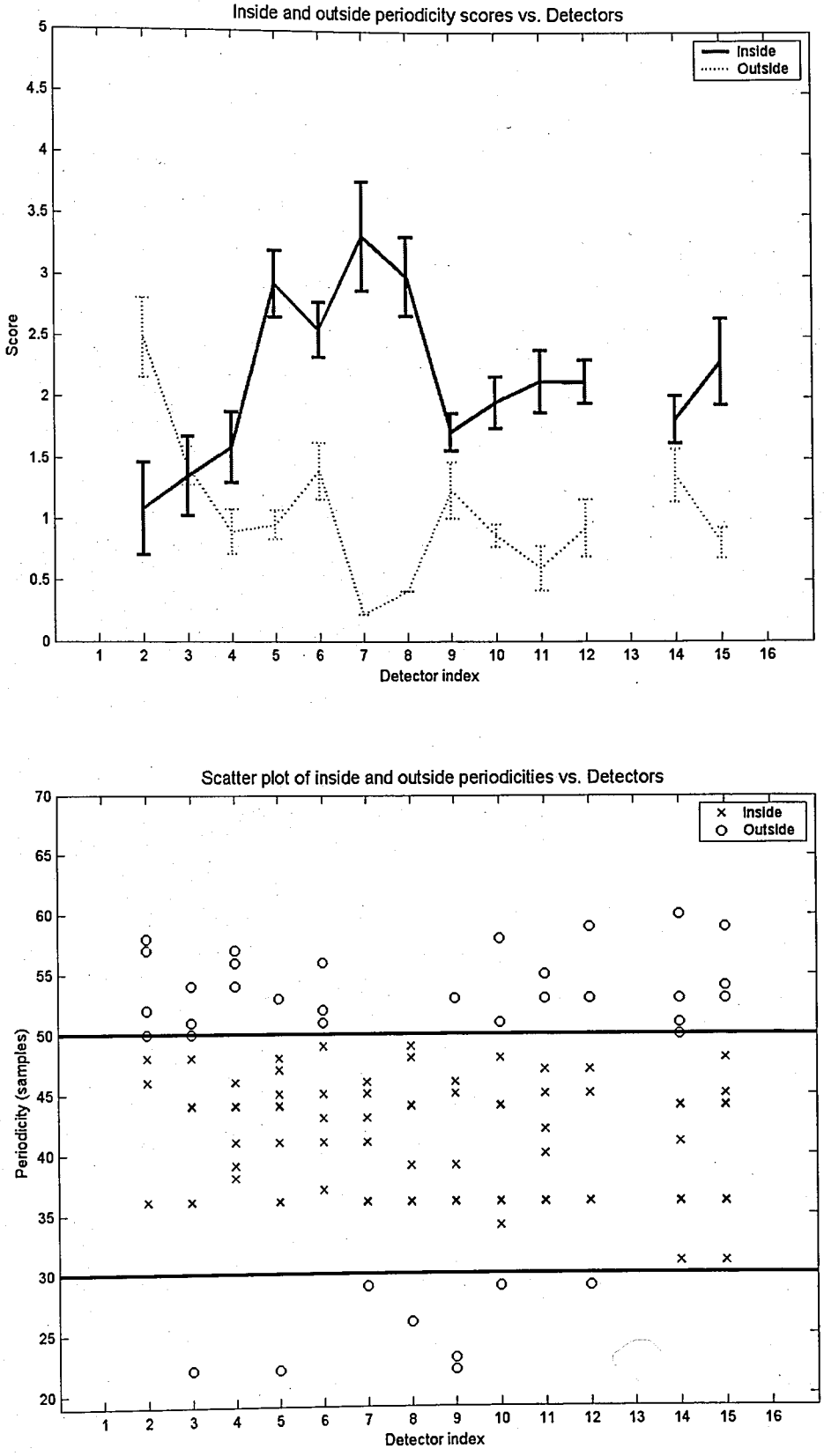

Figure 3.11. Error bar plots of scores vs. detectors with std. dev. bars at data points (top), scatter plots of periodicities vs. detectors (bottom) for Subject 3

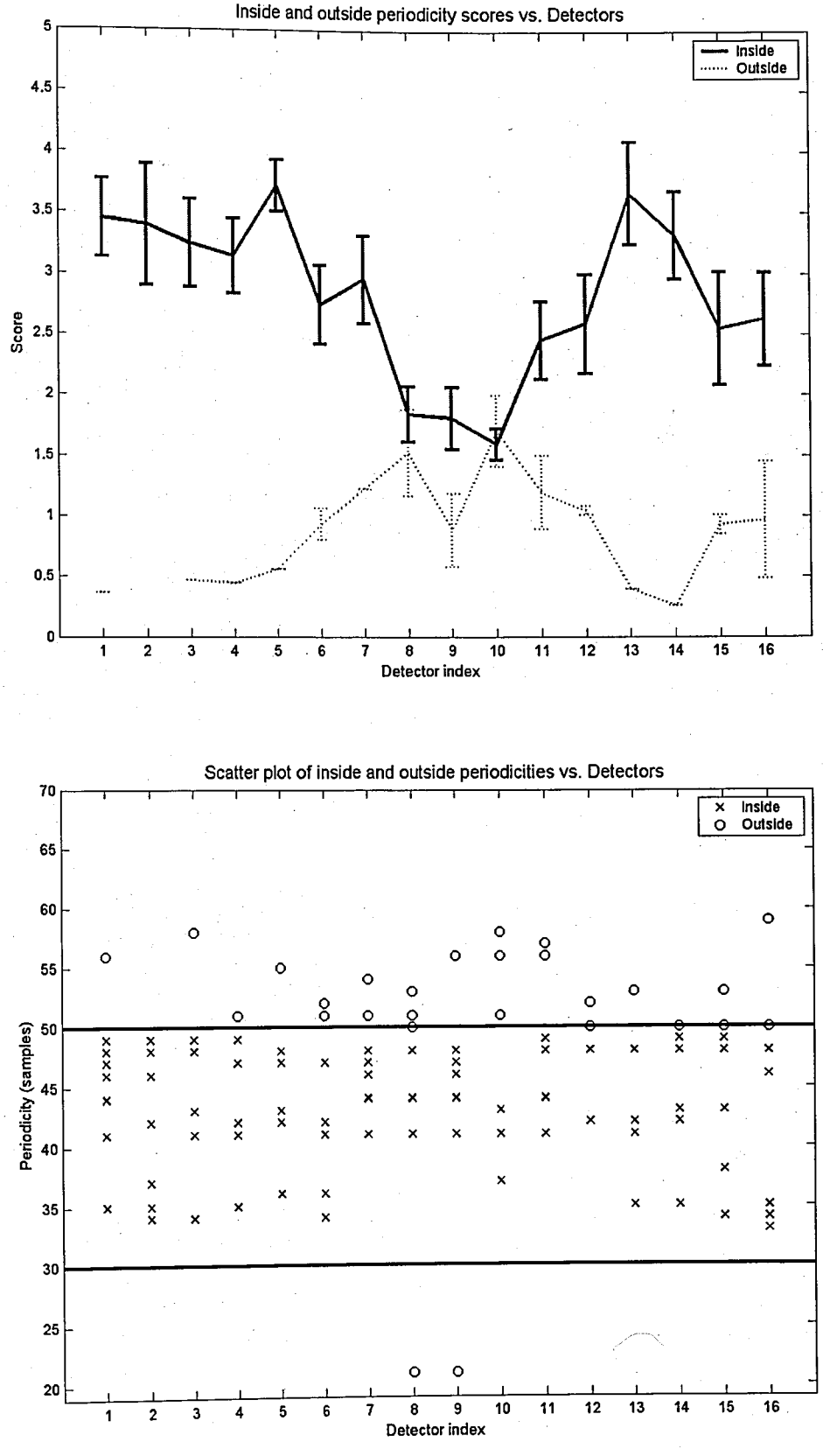

Figure 3.12. Error bar plots of scores vs. detectors with std. dev. bars at data points (top), scatter plots of periodicities vs. detectors (bottom) for Subject 4

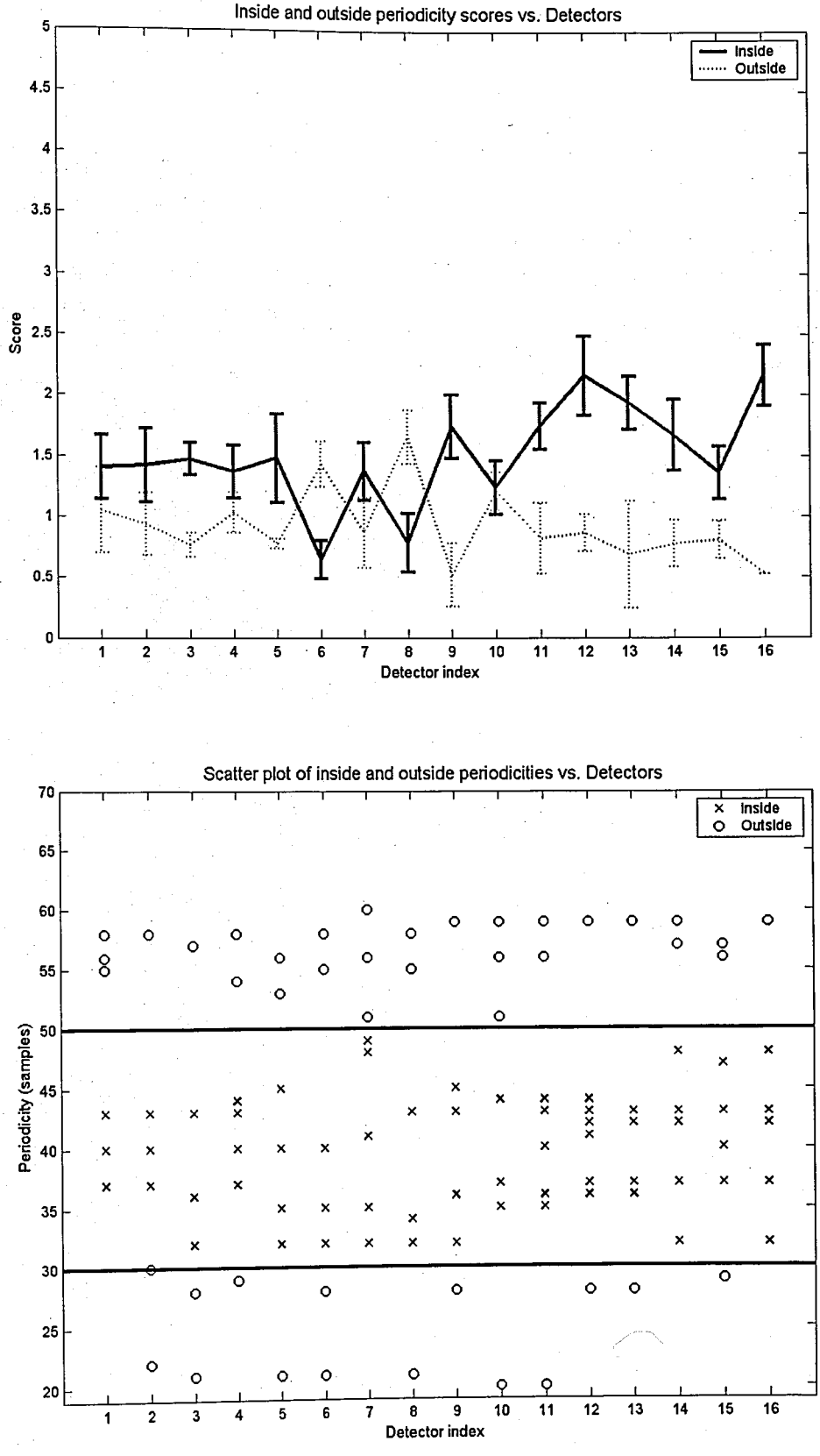

Figure 3.13. Error bar plots of scores vs. detectors with std. dev. bars at data points (top), scatter plots of periodicities vs. detectors (bottom) for Subject 5

4. FUNCTIONAL ACTIVITY ESTIMATION

The purpose of this chapter is to introduce and discuss algorithms for the extraction of waveforms associated with cognitive activity. We consider short-time fNIRS segments (of length m), which consist of the m samples right after the subjects are presented with the target stimuli. We adopt the following notation.

$i = 1, .., I$=64 (total number of targets per experiment I is 64)

$j = 1,..., j_0,..., J$=5 (total number of subjects J is 5)

$k = 1,..., k_0,..., K$=16 (total number of photodetectors for a given subject K is 16)

$\mathbf{x}$: A generic m-dimensional data vector that consists of sequential HbO_2 samples.

X : A generic dataset that consists of multiple realizations of $\mathbf{x}$.

$\mathbf{x}_{k_0}^{j_0}(i)$: A HbO_2 vector from the signal $s_{k_0}^{j_0}(t)$, target location i.

$X_{k_0}^{j_0} = \left\{ \mathbf{x}_{k_0}^{j_0}(i) \,\middle|\, 1 \le i \le I,\ j_0 \text{ fixed}, k_0 \text{ fixed} \right\}$: All the vectors from signal $s_{k_0}^{j_0}(t)$.

$X^{j_0} = \left\{ \mathbf{x}_k^{j_0}(i) \,\middle|\, 1 \le i \le I, 1 \le k \le K,\ j_0 \text{ fixed} \right\}$: All the vectors from Γ^{j_0}.

$X_{k_0} = \left\{ \mathbf{x}_{k_0}^{j}(i) \,\middle|\, 1 \le i \le I, 1 \le j \le J,\ k_0 \text{ fixed} \right\}$: All the vectors from Γ_{k_0}.

$X_{left}^{j_0} = \bigcup_{k=1}^{4} X_k^{j_0}$: All the vectors from *left* photodetectors of subject j_0.

$X_{mid-left}^{j_0} = \bigcup_{k=5}^{8} X_k^{j_0}$: All the vectors from *mid-left* photodetectors of subject j_0.

$X_{mid-right}^{j_0} = \bigcup_{k=9}^{12} X_k^{j_0}$: All the vectors from *mid-right* photodetectors of subject j_0.

$X_{right}^{j_0} = \bigcup_{k=13}^{16} X_k^{j_0}$: All the vectors from *right* photodetectors of subject j_0.

Recall for some values of the index k, the corresponding signal is omitted due to the fact that the measurement is corrupted.

It was noted before that the fNIRS signals exhibit properties similar to fMRI-BOLD signals recorded during functional brain activation, since both modalities measure, although in different ways, hemoglobin agents. It is also assumed that a typical fNIRS segment includes the following.

(i) Cognitive activity related component: "brain hemodynamic response"
(ii) Baseline physiological component
(iii) Higher frequency components
(iv) Noise, movement artifacts

We use independent component analysis (ICA) and clustering as exploratory tools to find out "interesting" waveforms in a generic dataset X [37, 38]. The former decomposes a signal into statistically independent components whereas the latter searches for most commonly occuring "interesting" waveforms (some of which can be associated with cognitive activity), in a multidimensional feature space. In Sections 4.1 and 4.2, both approaches are described in the fNIRS-HbO_2 setting. In Section 4.3, we introduce the preliminaries concerning the experiments. In Sections 4.4 and 4.5, we present the results of ICA and clustering experiments, respectively. The final section discusses the evaluation and comparison of these investigations.

4.1. Independent Component Analysis Approach

Independent component analysis (ICA) can be interpreted as finding a suitable basis for multivariate data (for a brief summary of independent component analysis, see Appendix C). Accordingly, ICA is similar to principal component analysis (PCA) where the basis vectors are ranked in terms of the data variance they account for. In contrast, ICA uses higher order statistical information to find a suitable basis in such a way to maximize statistical independence between projections onto different basis vectors. In formal terms, let $\mathbf{x}$ be an m-dimensional random observation vector, we then want to find a linear transformation $\mathbf{A}$ so that

$$\mathbf{x} = \mathbf{A}\mathbf{s} \tag{4.1}$$

where the components s_i and s_j (of the transformed vector **s**) are statistically "as independent as possible", $i = 1,...,n$; $j = 1,...,n$ so that $i \neq j$ and $n \leq m$. The matrix **A** is the so-called $m \times n$ mixing matrix and the n-dimensional vector **s** is the vector of independent components. We are only given a multivariate dataset $X = \{\mathbf{x}(i) \mid i = 1,...,I\}$ that consists of I realizations of the random vector **x**. The columns of the matrix **A** are said to form an ICA basis that is suitable for representing the observations in the sense explained above. Let's rewrite (4.1) in the following form

$$\mathbf{x} = \begin{bmatrix} \mathbf{a}_1 & \mathbf{a}_2 & \cdots & \mathbf{a}_n \end{bmatrix} \begin{bmatrix} s_1 \\ s_2 \\ \vdots \\ s_n \end{bmatrix} = \mathbf{a}_1 s_1 + \mathbf{a}_2 s_2 + \cdots + \mathbf{a}_n s_n \tag{4.2}$$

Thus, the data vector **x** is decomposed as a linear combination of the columns of **A**, where the weights s_i are the independent components. From this perspective, ICA can be very useful in discovering the underlying nature of many physical phenomena, where observations result from combinations of unrelated or independent activities. However, there are two ambiguities in ICA, which may be annoying for some applications [37]. First, ICA does not provide a natural ordering of the independent components or equivalently of the basis vectors. This is in contrast to PCA where the basis vectors are ordered as a function of data variance they explain. Second, independent components can be estimated up to the sign, that is, we should also consider the negative versions of the estimated components.

It is reasonable to assume, much as in the fMRI studies, that the components (i)-(iv) of fNIRS cited above are mutually independent and that they are linearly combined. This makes the problem suitable for ICA. Accordingly, the basis vectors estimated by ICA will correspond to one or more of the above components. Since observations consist of short-time segments sampled just after the target onsets, it is highly likely that one can estimate a cognitive activity related waveform or the "brain hemodynamic response" in one of the columns of the mixing matrix **A**. The FastICA[3] algorithm is used for that purpose. As a

[3] See Appendix C.

common practice, dimensionality is reduced from m to n by PCA, then the observation vectors with reduced dimensions are whitened, and finally the basis that is spanned by the columns of $\mathbf{A}$ is estimated by maximizing an objective function that "measures" independence. In addition, we remove the ambiguity in the estimated basis vectors, by using a brain hemodynamic response model, traditionally adopted in fMRI analyses, such as the Gamma function.

4.2. Clustering Approach

Another exploratory tool for discovering interesting waveforms related to cognitive activity is clustering the fNIRS signal segments. Clustering[4] is the generic name for the methods that help us to partition a multidimensional dataset into a set of clusters $Q=\{Q_c, \mathbf{q}_c \mid c=1,...,C\}$ where $\mathbf{q}_c$ is the centroid of the cluster Q_c. That is, each observation in the dataset is assigned to one of the clusters Q_c represented by its centroid $\mathbf{q}_c$. In this way, we are able to label the observations and furthermore summarize the data variabilities in terms of cluster centroids.

The fNIRS segments, sampled just after the target presentation, can be clustered to find out typical waveforms that reflect the cognitive activity. To this purpose, we may use the original fNIRS-HbO_2 segments $\mathbf{x}$ directly as input to a clustering algorithm or we may first extract some features. The feature extraction may help in removing noise and redundancy from the raw data. For example, the B-spline approximation is useful in putting into evidence the functional nature of the data and in eliminating irrelevant high-frequency fluctuations, noise and artifacts [39]. B-spline approximation is also known to have superb summarizing property for the waveforms by just using a few coefficients. With these ideas in mind, for all the vectors $\mathbf{x}(i)$ of dimensionality m in a given dataset X, the corresponding B-spline approximation coefficients $\mathbf{y}(i)$ of dimensionality $n \leq m$ are computed. Afterwards, the B-spline feature set $Y=\{\mathbf{y}(i) \mid 1 \leq i \leq I\}$ is input to the clustering algorithm in order to learn the set of clusters Q. Here again, an agglomerative clustering approach is adopted, in other words, we start with a set of clusters where each $\mathbf{y}(i)$ is a singleton cluster, and then group them step by step as described in Appendix B.

[4] See Appendix B.

For the distance metric, we consider the *one-minus-the-normalized correlation coefficient* which is defined by

$$d[\mathbf{y}(i),\mathbf{y}(j)]=1-\frac{\langle \mathbf{y}(i),\mathbf{y}(j)\rangle}{\|\mathbf{y}(i)\|\|\mathbf{y}(j)\|} \tag{4.3}$$

where the vectors $\mathbf{y}(i)$ and $\mathbf{y}(j)$ are made zero-mean by subtracting the mean value of their components. For the closeness criterion, we adopt the *average linkage* which states that the pair of clusters with minimum average distance between their members should be merged at each step. The dendrogram D of the vectors $\mathbf{y}(i)$ is then pruned in order to get the C-cluster set Q. We hope eventually to identify one (or more) of the C-cluster centroids $\mathbf{q}^c$ as cognitive activity related, based possibly on its resemblance to Gamma function. It may turn out that none of the centroids resembles the sought after waveform. This can be due to the fact that the dataset does not contain any cognitive activity related waveform or that the sparse evidence is submerged in some heavy baseline activity.

4.3. Preliminaries for the Experiments

In this section, we discuss two issues: formation of the datasets and ranking the estimated basis vectors.

4.3.1. Formation of the Datasets

We had obseved in Chapter 3 that some of the subjects/photodetectors were more responsive to cognitive activity as measured by fNIRS, as compared to others where the evidence of protocol-induced periodicity was dubious. Specifically, Subjects 1,3 and 4 had yielded higher scores of periodicity in the admissible interval of (30, 50) samples and that the qualified photodetectors followed a more or less regular spatial pattern. Accordingly, we will pay more attention to the subjects/photodetectors in the formation of the datasets and discard those with low periodicity scores (those with dubious evidence of cognitive activity), which are Subjects 2 and 5. For convenience, we replicate Table 3.5, Subjects 2 and 5 omitted, in the sequel.

Table 4.1. Subjects/photodetectors considered in cognitive activity estimation

Subject		Photodetector quadruples			
No.	**Alias**	**left (1-4)**	**mid-left (5-8)**	**mid-right (9-12)**	**right (13-16)**
1	**AA005**	3 and 4	5 to 8 (all)	10, 11 and 12	16
3	**KI003**	4	5 to 8 (all)	9 to 12 (all)	15 and 16
4	**KP001**	1 to 4 (all)	5 to 8 (all)	9, 11 and 12	13 to 16 (all)

Some guidelines to build a dataset for cognitive activity estimation are as follows.

(H1) *Single subject, single quadruple case.* Both inter-subject and inter-quadruple variations are important, hence each photodetector quadruple of a given subject should be treated separately.

(H2) *All detectors case.* We must explore inter-subject variation by grouping together the signals from all photodetectors in forming the dataset of a given subject.

(H3) *All subjects case.* We explore inter-quadruple variation by grouping together the signals from all subjects in forming the dataset of a given quadruple.

According to the guidelines (H1)-(H3), several different datasets can be formed as given in Table 4.2.

Table 4.2. Possible forms of datasets

Subject	Photodetector quadruples				
Index	**left (1-4)**	**mid-left (5-8)**	**mid-right (9-12)**	**right (13-16)**	**all (1-16)**
1	(H1): X^1_{left}	(H1): $X^1_{mid-left}$	(H1): $X^1_{mid-right}$	(H1): X^1_{right}	(H2): X^1
3	(H1): X^3_{left}	(H1): $X^3_{mid-left}$	(H1): $X^3_{mid-right}$	(H1): X^3_{right}	(H2): X^3
4	(H1): X^4_{left}	(H1): $X^4_{mid-left}$	(H1): $X^4_{mid-right}$	(H1): X^4_{right}	(H2): X^4
1,3 and 4	(H3): X_{left}	(H3): $X_{mid-left}$	(H3): $X_{mid-right}$	(H3): X_{right}	

Note that in grouping detectors and/or subjects, we only consider the pruned ones. To explicate Table 4.2., consider for example X_{left}. It is the union of individual datasets $X^{j_0}_{left}$, $j_0 = 1,\ldots,5$. Although after some pruning Subjects 2 and 5 are excluded, let $X^{1,3,4}_{left} \equiv X_{left}$. Similarly, X^1 stands for the union of individual datasets $X^1_{k_0}$, $k_0 = 1,\ldots, 16$, with

uninformative photodetectors duly discarded, either due to the fact that they provided no measurements at all or that they yielded in-range periodicity scores lower than out-of-range periodicity scores. X^1 happens practically to be the union of responsive photodetectors of Subject 1 (the same applies to X^3 and X^4). It is also worth noting that (H2)-type and (H3)-type datasets are large in the number of fNIRS-HbO_2 vectors as compared to (H1)-type datasets.

Another important issue is the selection of the dimensionality m of fNIRS-HbO_2 vectors **x**, that is, the number of samples after the stimulus. A natural choice for m would be the mean inter-target interval (ITI), which is 40 samples. This setting of m is compatible with both theoretical ITI of stimuli sequence and the estimated periodicities of Chapter 3. For both explorations, i.e., ICA and clustering, the training waveform vectors will consist of 40 HbO_2 samples following each target instance.

4.3.2. Ranking the Estimated Vectors

In order to associate ICA basis vectors and/or clustering centroids to some cognitive activity, we require the supervision of an expert or a golden standard. Unfortunately, there is no such a deus-ex-machina, there is even no consensus on the functional form of cognitive activity. Therefore, we refer to a common practice used in fMRI data analysis. We rank the estimated vectors, using a known brain hemodynamic response function model. The Gamma function is one such model defined as

$$h(t) = \begin{cases} A(t-T)^2 e^{-(t-T)/\tau} & \text{for } t \geq T \\ 0 & \text{for } t < T \end{cases} \tag{4.4}$$

where τ is the time-constant that characterizes the response, A is the gain and T is the delay in responding to the target stimulus. The sampled version of this waveform will be denoted by the m-dimensional vector **h** with components h_l sampled at time instances t=0, T_s , ..., (l-1)T_s ,..., (m-1)T_s where T_s is the sampling period. The candidate vectors are ranked based on their matching degree to the waveform in (4.4), after that the parameters A, T and τ are estimated. Let **z** be some estimated m-dimensional vector (either by ICA or

clustering) with components z_l, $l = 1,..., m$. The parameters A, T and τ are estimated by a mean squared error procedure

$$\min_{A,T,\tau} \arg \sum_{l=1}^{m} [z_l - h_l(A,T,\tau)]^2 \tag{4.5}$$

Notice that, A is allowed to take negative values as well to account for the ambiguous sign of the ICA basis vectors. Furthermore the range of values for the remaining parameters, namely T and τ, is constrained. The delay T is constrained to be between zero and a reasonable upper bound, say ~2-3 secs. The time constant τ is constrained to be in the range of (1, 4) seconds. Constrained minimization of (4.5) can be solved by routines readily available in scientific packages (e.g. the Optimization Toolbox in Matlab 6.5). Once the optimum model $\mathbf{h}_o$ is found, the estimated vectors $\mathbf{z}$ can be ranked based on their correlation with $\mathbf{h}_o$. The higher is the correlation value of a vector $\mathbf{z}$ with $\mathbf{h}_o$, the more likely that the response is deemed to be a cognitive activity related waveform.

4.4. Results of the Independent Component Analysis Approach

As discussed in Section 4.1, most ICA algorithms demand dimensionality reduction of data which can be realized by PCA. Thus, after eigendecomposition of the data, only those n projections of multivariate data with the highest variance are kept, so that effectively, the m-dimensional vector $\mathbf{x}$ is transformed into a vector of smaller dimension $n<m$. The subspace dimension n is selected based on proportion of data variance (PoV). When PoV was set to 90 per cent for the fNIRS-HbO_2 vectors n was found to be 4. This subspace projection simplifies the data and removes the high frequency fluctuations and other irrelevant components. Furthermore, n sets an upper limit to the number of independent components or basis vectors that can be estimated by the algorithm. Four basis vectors are also plausible since one can expect one or two cognitive activity related basis vector(s) and the rest to represent the baseline activity. The parameters in the ICA approach are shown in Table 4.3.

Table 4.3. Parameters in ICA experiments

Parameter	Value (or range)
Dimensionality of input vectors m	40
Reduced dimension n	4
Number of basis vectors n	4
Range for delay T	(0,3) seconds or (0,5) samples
Range for time constant τ	(1,4)

To illustrate the case in point, let's consider an (H1)-type dataset, namely $X^4_{mid-left}$, which consists of 256 vectors from mid-left photodetectors of Subject 4 (alias: KP001). In Figure 4.1, the estimated basis vectors are shown in blue curves (red curves correspond to the Gamma functions fit to basis vectors, thick black bars mark the estimated delay). At the top-left, the basis vector that best fits the model function (with a correlation value of 0.90) is displayed. Other basis vectors, in decreasing order, are displayed in the rest of the figure. We believe that an fMRI expert would rank these waveforms in much the same way as given by the correlation measure. In fact the low-ranking waveforms are not at all suited for cognitive activity representation and they must arise from the baseline activity.

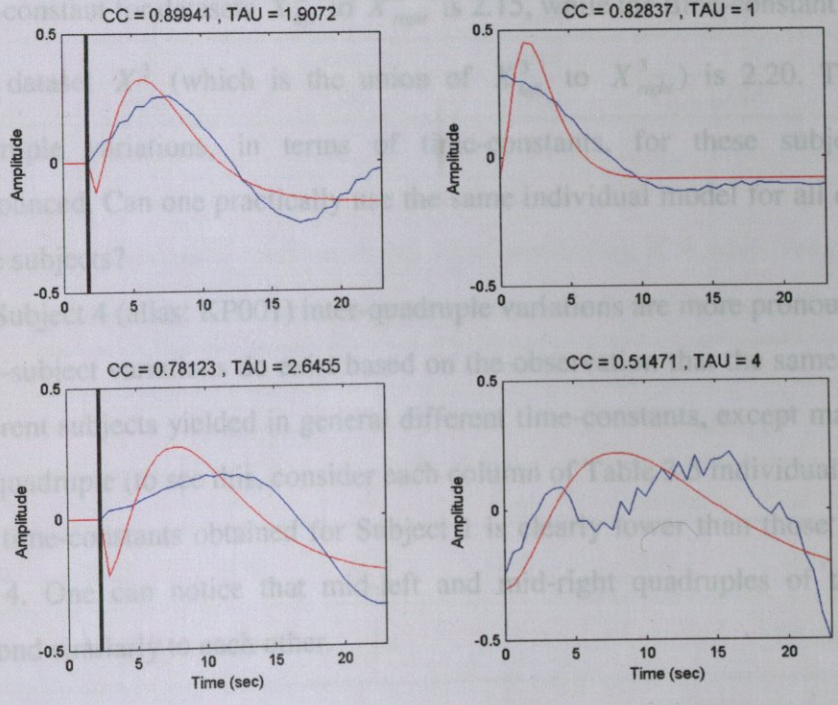

Figure 4.1. Four basis vectors estimated from dataset $X^4_{mid-left}$ using ICA

Table 4.3. Parameters in ICA experiments

Parameter	Value (or range)
Dimensionality of input vectors m	40
Reduced dimension n	4
Number of basis vectors n	4
Range for delay T	(0,3) seconds or (0,5) samples
Range for time constant τ	(1,4)

To illustrate the case in point, let's consider an (H1)-type dataset, namely $X^4_{mid-left}$, which consists of 256 vectors from mid-left photodetectors of Subject 4 (alias: KP001). In Figure 4.1, the estimated basis vectors are shown in blue curves (red curves correspond to the Gamma functions fit to basis vectors, thick black bars mark the estimated delay). At the top-left, the basis vector that best fits the model function (with a correlation value of 0.90) is displayed. Other basis vectors, in decreasing order, are displayed in the rest of the figure. We believe that an fMRI expert would rank these waveforms in much the same way as given by the correlation measure. In fact the low-ranking waveforms are not at all suited for cognitive activity representation and they must arise from the baseline activity.

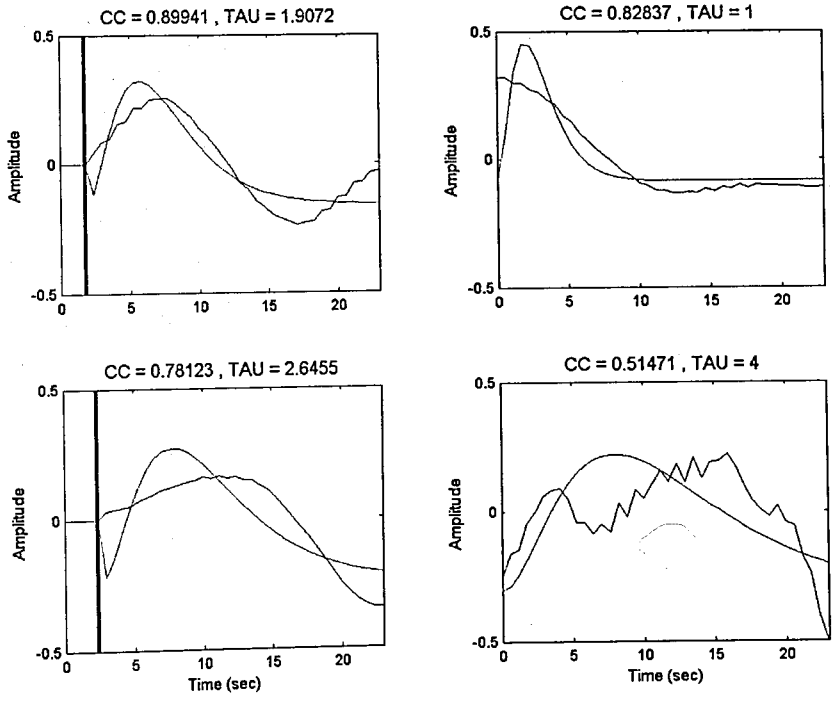

Figure 4.1. Four basis vectors estimated from dataset $X^4_{mid-left}$ using ICA

Table 4.4 summarizes the quality of fit for basis vectors estimated from (H1)-type datasets. We report only the correlation coefficients of the best-fitting vectors. In all cases, the correlation coefficient is on the order of 0.9, suggesting that ICA yielded indeed conjectured type of cognitive activity waveforms. The estimated time-constants of Gamma functions, as a by-product, may be of particular interest for computational neuroscientists (see Table 4.5).

In Table 4.6, we give, for (H2) and (H3)-type datasets, the correlation scores between the best-fitting basis vectors and corresponding Gamma models as well as the estimated time-constants. Note that correlation scores have slightly decreased for larger datasets (i.e. H(2) and (H3)-type). Let's comment and raise questions based on the results given in Tables 4.4-4.6.

(i) For Subjects 1 (alias: AA005) and 3 (alias: KI003), all quadruples yield Gamma fits with close time-constants. The mean time-constant for datasets X^1_{left} to X^1_{right} is 1.26 (see Table 4.5). Interestingly, the time-constant for the (H2)-type dataset X^1 (which is the union of X^1_{left} to X^1_{right}) is 1.44 (see Table 4.6). Similarly, the mean time-constant for datasets X^3_{left} to X^3_{right} is 2.15, while the time-constant for the (H2)-type dataset X^3 (which is the union of X^3_{left} to X^3_{right}) is 2.20. That is, inter-quadruple variations, in terms of time-constants, for these subjects are not pronounced. Can one practically use the same individual model for all quadruples of these subjects?

(ii) For Subject 4 (alias: KP001) inter-quadruple variations are more pronounced.

(iii) Inter-subject variations do exist based on the observation that the same quadruple of different subjects yielded in general different time-constants, except maybe the mid-left quadruple (to see this, consider each column of Table 3.5 individually).

(iv) The time-constants obtained for Subject 1 is clearly lower than those of Subjects 3 and 4. One can notice that mid-left and mid-right quadruples of these subjects respond similarly to each other.

Table 4.4. Correlation coefficients between best-fitting ICA basis vectors and corresponding Gamma models for (H1)-type datasets

Subject		Photodetector quadruples					
No.	Alias	left (1-4)	mid-left (5-8)	mid-right (9-12)	right (13-16)	Mean	Std. Dev.
1	AA005	0.96	0.93	0.91	0.94	0.93	0.02
3	KI003	0.88	0.89	0.96	0.91	0.91	0.04
4	KP001	0.93	0.90	0.90	0.90	0.91	0.01
Mean		0.92	0.91	0.92	0.92		
Std. Dev.		0.04	0.02	0.03	0.02		

Table 4.5. Time-constants of Gamma models to best-fitting ICA basis vectors for (H1)-type datasets

Subject		Photodetector quadruples					
No.	Alias	left (1-4)	mid-left (5-8)	mid-right (9-12)	right (13-16)	Mean	Std. Dev.
1	AA005	1.22	1.28	1.37	1.17	1.26	0.08
3	KI003	2.27	1.72	2.60	2.03	2.15	0.37
4	KP001	3.27	1.91	2.44	1.41	2.26	0.80
Mean		2.25	1.64	2.14	1.54		
Std. Dev.		1.03	0.32	0.67	0.44		

Table 4.6. Correlation coefficients between best-fitting ICA basis vectors and corresponding Gamma models, best-fitting time-constants for (H2) and (H3)-type datasets

	Dataset						
	(H2)-type			(H3)-type			
	X^1	X^3	X^4	X_{left}	$X_{mid-left}$	$X_{mid-right}$	X_{right}
Correlation	0.88	0.95	0.89	0.93	0.91	0.77	0.91
Time-constant	1.44	2.20	1.38	1.3569	4	1.5162	4

Remind ourselves that Gamma time-constant is but one of the aspects of data and that one can still glean more information from a visual investigation of the best-fitting basis vectors. Figs 4.2 and 4.3 are two different ways of looking at the plots of best-fitting ICA basis vectors for (H1)-type datasets. Figure 4.2 displays them on a subject-by-subject basis in order to evaluate inter-quadruple variations. One can see that, per quadruple, the time responses are essentially similar and stable over subjects. Subject 4 (alias: KP001), presents only the slight exception in that its left quadruple responds with a larger time-constant. Figure 4.3 also shows that, on a subject-by-subject comparison, all of the quadruples of Subject 1 responds in a very distinct way compared with Subjects 3 and 4. The mid-left quadruples of the latter respond similarly as well as their mid-right quadruples.

Figures 4.4 (a) and (b) exhibit the best-fitting ICA waveforms for (H2) and (H3)-type datasets, respectively. Figures 4.4 (a) illustrates inter-subject variation, notice for example Subject 1 has a more agile response compared to the others while Subject 3 has the most sluggish one. Actually, Subjects 3 and 4 have similar responses in selected quadruples, i.e., middle ones, while the ensemble of all their quadruples is considered, they appear different. In Figure 4.4 (b), we wanted to bring forward inter-quadruple dissimilarities. It can be seen that all quadruples have distinct responses. The idea of merging all subjects into one dataset may not be a good idea after all as inter-subject variations will be a nuisance factor when observing inter-detector variations. Therefore, Figure 4.4 (b) should be interpreted with caution, as it shows quadruple responses "averaged" over subjects.

In summary, ICA proves to be a viable scheme in extracting cognitive activity related waveforms, whether observed per detector group or whether averaged over all subjects or detectors.

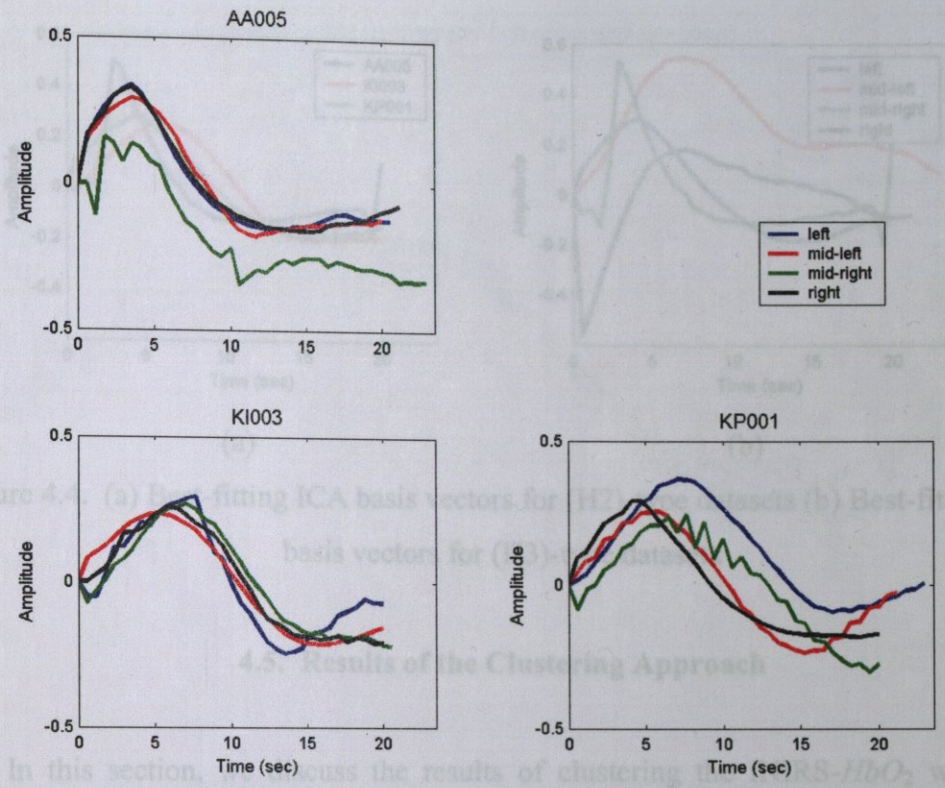

Figure 4.2. Best-fitting ICA basis vectors for (H1)-type datasets shown subject-by-subject.

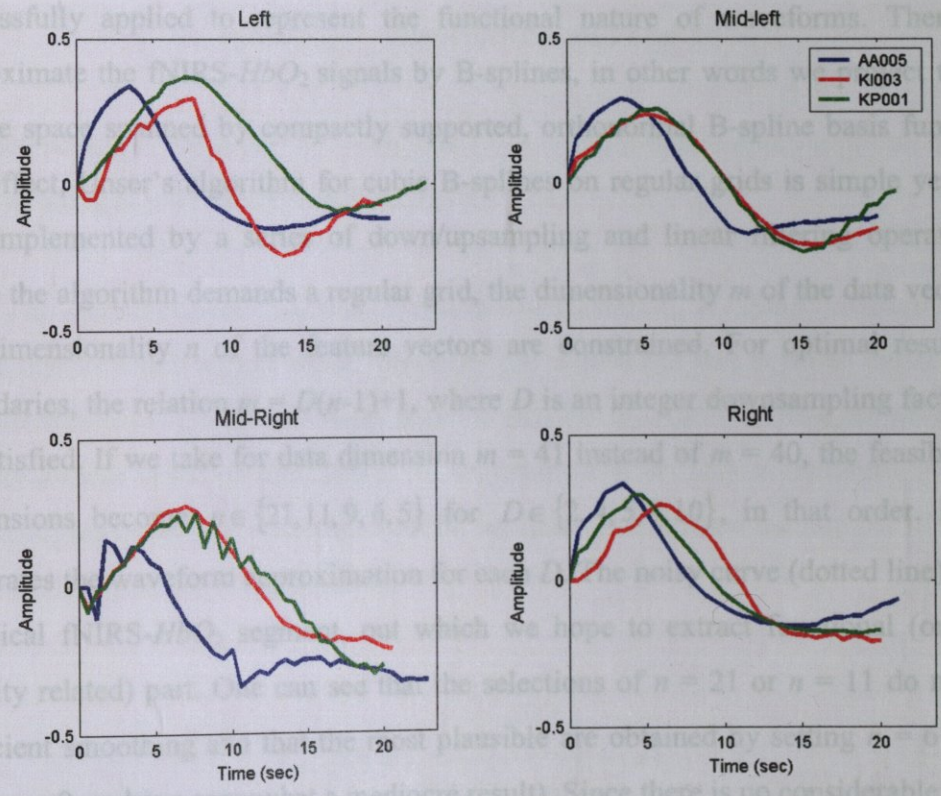

Figure 4.3. Best-fitting ICA basis vectors for (H1)-type datasets shown quadruple-by-quadruple.

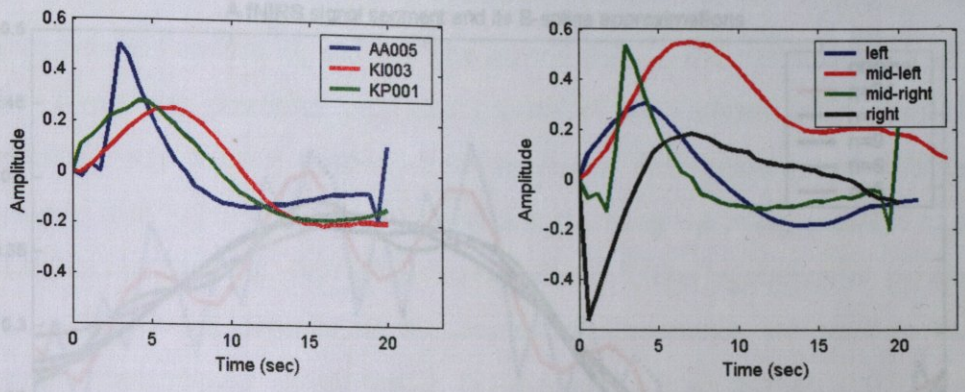

(a) (b)

Figure 4.4. (a) Best-fitting ICA basis vectors for (H2)-type datasets (b) Best-fitting ICA basis vectors for (H3)-type datasets

4.5. Results of the Clustering Approach

In this section, we discuss the results of clustering the fNIRS-HbO_2 waveforms. Waveform clustering algorithms in the literature first obtain a parametric representation of the waveform and then cluster this parameter vector [39]. B-spline approximation has been successfully applied to represent the functional nature of waveforms. Therefore, we approximate the fNIRS-HbO_2 signals by B-splines, in other words we project the signals on the space spanned by compactly supported, orthonormal B-spline basis functions. To this effect, Unser's algorithm for cubic B-splines on regular grids is simple yet efficient, and implemented by a series of down/upsampling and linear filtering operations [40]. Since the algorithm demands a regular grid, the dimensionality m of the data vectors $\mathbf{x}$ and the dimensionality n of the feature vectors are constrained. For optimal results on the boundaries, the relation $m = D(n-1)+1$, where D is an integer downsampling factor, should be satisfied. If we take for data dimension $m = 41$ instead of $m = 40$, the feasible reduced dimensions become $n \in \{21, 11, 9, 6, 5\}$ for $D \in \{2, 4, 5, 8, 10\}$, in that order. Figure 4.5 illustrates the waveform approximation for each D. The noisy curve (dotted line) stands for a typical fNIRS-HbO_2 segment, out which we hope to extract functional (or cognitive activity related) part. One can see that the selections of $n = 21$ or $n = 11$ do not provide sufficient smoothing and that the most plausible are obtained by setting $n = 6$ and $n = 5$ (with $n = 9$ we have somewhat a mediocre result). Since there is no considerable difference

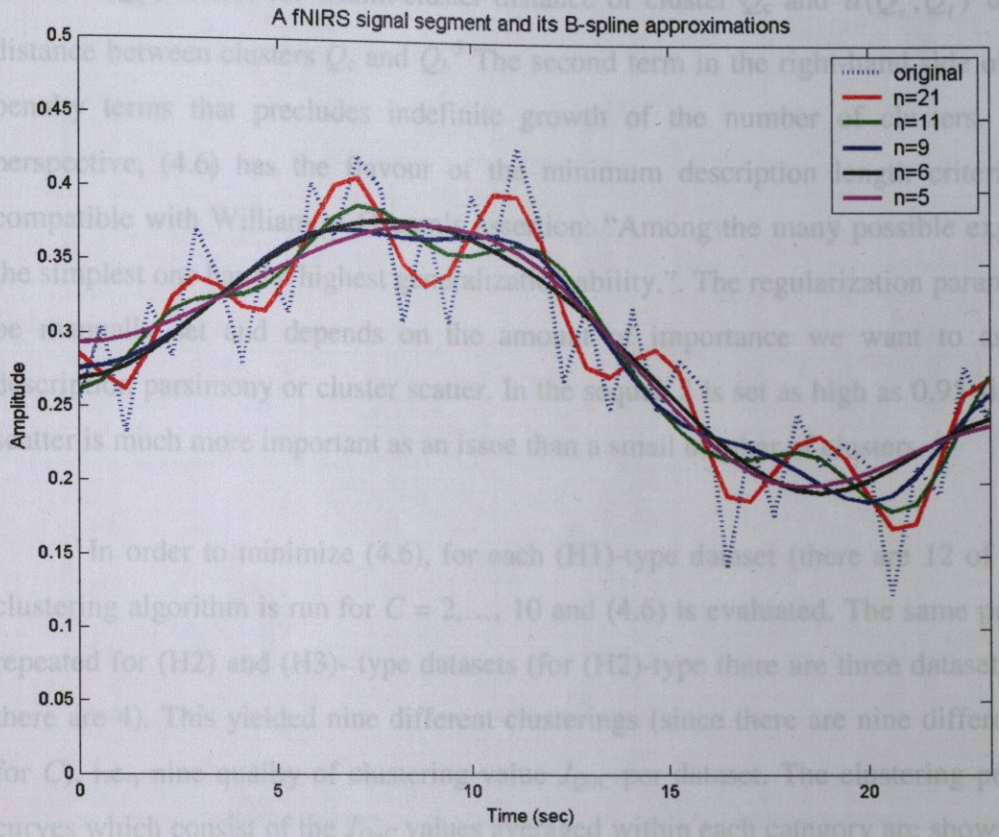

Figure 4.5. A noisy fNIRS-HbO_2 signal segment (vector) and its corresponding cubic B-spline approximations for various values of n

between setting $n = 6$ or $n = 5$, we choose $n = 5$ cubic B-spline approximation coefficients for explaining $m = 41$ dimensional vectors $\mathbf{x}$.

The second critical choice is the number of clusters C. A "good" clustering is said to be the one in which within cluster distances are minimized and between cluster distances are maximized [41], with minimum possible number of clusters. There are several cluster validity indices based on this idea in the multivariate data analysis literature, [42]-[44]. In this work, we consider a heuristic criterion function to determine the number of clusters C. The criterion function is expressed as

$$J_{QoC}(C) = \lambda \frac{\sum_{c=1}^{C} S(Q_c)}{\sum_{c=1}^{C} \sum_{l=1, l \neq c}^{C} d(Q_c, Q_l)} + (1-\lambda)C \qquad (4.6)$$

where $S(Q_c)$ stands for within-cluster distance of cluster Q_c and $d(Q_c, Q_l)$ denotes the distance between clusters Q_c and Q_l.[5] The second term in the right-hand side of (4.6) is a penalty terms that precludes indefinite growth of the number of clusters. From this perspective, (4.6) has the flavour of the minimum description length criterion and is compatible with William of Occam's assertion: "Among the many possible explanations, the simplest one has the highest generalization ability.". The regularization parameter λ can be manually set and depends on the amount of importance we want to associate to description parsimony or cluster scatter. In the sequel, λ is set as high as 0.95 since cluster scatter is much more important as an issue than a small number of clusters.

In order to minimize (4.6), for each (H1)-type dataset (there are 12 of them), the clustering algorithm is run for $C = 2,\ldots, 10$ and (4.6) is evaluated. The same procedure is repeated for (H2) and (H3)- type datasets (for (H2)-type there are three datasets, for (H3) there are 4). This yielded nine different clusterings (since there are nine different choices for C), i.e., nine quality of clustering value J_{QoC} per dataset. The clustering performance curves which consist of the J_{QoC} values averaged within each category are shown in Figure 4.6. For completeness, J_{QoC}-curve averaged over all possible 19 datasets is also provided. Due to the lack of data, we could not perform validation tests for generalization purposes. The results here are tuned to the training data and it remains to be seen whether they are valid for any other realizations (of these types of datasets). Figure 4.6 suggests that a setting of $C = 4$ or $C = 5$ is satisfactory. In the sequel, we take $C = 5$ since we observe that it sometimes gives better results than the choice of $C = 4$. Table 4.7 summarizes the parameters used in clustering experiments.

Tables 4.8 to 4.11 display the major findings of clustering experiments. The number of members per cluster gives an idea about how the input vectors (B-spline coefficient vectors $\mathbf{y}$) are distributed over the estimated clusters (see Table 4.8 for (H1)-type datasets and see Table 4.10 for (H2) and (H3)-type datasets). The vectors are more or less evenly distributed, i.e., there are no over-populated or under-populated cluster s. Interestingly, the centroids of the largest clusters (in terms of the number of members) need not always be the best-fitting one. In other words, the population assigned to the centroid represented by the best Gamma approximation ranked low, e.g., fourth or fifth,

[5] See Appendix B for explicit definitions of these quantities.

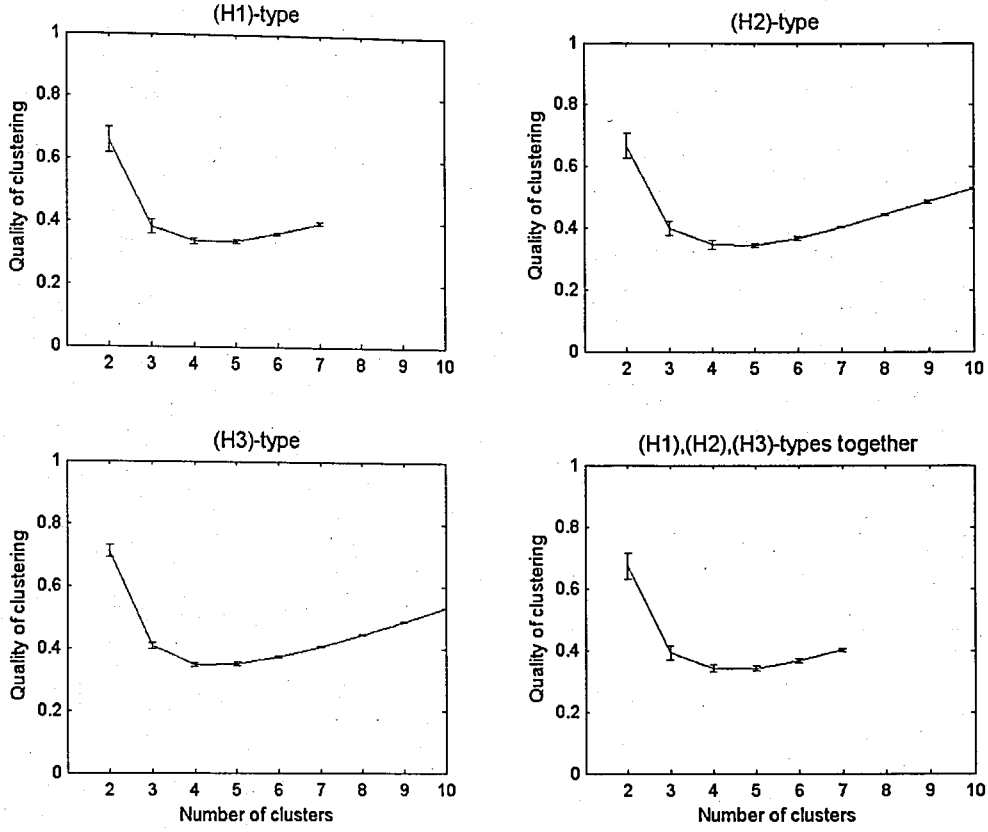

Figure 4.6. J_{QoC}-curves averaged over (H1)-type datasets (top left), over (H2)-type datasets (top right), over (H3)-type datasets (bottom left), over all datasets (bottom right).

Table 4.7. Parameters in clustering experiments

Parameter	Value (or range)
Dimensionality of input vectors m	41
Reduced dimension n	5
Number of clusters C	5
Distance metric	One-minus-the-normalized correlation coefficient
Closeness criterion	Average linkage
Range for delay T	(0,3) seconds or (0,5) samples
Range for time constant τ	(1,4)

especially in the (H2) and (H3)-type datasets. Thus not all the input waveforms following a stimulus can be expected to reflect the hemodynamic behaviour. Instead, the interference from the baseline may be more pronounced, or the subject may have not even responded to the corresponding target. On the other hand, in terms of cluster quality, all datasets yield equivalent results. Tables 4.9 and 4.11 indicate that, at $C = 5$, the value of the clustering

index J_{QoC} becomes 0.34 for almost all cases. This fact was already illustrated in Figure 4.6.

Table 4.8. Number of cluster members for (H1)-type datasets

Dataset	Cluster					Total number of samples
	Q_1	Q_2	Q_3	Q_4	Q_5	
X^1_{left}	37	36	23	19	13	128
$X^1_{nid-left}$	81	63	55	50	7	256
$X^1_{mid-right}$	65	59	33	28	7	192
X^1_{right}	20	19	9	8	8	64
X^3_{left}	19	19	13	11	2	64
$X^3_{nid-left}$	100	46	46	44	20	256
$X^3_{mid-right}$	80	68	53	28	27	256
X^3_{right}	48	46	20	8	6	128
X^4_{left}	88	58	41	40	29	256
$X^4_{nid-left}$	98	64	44	27	23	256
$X^4_{mid-right}$	69	50	44	16	13	192
X^4_{right}	67	59	55	44	31	256

Shaded rows correspond to centroids that are best-fitting in terms of the correlation with corresponding Gamma fits

Table 4.9. Quality of clustering values for (H1)-type datasets

Subject		Photodetector quadruples					
No.	Alias	left (1-4)	mid-left (5-8)	mid-right (9-12)	right (13-16)	Mean	Std. Dev.
1	AA005	0.34	0.33	0.34	0.32	0.33	0.01
3	KI003	0.34	0.34	0.34	0.33	0.34	0.00
4	KP001	0.35	0.33	0.34	0.35	0.34	0.01
Mean		0.34	0.33	0.34	0.33		
Std. Dev.		0.00	0.00	0.00	0.01		

Table 4.10. Number of cluster members for (H2) and (H3)-type datasets

Dataset		Cluster					Total number of samples
		Q_1	Q_2	Q_3	Q_4	Q_5	
(H2)-type	X^1	198	169	149	106	18	640
	X^3	277	219	127	44	37	704
	X^4	245	212	183	175	145	960
(H3)-type	X_{left}	139	99	77	73	60	**448**
	$X_{nid-left}$	260	237	143	75	53	**768**
	$X_{mid-right}$	205	185	109	87	54	**640**
	X_{right}	141	106	73	71	57	448

Shaded rows correspond to centroids that are best-fitting in terms of the correlation with corresponding Gamma fits

Table 4.11. Quality of clustering values for (H2) and (H3)-type datasets

	Dataset						
	(H2)-type			(H3)-type			
	X^1	X^3	X^4	X_{left}	$X_{mid-left}$	$X_{mid-right}$	X_{right}
J_{QoC}-value	0.34	0.34	0.35	0.35	0.35	0.35	0.34

In Tables 4.12-4.14, we give the correlation scores of the best-fitting waveforms with corresponding Gamma models and the estimated time-constants. Observations are in the sequel.

(i) In general, correlation scores for (H1)-type small datasets are not too high and they fluctuate. For instance, we see that for left and mid-right photodetectors of Subject 3 (alias: KI003) in Table 4.12, the correlation score become as low as 0.69.

(ii) The most consistent quadruple in terms of the time-constants is the mid-right one, however correlation values (~0.82) for corresponding datasets $X^j_{mid-right}$, $j = 1, 3, 4$ are mediocre.

(iii) The most consistent subject in terms of the time-constants is Subject 3 (alias: KP001). Interestingly, left and mid-right quadruples have proven to give better correlation values (~0.97) than those of the remainder for this subject (~0.81).

(iv) The most consistent quadruple in terms of the correlation scores is the right one, however correlation values (~0.85) for corresponding datasets X^{j}_{right}, $j = 1, 3, 4$ are mediocre.

(v) The most consistent subject in terms of the correlation scores is Subject 1 (alias: AA005). Interestingly, photodetector quadruples of left hemisphere have proven to give better correlation values (~0.95) than those of the right one for that subject (~0.85).

(vi) For larger datasets, the most satisfactory results came from Subject 4 (alias: KP001, X^{4} of (H2)-type) with a correlation value of 0.91 and from left and mid-left quadruples (X_{left} and $X_{mid-left}$ of (H3) type) with perfect matches (correlation values of 1.00 and 0.99 respectively).

(vii) There exist significant standard deviations in Table 4.13 both for inter-subject and inter-quadruple observations.

(viii) Much in the same way as in Table 3.6 for ICA analysis, we observe that there are significant differences in the estimated waveforms among subjects and among detector quadruples (see Table 4.14).

Table 4.12. Correlation coefficients between best-fitting cluster centroids and corresponding Gamma models for (H1)-type datasets

Subject		**Photodetector quadruples**					
No.	**Alias**	**left (1-4)**	**mid-left (5-8)**	**mid-right (9-12)**	**right (13-16)**	**Mean**	**Std. Dev.**
1	**AA005**	0.98	0.93	0.83	0.87	0.90	0.06
3	**KI003**	0.68	0.93	0.69	0.86	0.79	0.12
4	**KP001**	1.00	0.78	0.94	0.83	0.89	0.10
Mean		0.88	0.88	0.82	0.85		
Std. Dev.		0.18	0.08	0.12	0.02		

Table 4.13. Time-constants of Gamma models to best-fitting cluster centroids for (H1)-type datasets

Subject		Photodetector quadruples					
No.	Alias	left (1-4)	mid-left (5-8)	mid-right (9-12)	right (13-16)	Mean	Std. Dev.
1	AA005	2.93	1.41	1.57	3.51	2.35	1.03
3	KI003	1.20	1.49	1.40	2.60	1.67	0.63
4	KP001	2.11	1.88	1.60	1.39	1.75	0.31
Mean		2.08	1.59	1.52	2.50		
Std. Dev.		0.86	0.25	0.11	1.06		

Table 4.14. Correlation coefficients between best-fitting cluster centroids and corresponding Gamma models, best-fitting time-constants for (H2) and (H3)-type datasets

	Dataset						
	(H2)-type			(H3)-type			
	X^1	X^3	X^4	X_{left}	$X_{mid-left}$	$X_{mid-right}$	X_{right}
Correlation	0.87	0.75	0.91	1.00	0.99	0.71	0.85
Time-constant	3.52	1.79	2.95	2.34	1.97	1.11	4.00

Let's turn now our attention to graphical results depicted in Figures 4.7-4.9. Similar to the presentation of ICA results in Figures 4.2-4.4, Figures 4.7 and 4.8 display the best-fitting centroidal waveforms on a subject-by-subject basis and on a quadruple-by-quadruple basis. One can observe that on some centroidal waveforms, there exists a second rise, resulting in a two-bump appearance. This wave shape cannot be easily modeled by the single bump Gamma function, which explains the low correlations in Tables 4.12 and 4.14. It's disputable whether these waveforms are indeed related to any cognitive activity.

In summary, for (H1)-type datasets, one can state that Subject 4 (alias: KP001) and mid-left quadruple prove to be the most responsive among subjects and among quadruples, respectively. This fact can also be verified from Figures 4.9 (a) and (b) where (H2)-type dataset and (H3)-type dataset results are displayed.

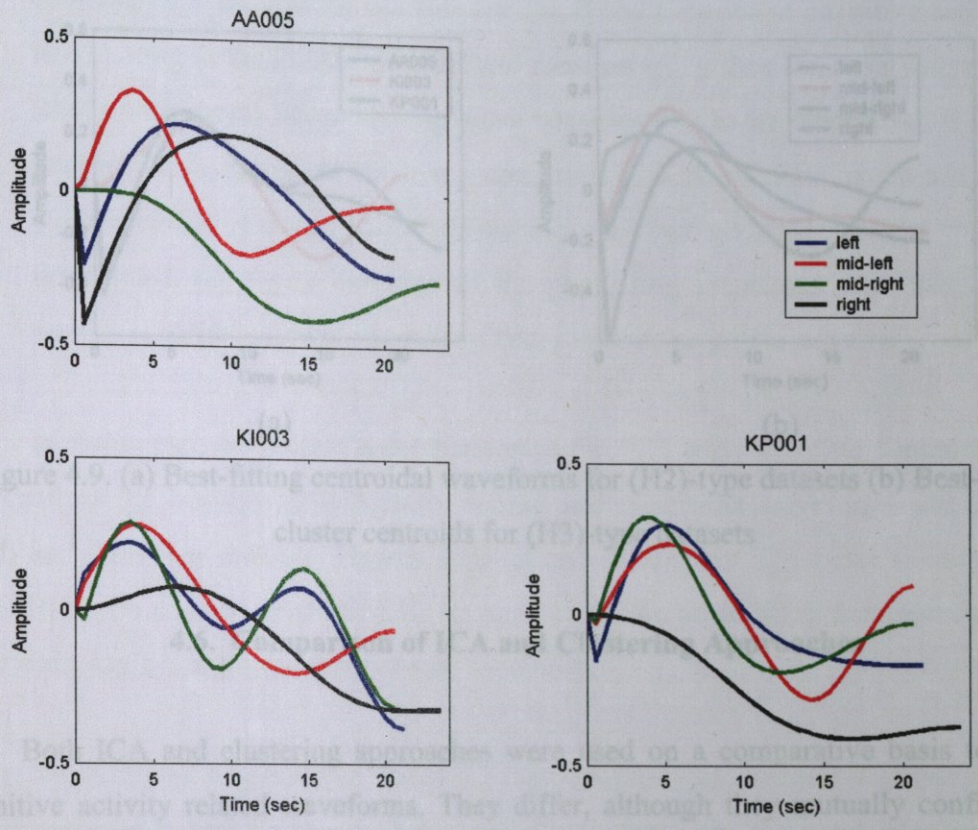

Figure 4.7. Best-fitting centroidal waveforms for (H1)-type datasets, subject-by-subject

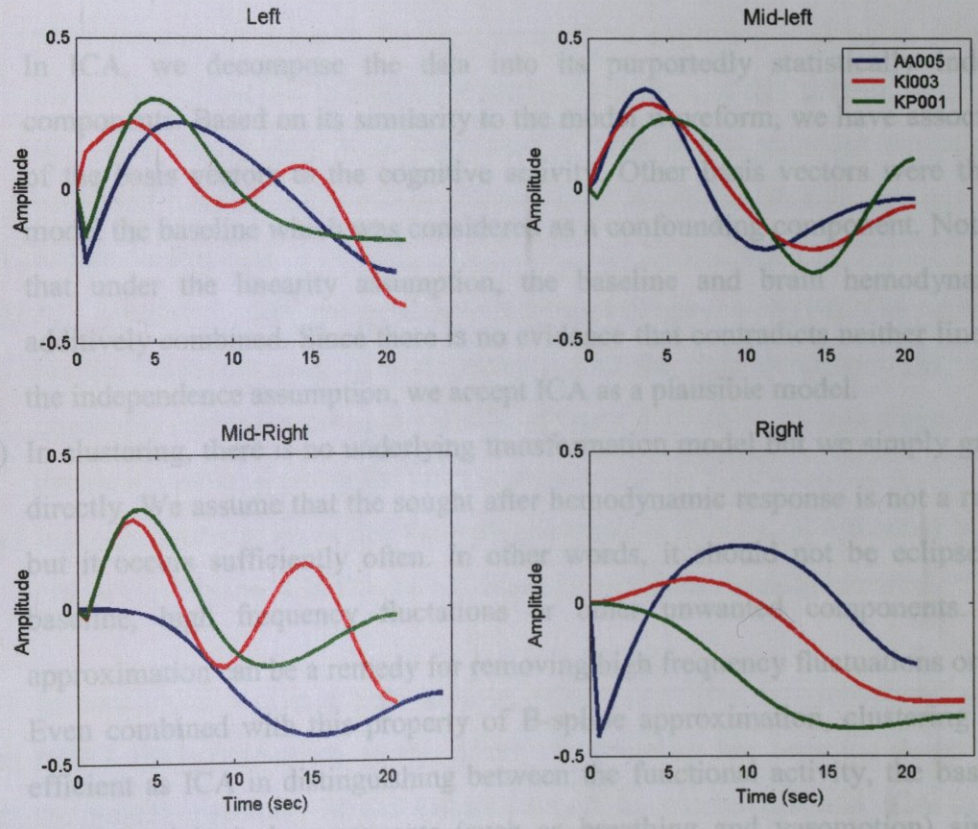

Figure 4.8. Best-fitting centroidal waveforms for (H1)-type datasets, quadruple-by-quadruple

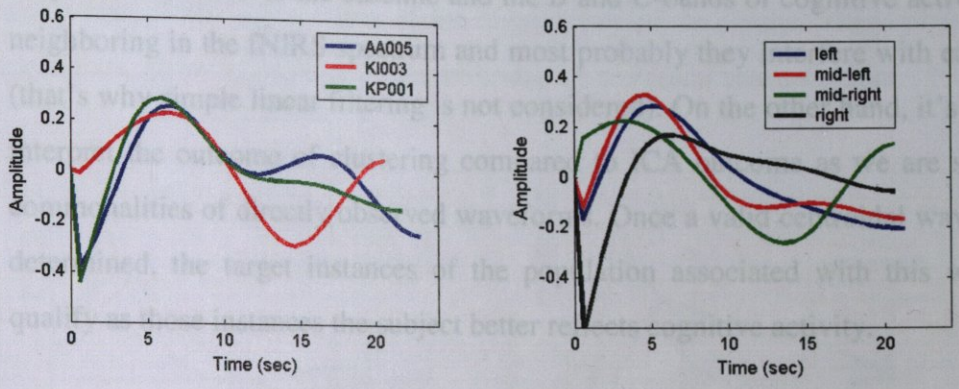

(a) (b)

Figure 4.9. (a) Best-fitting centroidal waveforms for (H2)-type datasets (b) Best-fitting cluster centroids for (H3)-type datasets

4.6. Comparison of ICA and Clustering Approaches

Both ICA and clustering approaches were used on a comparative basis to extract cognitive activity related waveforms. They differ, although they mutually confirm each other, in the following aspects

(i) In ICA, we decompose the data into its purportedly statistically independent components. Based on its similarity to the model waveform, we have associated one of the basis vectors to the cognitive activity. Other basis vectors were thought to model the baseline which was considered as a confounding component. Notice again that under the linearity assumption, the baseline and brain hemodynamics are additively combined. Since there is no evidence that contradicts neither linearity nor the independence assumption, we accept ICA as a plausible model.

(ii) In clustering, there is no underlying transformation model but we simply group data directly. We assume that the sought after hemodynamic response is not a rare event, but it occurs sufficiently often. In other words, it should not be eclipsed by the baseline, high frequency fluctations or other unwanted components. B-spline approximation can be a remedy for removing high frequency fluctuations or artifacts. Even combined with this property of B-spline approximation, clustering is not as efficient as ICA in distinguishing between the functional activity, the baseline and other physiological components (such as breathing and vasomotion) since those components have very close spectral ranges of dominance. Recall that the

conjectured *A*-band of the baseline and the *B* and *C*-bands of cognitive activity were neighboring in the fNIRS spectrum and most probably they interfere with each other (that's why simple linear filtering is not considered). On the other hand, it's easier to interpret the outcome of clustering compared to ICA outcome as we are searching commonalities of directly observed waveforms. Once a valid centroidal waveform is determined, the target instances of the population associated with this waveform qualify as those instances the subject better reflects cognitive activity.

In the sequel, we present a comparison of the ICA and clustering approaches. Let's concentrate the best-fitting ICA basis vectors and centroidal waveforms obtained from (H2) and (H3)-type datasets. Figures 4.10 (a) and (b) display ICA basis vectors for (H2) and (H3)-type datasets, Figures 4.10 (c) and (d) do the same thing for estimated cluster centroids. Let's itemize the observations for clarity.

(i) Similarity of responses of Subject 3 (alias: KI003) and Subject 4 (alias: KP001) is observed in both ICA basis vectors and cluster centroids (Figures 4.10 (a) and (c)).

(ii) While the response of Subject 1 (alias: AA005), as estimated by ICA, has a small time-constant, in contrast, the one estimated by clustering is sluggish (Figures 4.10 (a) and (c)). Note that individual quadruple responses of this subject, as estimated by ICA (see Figure 4.2), were very similar (with a low standard deviation of the estimated time-constants of the Gamma fits), hence we should rely more on ICA results for this case.

(iii) ICA yielded all different quadruple responses (Figure 4.10 (b)). On the other hand for the clustering case, with the exception of the right quadruple, the other three quadruple responses are quite similar (Figure 4.10 (b)). At this stage, we cannot decide in favour of one or the other approach.

(iv) It is comforting to know that the right quadruple responses, as estimated by ICA and clustering (Figures 4.10 (b) and (d), black curves), are virtually identical.

In conclusion, we have been able to extract cognitive activity-related waveforms from fNIRS-HbO_2 time-series. In this effort, the guideline has been the degree of match with the model waveform of the Gamma function. We have found ICA to be more

satisfactory than clustering in terms of the consistency of its results. These observations and conclusions, however, need to be corroborated by a clinical neuroscientist.

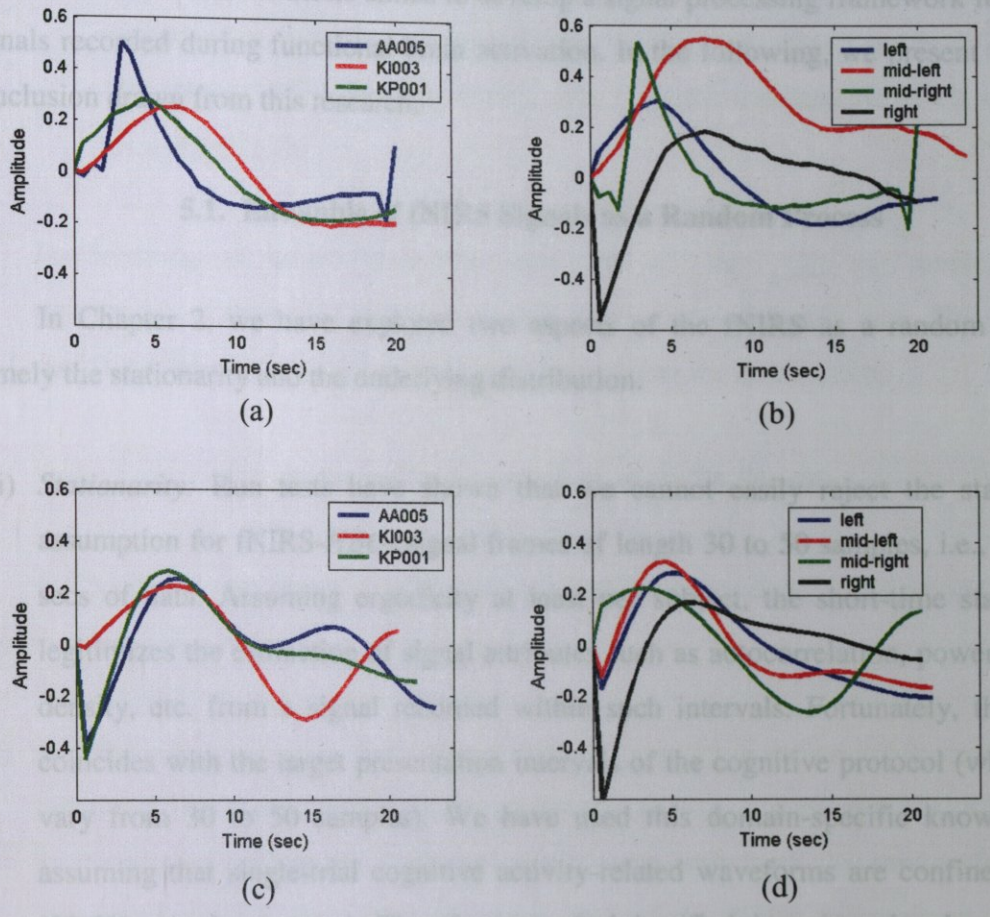

Figure 4.10. (a) Best-fitting ICA basis vectors for (H2)-type datasets, (b) Best-fitting ICA basis vectors for (H3)-type datasets, (c) Best-fitting centroidal waveforms for (H2)-type datasets and (d) Best-fitting centroidal waveforms for (H3)-type datasets

5. CONCLUSIONS

Let's recall that the thesis aimed to develop a signal processing framework for fNIRS signals recorded during functional brain activation. In the following, we present the main conclusion drawn from this research.

5.1. Ensemble of fNIRS Signals as a Random Process

In Chapter 2, we have explored two aspects of the fNIRS as a random process, namely the stationarity and the underlying distribution.

(i) *Stationarity:* Run tests have shown that we cannot easily reject the stationarity assumption for fNIRS-HBO_2 signal frames of length 30 to 50 samples, i.e., 18 to 29 secs of data. Assuming ergodicity at least per subject, the short-time stationarity legitimizes the estimation of signal attributes such as autocorrelation, power spectral density, etc. from a signal recorded within such intervals. Fortunately, this range coincides with the target presentation intervals of the cognitive protocol (which also vary from 30 to 50 samples). We have used this domain-specific knowledge in assuming that single-trial cognitive activity-related waveforms are confined within (30,50) samples interval. Therefore, we feel justified in using signal processing techniques under the assumption of stationarity. On the other hand, the long-term non-stationarity of fNIRS signals is mostly due to the baseline which is responsible of the trend. It's known that even in resting state, the hemoglobin and oxyhemoglobin concentrations in the brain change over time [45]. During task-related cognitive activity, the subject's hemodynamic responses are superimposed on the baseline, which in ensemble result in a non-stationary process.

(ii) *Gaussianity:* We performed three different Gaussianity tests on fNIRS-HbO_2 signals. The conclusion of all these, namely Kolmogorov-Smirnov test, Jarque-Bera test and Hinich test, was common so that HbO_2 signals are non-Gaussian. The implication is two-fold.

- The linear minimum mean-squared error (MSE) estimators will not be globally optimal, in extracting cognitive activity-related waveforms.
- The use of ICA in chapter 4 is plausible. ICA can be achieved under the assumption that all, but except one, sources which linearly combine to yield the observations, are non-Gaussian. Since the observed signals are non-Gaussian, the sources cannot be "more" Gaussian than the observations by Central limit theorem (CLT).

Furthermore, as skewness and kurtosis analyses have put into evidence, the distribution of detrended HbO_2 samples is symmetric with heavy tails. This suggests that Gaussian mixtures are not suitable for modeling the distribution.

5.2. Relevant Spectral Bands of fNIRS Signals

In Chapter 3, we investigated canonical bands that purportedly corresponded to the cognitive activity.

(i) *The short-time spectrum* revealed that fNIRS signals have their main spectral content below 0.1 Hz. Furthermore, we have observed a peaking at around 0.7-0.85 Hz range as the aliased part of the heartbeat signal, compatibly with the cardiac frequency range, i.e, 0.6-1.2 Hz [45]. Otherwise, the whole fNIRS spectrogram was too promiscous in localizing temporal events such as the responses to cognitive task stimuli.

(ii) *Canonical bands:* We have developed a method to parse the signal spectrum into canonical subbands that, we think, can faithfully be associated to different physiological components, such as the baseline, the task-related activity or others such as the breathing effect and the cardiac pulsations. The subbanding scheme uses dissimilarity between relative power profiles per band of the signal. We note that the proposed subband partitioning methodology is general and can be utilized for a similar analysis of any set of signals. For fNIRS signals recorded during functional brain activation, we found the following.

- *A*-band: 0-30 mHz. We conjecture that this band corresponds to the baseline signal, or at least some part of it, which is independent of task-related cognitive activity.
- *B*-band: 30-40 mHz. The centered Gamma function, which is a commonly used brain hemodynamic response model in fMRI, has its spectral peak in this frequency interval. We believe that the fundamental frequency of task-related events in fNIRS lies in the *B*-band.
- *C*-band: 40-250 mHz. The relatively larger *C*-band is also assumed to carry task-related information due to the periodicity of target stimuli induced by cognitive protocol. Moreover, it overlaps with the respiratory-frequency range (100-500 mHz) [45] and is hypothesized to include vasomotion.
- *D*-band: 250-850 mHz. This band contains a very small proportion of the total signal power and is definitely uncorrelated with cognitive activity. Notice that since the upper limit is set by the Nyquist sampling theorem, it only contains the aliased part of the heartbeat signal.

Notice that fMRI experiments carried over subjects at the resting state, have shown that the baseline activity is observed up to 100 mHz [45]. Thus, at least in fMRI, the baseline extends over our *A*-band, *B*-band and lower one third of the *C*-band. Accordingly, interference from the baseline, although less pronounced, should coexist with other components cited above at the *B* and *C*-bands.

(iii) *Evidence of cognitive activity:* We have validated our conjecture on the protocol-induced periodicity. Some of the fNIRS-HbO_2 signals exhibit the target quasi-periodicity. The observability of such periodicity was instrumented in classifying photodetectors/subjects as responsive and non-responsive to cognitive stimuli. The algorithm we have used was the least-square periodicity estimation method which implicitly assumes the stationarity of the signal being analyzed. Notice that the (30,50) samples stationarity range established by the run tests couldn't carry such a periodicity information, since the sought-after periods were in that range. In order to mitigate the problems associated to non-stationarity, we have first prefiltered the signals in the *BC*-band, as a common practice in statistical signal processing since many signals may look stationary after trend removal [22]. Stationarity was not actually the major concern in prefiltering but a useful side-benefit. Based on our

conjectures on the canonical bands, prefiltering had the effect of removing the baseline component significantly and putting the protocol-induced periodicity into evidence. A second precaution concerning stationarity was using signal sessions that include 8 targets at most. Since target exposition patterns were identical for such sessions (there are 8 of them per experiment), we have been able to collect enough evidence to decide for the responsiveness or non-responsiveness of a signal from a specific photodetector/subject pair. In conclusion, we have observed that the mean periodicity estimated from qualified pairs matches the mean inter-target interval length of 40 samples.

5.3. Cognitive Activity-Related Waveform Extraction

With the goal of identifying the brain hemodynamic response waveform to a single cognitive stimulus, we explored two non-parametric methods: ICA and clustering. Both of these methods are exploratory. The outcomes of the non-parametric schemes were benchmarked against the model waveform, that is the parametric fit to the Gamma waveform was tested. Based on the results, we concluded the following.

(i) Inter-subject and inter-quadruple-of-detectors variations exist.

(ii) In terms of the conformance to Gamma function model, waveforms estimated by ICA are more plausible to be cognitive-activity related than those estimated by clustering.

(iii) ICA decomposition yields not only the cognitive activity-related waveform, but also others that can potentially be used to model the baseline interference.

(iv) The brain hemodynamic response can be more flexibly parametrized as compared to Gamma model which relegates all the characteristics to a single parameter. Instead, B-spline coefficients represent the global waveform while preserving locality property.

(v) A final interesting alternative could be the ICA of B-spline coefficients for cognitive activity-related waveform extraction.

5.4. Future Prospects

Several future research topics can be proposed, as presented in the sequel.

5.4.1 Process Characterization

We emphasize the following issues.

(i) *Distribution of fNIRS data:* As established in Chapter 2 and pointed out in Section 5.1 as well, fNIRS signals do not arise from a Gaussian process. Furthermore, the unimodality of the samples precludes Gaussian mixture modeling. A future work may concentrate on the density estimation of HbO_2 signal samples either in a non-parametric way (e.g. by a kernel or K-nearest neighbor estimator) [38] or using a parametric heavy-tailed distribution model [37]. Such a study would not only complete the statistical characterization of fNIRS signals but it would also provide preliminaries for Bayesian estimation of the cognitive activity-related waveforms.

(ii) *Alternative time-frequency features:* In Chapter 3, we have prefered the relative power profile per band as an objective measure of the time-frequency representation. Blanco et al. suggested other objective measures such as the series of the *mean weight frequency*, the *main peak frequency* and the *monofrequency deviation* in the analysis of EEG signals [28]. An exploration of the variations of these quantities over time, at the canonical bands we determined, may be pursued in order to maximize the benefits of the time-frequency analysis.

(iii) *Alternative subband partitioning scheme:* The motivation behind wavelet packet analysis of EEG signals [46] is very similar to the one behind our subbanding methodology. The wavelet packet analysis may be implemented for fNIRS signals to see whether the results of both methods mutually confirm each other.

5.4.2. Alternative Methods for Functional Activity Estimation

The following issues can be addressed for the extraction of the cognitive activity related waveforms.

(i) *Fuzzy clustering of B-spline coefficients* can potentially improve waveform classification [38]. In real applications there is often no sharp boundaries between clusters. Hence one risks of artificially assigning data into some clusters in crisp clustering. In contrast to the latter, the assignments in fuzzy clustering are accompanied with membership degrees that vary from zero to one. Such an approach may be useful in classifying the responses of a subject in a more flexible way and in associating a confidence to the estimated cognitive activity-related waveform.

(ii) *The self-organizing map* (SOM) can be another clustering-based approach [47]. A SOM is a 1D or 2D array of vectors that are equivalent to cluster centroids. In the SOM, the centroids are configured in such a way that neighboring centroids on the grid are similar to each other whereas the farther away ones are dissimilar. This property of the SOM may be exploited in order to observe cognitive activity variations. The dot-product SOM algorithm, in particular, should be considered in the first place since it relies on a correlation metric, like in our agglomerative scheme, to evaluate correspondences.

(iii) *Bayesian modeling:*One of the most up-to-date approaches in the non-parametric estimation of the brain hemodynamic response (BHR) function in fMRI is due to Ciuciu et al. [9]. A reduced form of the generative data model, suitable for single-trial events, can be described as

$$\mathbf{y}_k = \mathbf{h} + \mathbf{C}\mathbf{d}_k + \mathbf{v}_k \tag{5.1}$$

$\mathbf{y}_k = \left[y_{t_k}, y_{t_k+1}, \cdots, y_{t_k+m-1}\right]^T$: the observed BOLD sequence (vector) of length m in response to the k^{th} target stimulus at instance t_k.

$\mathbf{h} = \left[h_0, h_1, \cdots, h_{m-1}\right]^T$ is the unknowm BHR vector of length m.

$\mathbf{C}=\left[\mathbf{c}_1,\cdots,\mathbf{c}_Q\right]$ is a set of orthonormal basis functions $\mathbf{c}_q=[c_0,\cdots,c_m]^T$ that can model the low-frequency components, i.e., the baseline.

$\mathbf{d}_k=[d_{1,k},d_{2,k},\cdots,d_{Q,k}]^T$: vector of unknown weighting coefficients of the basis functions at the arrival of the k^{th} target stimulus.

$\mathbf{v}_k=[v_{t_k},v_{t_k+1},\cdots,v_{t_k+m-1}]^T$: the term that stands for unwanted random physiological fluctuations and measurement noise after the arrival of the k^{th} target stimulus.

They treated the model (5.1), and its general form which is suitable for multitask cognitive protocols, in a Bayesian formalism and estimated BHR functions, that are validated for both real and synthetic data, using expectation conditional maximization (ECM) algorithm [48]. The very same approach can be adopted in fNIRS for the extraction of cognitive activity-related waveforms by modeling prior information on the brain hemodynamics and the baseline measured by fNIRS, in order .

(iv) *Dynamic Bayesian modeling:* The model (5.1) is time-invariant in that it imposes a fixed vector **h** for every trial of the cognitive stimulus, as the methods of Chapter 4 in this report implicitly assumed. On the other hand, (5.1) can be extended to a dynamical model using a state-space approach as described below.

$$\begin{aligned}\mathbf{h}_{k+1}&=\boldsymbol{\Gamma}(k+1,k)\mathbf{h}_k+\mathbf{w}_k\\ \mathbf{y}_k&=\mathbf{h}_k+\mathbf{C}\mathbf{d}_k+\mathbf{v}_k\end{aligned}\tag{5.2}$$

where $\boldsymbol{\Gamma}(k+1,k)$ is the state-transition matrix that should cope with the dependencies between successive responses and $\mathbf{w}_k$ is a disturbance vector. From this viewpoint, the estimation of the cognitive activity-related waveforms (or the BHR) based on (5.2) constitute a further research topic that should consider the extended Kalman Filtering concepts [49], such as Markov chain Monte Carlo methods or particle filtering [50], in the fNIRS setting.

(v) *Non-linear neurovascular coupling:* A majority of the BHR estimation schemes in fMRI commonly assume linearity between neuronal activity and BOLD response. However, the true underlying mechanism, i.e., the neurovascular coupling, is not completely understood and characterized [9]. Linearity is often retained for its simplicity. In the fMRI literature, there exists a couple of attempts in non-linear modeling of neurovascular coupling through support vector machines [51], [52]. Based on these ideas, (5.1), or equivalently the second equation in (5.2), extend to

$$\mathbf{y}_k = f(\mathbf{X})\mathbf{h} + \mathbf{C}\mathbf{d}_k + \mathbf{v}_k \tag{5.3}$$

where $\mathbf{X}$ stands for the binary stimuli matrix as a mean of expressing neuronal activity in mathematical formalism and $f(\cdot)$ is a non-linear function of $\mathbf{X}$. Notice that in (5.3), the model is still linear in $\mathbf{h}$, but $\mathbf{X}$ undergoes a non-linear transformation. Multilayer perceptrons, which can learn any non-linear function in theory [38], can be constructed in conjunction with the ideas proposed in items (iii) and (iv) above as a further prospect in fNIRS.

5.5. Remarks on the Experimental Protocols and Measurements

In this final section, we would like to discuss two important aspects of cognitive experiments in the context of fNIRS.

(i) *Simultaneous fMRI-fNIRS measurements*: There is a necessity to simultaneously acquire fMRI and fNIRS data during functional brain activity. For the time being, cognitive activity-related waveform extraction in fNIRS, due to its low spatial resolution, cannot find its true running track unless it is accompanied with simultaneous fMRI data. To clarify, using fNIRS one cannot obtain fine detail brain activity maps, although the brain hemodynamic response can be more accurately estimated by fNIRS thanks to its higher temporal detail. Research in optimizing spatial photosensor-array geometry is a relatively new field in diffuse optical methods [2] and localization of externally recorded signals in fNIRS is still very difficult [8]. Another argument in favor of simultaneous use of fNIRS and fMRI is the lacking of reliable quantification schemes for *Hb* and HbO_2 concentrations, as

reported in [8]. Once such recordings from both modality are acquired simultaneously, the fNIRS waveforms can be utilized for generating more reliable fMRI activation maps.

(ii) *Design of experimental protocols*: In stimulus design of even-related fMRI experiments, two dichotomies exist: randomized vs. block designs. The former consists of impulsive train of target stimuli with random arrivals and it can possibly be interleaved with a series of more frequent context stimuli. The cognitive protocol of the present work is an example to randomized designs. On the other hand, in block designs, the stimuli sequence can be described as a series of rectangular waves. In a recent study [53], it has been argued that "randomized designs offer maximum estimation efficiency but poor detection power, while block designs offer good detection power at the cost of minimum estimation efficiency.". Since activation detection in fNIRS cannot be an issue unless devices that can provide more spatial detail are implemented, randomized event-related designs should be considered in the first place for maximum estimation efficiency in fNIRS experiments.

APPENDIX A: STATISTICAL TOOLS

We made use of [22-27, 38] in preparing the material presented in this part.

A.1. Hypothesis Testing

Statistical hypothesis testing provides a formal way to decide if the results of an experiment are significant or accidental. Consider a record of samples that consist of n measurements (samples). Suppose futher that we want to determine whether these measurements come from a known distribution f_0 (whose parameters are fully specified) or not. Initially, we hypothesize that f_0 is indeed the underlying distribution of the samples; this is called the *null hypothesis* and denoted as H_0. The *alternative hypothesis*, i.e., that the samples are not drawn from f_0, is denoted as H_1. We now state the problem as deciding whether to *accept* or *reject* H_0.

At this point, we assume that we will accept H_0, if a *test-statistic* ξ, computed from the available n samples, is below some *critical value* γ; otherwise we will accept H_1. That is

$$\begin{aligned} &\text{If } \xi > \gamma, \quad \text{accept } H_1 : \text{samples are not drawn from } f_0. \\ &\text{If } \xi < \gamma, \quad \text{accept } H_0 : \text{samples are drawn from } f_0. \end{aligned} \tag{A.1}$$

We can make two kinds of error

- *False Alarm* (Type I error): Reject H_0 (accept H_1) when H_0 is true.
- *False Miss* (Type II error): Reject H_1 (accept H_0) when H_1 is true.

The probability of false alarm *PFA* is expressed as

$$PFA = \Pr\{\xi \geq \gamma | H_0\} \tag{A.2}$$

The hypothesis test can equivalently be performed by the following statements

$$\begin{aligned} &\text{If } PFA < \alpha, \quad \text{accept } H_1 : \text{samples are not drawn from } f_0. \\ &\text{If } PFA > \alpha, \quad \text{accept } H_0 \text{ (it is risky to accept } H_1\text{)} : \text{samples are drawn from } f_0. \end{aligned} \tag{A.3}$$

where α is said to be the *significance level* of the test. As the context implies, there is a one-to-one correspondence between the significance level α and the critical value γ. In order to compute (A.2), we must know the distribution of the test-statistic ξ or simply its percentage points (critical values at corresponding significance levels). Usually, we set the significance level to 0.05 or 0.01 and use a statistical table to find out the corresponding critical value. Afterwards we compare the test-statistic against the critical value and decide whether to accept of reject H_0 as descibed above. If we require the explicit knowledge of the *PFA*, we can read it from the graph of the cumulative distribution function (cdf) of the test-statistic. Suppose we read p_ξ at ξ from the graph of its cdf for some test: if the test is *significant in the upper tail PFA*=1- p_ξ, or otherwise, if it is *significant in the lower tail PFA*= p_ξ.

The use of hypothesis testing is certainly not limited to test whether the measurements are drawn from a known distribution or not. Some of hypothesis testing examples are: (i) There is no signal in the present interval, (ii) The short-time signal is stationary, (iii) There is neuronal activation in a particular brain region at a particular time, (iv) Smoking does not kill, (v) Team A will defeat Team B in the next match, etc.

A.2. Run Test for Stationarity

Run test can detect a monotonic trend in a time series $x(t)$, t=1,..., $2N$, by evaluating the number of runs in a time-series derived from $x(t)$. A "run" is defined as a sequence of identical observations that is followed or preceded by a different observation or no observation at all. To this effect, we first evaluate the median m_x of the observations and derive the series $y(t)$ as

$$\begin{aligned} y(t) &= 0 \quad \text{if } x(t) < m_x \\ y(t) &= 1 \quad \text{if } x(t) \geq m_x \end{aligned} \tag{A.4}$$

Then we compute the number of runs in $y(t)$, that is the number of consecutive observations where the signal exceeds the median level and similarly the number of consecutive observations where the signal remains below the median level. If $x(t)$ is a stationary random process, the number of runs R is a random variable with

$$\mu_R = N+1$$
$$\sigma_R^2 = \frac{N(N-1)}{2N-1} \tag{A.5}$$

where μ_R and σ_R^2 denote the mean and variance of R, respectively. An observed number of runs significantly different from N+1 is indicative of non-stationarity because of the possible presence of a trend in $x(t)$. Using the run distribution with parameter N, that is

$$P(R=n) = \begin{cases} 2\dfrac{\binom{N-1}{n/2-1}^2}{\binom{2N}{N}}, & n = 2,4,\ldots,2N \\ 2\dfrac{\binom{N-1}{n/2-1/2}\binom{N-1}{n/2-3/2}}{\binom{2N}{N}}, & n = 3,5,\ldots,2N-1 \end{cases} \tag{A.6}$$

we determine whether the signal $x(t)$ is stationary or not by hypothesis testing.

A.3. Gaussianity Tests

A.3.1. Kolmogorov-Smirnov Test

The Kolmogorov-Smirnov test (*K-S* test) is a general purpose test based on comparing the empirical cumulative distribution function (ecdf) of the available samples with the theoretical cdf of the distribution that the test is carried for. It is defined as

$$\begin{aligned} H_0 &: \text{Random variable } X \text{ follows the specified distribution } F(x). \\ H_1 &: \text{Random variable } X \text{ does not follow the specified distribution } F(x). \end{aligned} \tag{A.7}$$

The *K-S* test-statistic ξ_{ks} is defined as

$$\xi_{ks} = \max_{t}^{N} \left| F(x_t) - F_e(x_t) \right| \tag{A.8}$$

where $F_e(x_t)$ is the ecdf of observations x_t, $t = 1,..., N$. The *KS*-test can be utilized for testing observations for Gaussianity (normality). Since $F(x)$ should be completely specified, we first make the observations zero-mean, unit-variance and then we compute $F_e(x)$. We evaluate (A.8) using the standard normal cdf in place of $F(x)$ and the ecdf $F_e(x)$. Once ξ_{ks} is obtained, the rules of hypothesis testing can be applied to decide for normality using tabulated critical values of the *K-S* test-statistic distribution. Note that this test requires independent identically distributed (i.i.d.) data.

A.3.2. Jarque-Bera Test

The Jarque-Bera (*J-B*) test is a normality test that uses third and fourth order central moments based on the fact these vanish for normal random variables. The *J-B* test-statistic ξ_{jb} is a function of the sample estimates of the skewness and of the kurtosis denoted by $\hat{\tau}$ and $\hat{\kappa}$, respectively.

$$\xi_{jb} = \frac{N}{6}\left(\hat{\tau}^2 + \frac{\hat{\kappa}^2}{4} \right) \tag{A.9}$$

$$\hat{\tau} = \frac{1}{N\hat{\sigma}^3}\sum_{t=1}^{N}(x_t - \hat{\mu})^3 \tag{A.10}$$

$$\hat{\kappa} = \frac{1}{N\hat{\sigma}^4}\sum_{t=1}^{N}(x_t - \hat{\mu})^4 - 3 \tag{A.11}$$

where $\hat{\mu}$ and $\hat{\sigma}^2$ are the sample estimates of the mean and the variance of the observations x_t, $t = 1,..., N$. The limiting distribution, for i.i.d data, of the *J-B* test-statistic ξ_{jb} is χ_2^2, i.e., Chi-square with two degrees of freedom. Again it is a simple matter to calculate (A.9)-(A.11) and apply hypothesis testing concepts using the fact that $\xi_{jb} \to \chi_2^2$. However, the results are only accurate for sufficiently large N and i.i.d. data since the estimates of higher order moments can be biased for small N and correlated data.

A.3.3. Hinich's Gaussianity Test for Time-series

The above described tests assume i.i.d data and are not suitable for time-series unless one collects data samples at random distant locations. Hinich's bispectrum-based test is purely designed for correlated time-series. In theory, signals that result from Gaussian processes have zero third and higher-order cumulants and this knowledge can be exploited for determining the underlying process of the signal. However in practice, sample estimates of cumulants do not strictly vanish. Thus, one needs a test to determine whether or not estimated quantities are significantly different from zero in the statistical sense. For a linear non-Gaussian process $X(t)$, the following identity holds

$$\frac{S_{xx}(f_1, f_2)}{[S_x(f_1)S_x(f_2)S_x(f_1 + f_2)]^{1/2}} = \text{constant or zero} \tag{A.12}$$

The left-hand side of (A.12) is the bicoherence of the random process $\{X(t)\}$. In particular, the numerator term $S_{xx}(f_1, f_2)$ is the bispectrum and $S_x(f)$ is the power spectral density, f_1 and f_2 being frequency variables. Again, sample estimates of the bicoherence will not be constant, and we need a test to determine whether the non-

constancy is statistically significant. Hinich developed a test which determines whether a given signal is non-Gaussian as

$$\begin{aligned} H_0 &: X(t) \text{ has zero bispectrum, i.e., the process is Gaussian.} \\ H_1 &: X(t) \text{ has non - zero bispectrum, i.e., the process is not Gaussian.} \end{aligned} \tag{A.13}$$

Accordingly the test is based on whether the ratio in (A.12) differs significantly from zero or not. Hinich's test statistic ξ_{hin} is the sum of the squared bicoherence values over the principal domain of the bispectrum, and is Chi-square distributed. The test can be performed either by using ξ_{hin} and (A.1) or the computed probability of false alarm p_{hin} and (A.3) at the desired significance level α.

A.4. Fisher's Method for Combining Independent Tests

Fisher's method can be used for combining independent tests for several records based on computed false alarm probabilities, also called p-values, of individual tests. Suppose K tests are made of null hypotheses $H_0^i, i = 1,..., K$ each of which states the ecdf of the samples of the i^{th} record, $x_t^i, t = 1,..., N$, is greater than the standard normal cdf. Let H_0 be the composite hypothesis that all H_0^i are true, that is, if anyone is false then we must reject H_0. Suppose further that each test returned p_i as its significance level, i.e., the probability of rejecting H_0^i when it is indeed true. Furthermore, when H_0^i is true, p_i is a uniform random variable in the interval (0, 1). Hence we obtain a record of K samples with uniform distributions if all H_0^i together, or equivalently the composite hypothesis H_0, holds. In such a situation, any deviation from uniformity would be sufficient for rejecting the composite hypothesis H_0, i.e., the normality of all records. For instance, the Kolmogorov-Smirnov test can be used for detecting deviations of p-values from uniformity. On the other hand, Fisher developed a test-statistic, denoted by P_1, that can easily be computed in terms of p-values and be directly used for rejecting or accepting H_0

$$P_1 = -2\sum_{i}^{K} \log(p_i) \tag{A.14}$$

where log(.) stands for the natural logarithm. P_1 combines one-tail component statistics p_i, each of which are the significance levels of the tests, that determine whether the ecdf is *greater* than the standard normal cdf, or not in our working example. P_1 itself is significant at the upper tail of its limiting distribution. In the literature, there exist other versions of statistics of this type, which combines two tail component statistics, each of which tests whether the ecdf is *equal* to the theoretical cdf, or not. One such statistic which is significant at the lower tail of its limiting distribution is defined as

$$P_2 = -2\sum_{i}^{K} \log|1-2p_i| \tag{A.15}$$

The limiting distributions of both P_1 and P_2 are χ^2_{2K}, hence a Chi-square test, with appropriate degrees of freedom, i.e., $2K$, suffices for combining the individual test results.

APPENDIX B: CLUSTERING

In exploratory data analysis as well as in pattern recognition, discovering the underlying distribution of multivariate data in the multidimensional space is of particular importance. A *clustering procedure* is a non-parametric method that gives dominant modes of the multivariate data in terms of clusters or groups of data points that possess strong internal similarities. In formal terms, clustering partitions a multivariate dataset $X=\{\mathbf{x}^t \mid t=1,...,N\}$ into a set of clusters $Q=\{Q_c, \mathbf{q}_c \mid c=1,...,C\}$ where $\mathbf{q}_c$ is the centroid of the cluster Q_c. To this effect, often a criterion or a set of criteria is to be satisfied for a set of clusters Q. Two major issues are of concern in clustering

(i) The way we measure similarity between data samples,
(ii) The aspects of the clusters that lead to a natural grouping of the data.

Note that we made use of [38, 41] in preparing the material presented in this appendix.

B.1. Similarity Measures

Similarity measures addresses the item-(i) above. The most natural way to measure similarity between two samples is to evaluate the distance between them. A suitable distance metric satisfies

- **Non-negativity:** $d(\mathbf{x},\mathbf{y}) \geq 0$
- **Reflexivity:** $d(\mathbf{x},\mathbf{y}) \geq 0 \Leftrightarrow \mathbf{x}=\mathbf{y}$
- **Symmetry:** $d(\mathbf{x},\mathbf{y}) = d(\mathbf{y},\mathbf{x})$
- **Triangle Equality:** $d(\mathbf{x},\mathbf{y}) + d(\mathbf{y},\mathbf{z}) \leq d(\mathbf{x},\mathbf{z})$

Note that it is possible to transfom a similarity measure into a distance metric so that it gains the above cited properties. Some of the distance metrics and similarity measures that are widely used in clustering are in the sequel.

- **Minkowski metric** $d(\mathbf{x},\mathbf{y})=\left(\sum_{k=1}^{m}|x_k-y_k|^c\right)^{1/c}$, where $c\geq 1$ is the selective parameter. The Minkowski metric is equivalently called as L_c-metric. Notice that for $c = 2$, the Minkowski metric evalautes to the familiar Euclidean distance. For $c = 1$, it can be recognized as *Manhattan* or *city block* distance that accounts for the sum of the absolute distances along each of the m coordinate axes. In some cases, the distances along a single axis is much more important than in all of the remainder. $L_\infty=\max_{k=1}^{m}|x_k-y_k|$ is evaluated in such situations.

- **Mahalanobis distance** $d(\mathbf{x},\mathbf{y})=(\mathbf{x}-\mathbf{m})^T\boldsymbol{\Sigma}^{-1}(\mathbf{y}-\mathbf{m})$ involves data-dependent terms as the mean vector $\mathbf{m}$ and the covariance matrix $\boldsymbol{\Sigma}$ of the observations $\{\mathbf{x}^t \mid t=1,...,N\}$ for which $\mathbf{x}$ and $\mathbf{y}$ are two generic instances. The Mahalanobis distance is invariant under dilations, translations and rotations in the m-dimensional space.

- **Cosine of the angle** $s(\mathbf{x},\mathbf{y})=\dfrac{\mathbf{x}^T\mathbf{y}}{\|\mathbf{x}\|\|\mathbf{y}\|}$, where $\|\cdot\|$ stands for the Euclidean distance. In case the cosine of the angle is a meaningful measure of similarity, we can use $d(\mathbf{x},\mathbf{y})=1-s(\mathbf{x},\mathbf{y})$ as a distance metric for clustering, $d(\mathbf{x},\mathbf{y})$ can be called as *one-minus-the-cosine-of-the-angle*. In some situations, it would be more appropriate to treat the observations as sequences of values (e.g., when the components of the vectors are consecutive samples of a short-time signal), rather than as vectors, by subtracting the mean value of their components from each of the vectors, i.e., for $\mathbf{x}$, $x_{k,new}=x_k-\dfrac{1}{m}\sum_{i=1}^{m}x_i$ for $k = 1,..., m$ and similarly for $\mathbf{y}$, before computing $s(\mathbf{x},\mathbf{y})$. The resulting similarity measure is called as the normalized correlation coefficient, and the distance metric derived from it as *one-minus-the-normalized-correlation-coefficient* in a way compatible with the signal processing literature.

B.2. Clustering Criteria

The choice of the distance metric is one of the issues in clustering, the aspects of data that we exploit for grouping constitute another. An optimal clustering is generally defined as the one that *minimizes within-cluster* and *maximizes between-clusters* distances. However, such distances need to be defined to get several different criterion functions. In Table B.1, many possibilities are displayed.

Table B.1. Several definitions
for within-clusters distance $S(Q_c)$ and between-cluster distance $d(Q_c, Q_l)$

Within-cluster distance	$S(Q_c)$
average distance	$S_a = \frac{1}{N_c(N_c-1)} \sum_{i,i'} \left\| \mathbf{x}^i - \mathbf{x}^{i'} \right\|$
nearest neighbor distance	$S_{nn} = \frac{1}{N_c} \sum_{i} \min_{i'} \left\| \mathbf{x}^i - \mathbf{x}^{i'} \right\|$
centroid distance	$S_c = \frac{1}{N_c} \sum_{i} \left\| \mathbf{x}^i - \mathbf{q}_c \right\|$
Between-cluster distance	$d(Q_c, Q_l)$
single linkage	$d_s = \min_{i,j} = \left\| \mathbf{x}^i - \mathbf{x}^j \right\|$
complete linkage	$d_s = \max_{i,j} = \left\| \mathbf{x}^i - \mathbf{x}^j \right\|$
average linkage	$d_a = \frac{1}{N_c N_l} \sum_{i,j} \left\| \mathbf{x}^i - \mathbf{x}^j \right\|$
centroid linkage	$d_{ce} = \left\| \mathbf{q}_c - \mathbf{q}_l \right\|$

Q_c and Q_l: two clusters with centroids $\mathbf{q}^c$ and $\mathbf{q}^l$, $c \neq l$, respectively

$\mathbf{x}^i, \mathbf{x}^{i'} \in Q_c, i \neq i'; \mathbf{x}^j, \mathbf{x}^{j'} \in Q_l, j \neq j'$

N_c and N_l: the number of samples in clusters Q_c and Q_l, respectively

The distance norm $\|\cdot\|$ can be chosen as one of the metrics presented in B.1 or others that are not given here, according to the specific application. Notice that the combination of within-cluster distance, between-clusters distance and the distance metric to form a criterion function should be carried with caution since an inappropriate combination can cause misinterpretation of the data. In summary, a criterion J is implicitly expressed as

$$J = f[S(Q_c), d(Q_c, Q_l), C] \tag{B.1}$$

where $c, l = 1,...,C$ with $c \neq l$ and C is the total number of clusters. The parameter C appears in (A.1) in order to optimize J with minimum possible number of clusters.

B.3. Clustering Algorithms

Clustering algorithms are dichotomized in the way they make the partitioning: (i) *partitive* approaches and *hierarchical* approaches. The former divide a dataset into a, usually prescribed, number of clusters C. In a partitive algorithm, initially one should choose a criterion function to optimize, determine the number of clusters C, determine assignment (for data vectors) and update (for centroids) rules as dictated by the chosen criterion. The pseudo-code is as follows.

(1) Initialize the cluster centroids $\mathbf{q}^c$.
(2) Assign each of the data vectors to one of the clusters Q^c using the assignment rules.
(3) Update the cluster centroids $\mathbf{q}^c$ using the update rules.
(4) Stop if the partitioning is unchanged (or the criterion function is optimized); otherwise return to step (3).

Hierarchical clustering algorithms can be further subdivided to *divisive* and *agglomerative* schemes. The latter is more commonly used and can be implemented by the following steps.

(1) Initialize: Assign each vector to its own cluster.
(2) Compute distances between all clusters (according to chosen metric and between-clusters distance).
(3) Merge the two clusters that are closest to ecah other.
(4) Return to step (2) until there is only one cluster left.

By executing the above steps, we obtain an hierarchical tree, or a dendrogram, that holds correspondences between the data vectors. The dendrogram can be utilized in interpreting the underlying structure of the data. Exploiting the dendrogram tree to finalize the clustering procedure, is another issue.

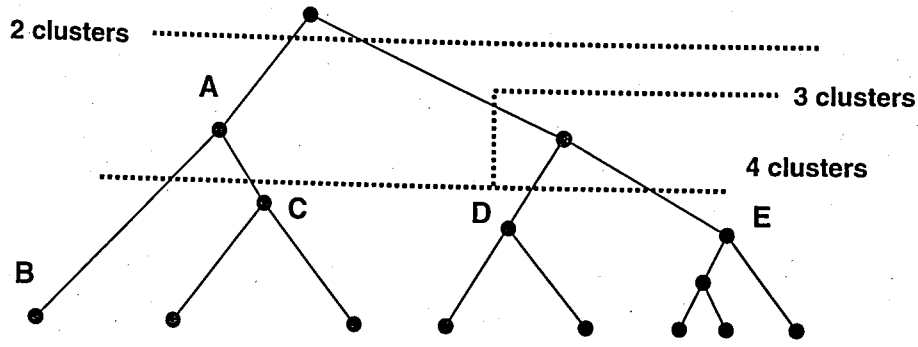

Figure B.1. A sample dendrogram of 8 data points.

In Figure B.1, a sample dendrogram is shown along with three of the plausible cuts. Consider, for instance, the one that results in four clusters. To identify the clusters, we look, on each branch, for the next node below the cut. Accordingly, we get the node **B** as a singleton cluster, the leaves of the node **C** as the second cluster, the leaves of the node **D** as the third and finally the leaves of the node **E** as the fourth. In short, each node stands for a cluster whose members are the leaves of that node. The height of the nodes is proportional to the distance between its childs, i.e., the clusters that are merged at that level. For instance, the height of the node **A** is proportional to the distance between the clusters denoted by the nodes **B** and **C**. Observe that the cut need not to be straight. Although there exist sophisticated methods that give cuts at different levels; usually, the dendrogram is pruned at a fixed level to yield the desired number of clusters *C*.

APPENDIX C: INDEPENDENT COMPONENT ANALYSIS

We made use of [37, 38] in preparing the material presented in this part.

C.1. Description of the Independent Component Analysis

Independent component analysis (ICA) seeks directions of multivariate data that are mutually most independent. It is formalized by the following general definition.

ICA of a random vector **x** *consists of finding a linear transform* **s=Wx** *so that the components* s_i *are as independent as possible, in the sense of maximizing some function* $F(\mathbf{s})$ *that measures independence.*

If the dimensionality m of the observation vectors **x** matches the number of independent components n (i.e., dimensionality of the independent components vector **s**), the relation **s = Wx** can be inverted as **x = As**. The matrix **A** is said to be the mixing matrix, reciprocally the matrix **W** as the demixing matrix. The naming of these matrices follows from the classical example of ICA, where two people speaks in a room simultaneously and you record their speech with two microphones that, ideally, capture but only the mixture of their voices. You have two time signals $x_1(t)$ and $x_2(t)$ as measured by the two microphones. Can you recover the individual speech of both of these people, i.e., the source signals $s_1(t)$ and $s_2(t)$, by just making use of the observed signals $x_1(t)$ and $x_2(t)$? Using ICA, the answer is yes, if certain conditions are fulfilled. In the general case of m observed mixtures $x_j(t)$ and n sources $s_i(t)$, these conditions are stated as follows

(i) The instances of each of the observed mixtures $x_j(t)$, $t = 1,...,T$ must be independent identically distributed (i.i.d) in time.

(ii) All the indepenent components s_i, with the possible exception of one component, must be non-Gaussian.

(iii) The number of observed of observed mixtures m must be as large as the number of independent components n, i.e., $m \geq n$.

(iv) The matrix **A** must be of full column rank.

However, even if the above cited conditions are fulfilled, there are two ambiguities in identifying the columns of the mixing matrix **A**.

(i) The columns of **A** can be estimated up to a multiplicative constant. That is, we cannot recover the original intensity of the sources neither their sign.
(ii) The columns of **A** can be estimated up to a permutation. Hence ICA does not provide an ordering of the independent components.

Two elements are fundamental in solving the ICA problem: an objective function that measures independence (or a quantity negatively related to independence) and an optimization algorithm that maximizes (or minimizes) the objective function. Among the basic ICA methods, one can cite

- **ICA by maximizing non-Gaussianity.** Non-Gaussianity is related to independence by the *Central Limit Theorem* which basically states that the sum of i.i.d. random variables has the Gaussian distribution in the limiting case. Intuitively to say, if the generative linear mixture model holds for a set of observed mixtures, they must be "more" Gaussian than the underlying sources. Hence, ICA can be achieved equivalently by maximizing non-Gaussianity between the sources to be estimated. *Kurtosis* and *negentropy*-based methods exploit this knowledge.
- **ICA by maximum likelihood estimation.** It is possible to solve the ICA problem by classical maximum likelihood methods in case the distributions of the sources are of certain specific form with some parameters to be determined. These methods treat the problem in a semi-parametric way.
- **ICA by minimization of mutual information.** Mutual information is a natural measure of dependence between random variables, that vanishes if and only if the random variables are statistically independent. As a result, the minimization of mutual information constitutes another approach for solving the ICA problem.

In addition to these, in the literature, there exist other basic ICA methods that use higher-order cumulant information and concepts of non-linear decorrelation.

C.2. Applications of the Independent Component Analysis

The applications of ICA are certainly not limited to the working example of the previous section, which may be generalized under the name of blind source separation. Blind deconvolution is another signal processing problem that ICA methods have been found to work successfully in some cases. Furthermore, ICA has received a considerable interest in especially image feature extraction, as an alternative to classical principal component analysis (PCA). Low-level features of natural image data, extracted by ICA, have been shown to correspond closely to those observed in primary visual cortex. Texture analysis, biometric pattern recognition, image compression and watermarking constitute those applications that make use of ICA image features.

On the other hand, ICA is, first of all, an exploratory data analysis tool that can be benefited in applications where little prior knowledge about the underlying physical phenomena is available. Areas like astrophysics, biomedical signal processing, economics and social sciences possess a great deal of such applications.

C.3. The FastICA Algorithm

FastICA is a fast fixed-point ICA algorithm which is based on the maximization of a negentropy approximation. Specifically, FastICA maximizes the following objective function for finding one independent component

$$J(\mathbf{w}^T\mathbf{z}) \approx \left[E\{G(\mathbf{w}^T\mathbf{z})\} - E\{G(v)\}\right]^2 \tag{C.1}$$

where, $\mathbf{z}$ is the preprocessed version of the observed vector $\mathbf{x}$, $\mathbf{w}$ is one of the columns of the mixing matrix $\mathbf{W}$, v is a standard normal random variable and G is practically any non-quadratic function. Note that, $E\{.\}$ is computed by sample estimates. The following choices for G has been found to be very useful for robust approximations of negentropy

$$G_1(u) = \log\cosh u \quad \text{and} \quad G_2(u) = -\exp(-u^2/2) \tag{C.2}$$

The FastICA algorithm consists of a preprocessing and an optimization step details of which are given next.

C.3.1. Preprocessing

Preprocessing involves *centering* and *whitening*.

- **Centering.** We make the observed vectors zero-mean by subtracting the mean vector of the observations.

$$\tilde{\mathbf{x}} = \mathbf{x} - E\{\mathbf{x}\} \tag{C.3}$$

- **Whitening.** We transform $\tilde{\mathbf{x}}$ to $\mathbf{z}$ so that the covariance matrix of the latter becomes identity, i.e., $E\{\mathbf{z}\mathbf{z}^T\} = \mathbf{I}$. This can be achieved by first eigendecomposing $E\{\tilde{\mathbf{x}}\tilde{\mathbf{x}}^T\} = \mathbf{E}\mathbf{D}\mathbf{E}^T$ where $\mathbf{E}$ is the orthogonal matrix of eigenvectors and $\mathbf{D}$ is the diagonal matrix of eigenvalues of $E\{\tilde{\mathbf{x}}\tilde{\mathbf{x}}^T\}$. Then,

$$\mathbf{z} = \mathbf{E}\mathbf{D}^{-1/2}\mathbf{E}^T\tilde{\mathbf{x}} \tag{C.4}$$

Note that in case one would like to estimate fewer independent components than the observations such that $m \geq n$; only n columns, which are significant in terms of the eigenvalues, of the the transformation matrix $\mathbf{V} = \mathbf{E}\mathbf{D}^{-1/2}\mathbf{E}^T$ are involved in the computation of (C.4).

C.3.2. FastICA for Estimating One Independent Component

The FastICA algorithm can then be performed by the following procedure.

(1) Choose an initial random vector $\mathbf{w}$.

(2) $\mathbf{w} \leftarrow E\{\mathbf{z}G'(\mathbf{w}^T\mathbf{z})\} - E\{G''(\mathbf{w}^T\mathbf{z})\}\mathbf{w}$

(3) $\mathbf{w} \leftarrow \mathbf{w}/\|\mathbf{w}\|$

```
(4) If not converged, return to step (2).
```

where $\|\cdot\|$ denotes the Euclidean norm, G' and G'' are the first and second derivatives of G in which place one of the functions in (C.2) can be utilized.

C.3.3. FastICA for Estimating Multiple Components

In order to estimate several independent components, the above procedure should be repeated as many times as the number of independent components we want to estimate. To preclude convergence to the same maxima, the vectors $\mathbf{w}_1,\ldots,\mathbf{w}_n$ should be decorrelated at each step. This can be achieved in two ways.

- **Deflation-based decorrelation.** Let $\mathbf{w}_1,\ldots,\mathbf{w}_p$ be estimated by the above procedure, to remove the projections of $\mathbf{w}_1,\ldots,\mathbf{w}_p$ from the next estimated vectors $\mathbf{w}_p$, we perform the following

$$\begin{aligned}\mathbf{w}_{p+1} &\leftarrow \mathbf{w}_{p+1} - \sum_{j=1}^{p} \mathbf{w}_{p+1}^T \mathbf{w}_j \mathbf{w}_j \\ \mathbf{w}_{p+1} &\leftarrow \mathbf{w}_{p+1} \Big/ \left\|\mathbf{w}_{p+1}\right\|\end{aligned} \tag{C.5}$$

- **Symmetric decorrelation.** Decorrelation can equivalently be achieved in a simultaneous manner by

$$\mathbf{W} \leftarrow (\mathbf{W}\mathbf{W}^T)^{-1/2}\mathbf{W} \tag{C.6}$$

where $\mathbf{W}$ is the demixing matrix, as estimated at some step of the iterative procedure.

REFERENCES

1. Raichle, M. E., "Behind The Scenes of Functional Brain Imaging: A Historical and Physiological Perspective", *Proc. Natl. Acad. Sci.*, Vol. 95, pp. 765-772, 1998.

2. Emir, U. E., *System Characterization for a Fast Optical Imager*, M.S. Thesis, Boğaziçi University, 2003.

3. Frackowiak, R., P. J. Magistretti, R. Shulman, J. Altman and M. Adams (editors), *Neuroenergetics: Relevance for Functional Brain Imaging*, Human Frontier Science Program, Strasbourg, 2001.

4. Villringer, A. and B. Chance, "Non-Invasive Optical Spectroscopy and Imaging of Human Brain Function", *Trends in Neuroscience*, Vol. 20, pp. 4435-4442, 1997.

5. Strangman, G., D. Boas and J. Sutton, "Non-invasive Neuroimaging using Near-Infrared Light", *Society of Biological Psychiatry*, Vol. 17, pp. 679-693, 2002.

6. Schmidt, F. E. W., *Development of a Time-Resolved Optical Tomography System for Neonatal Brain Imaging*, Ph.D. thesis, University College London, 1999.

7. Boynton, G. M., S. A. Engel, G. H. Glover and D. J. Heeger, "Linear Systems Analysis of Functional Magnetic Resonance Imaging in Human V1", *The Journal of Neuroscience*, Vol. 16, pp. 4207-4221, 1996.

8. Strangman, G., J. P. Culver, J. H. Thompson and D. A. Boas, "A Quantitative Comparison of Simultaneous BOLD fMRI and NIRS Recordings during Functional Brain Activation", *NeuroImage,* Vol. 17, pp. 719-731, 2002.

9. Ciuciu, P., J-B. Poline, G. Marrelec, J. Idier, C. Pallier and H. Benali, "Unsupervised Robust Non-Parametric Estimation of the Hemodynamic Response Function for any

fMRI Experiment", *IEEE Trans. On Medical Imaging*, Vol. 22, No. 10, pp. 1235-1251, October 2003.

10. Friston, K. J., A. P. Holmes, K. J. Worsley, J-P. Poline, C. D. Frith and R. S. J. Frackowiak, "Statistical Parametric Maps in Functional Imaging: A General Linear Approach", *Human Brain Mapping*, Vol. 2, pp. 189-210, 1995.

11. Bandettini, P. A., A. Jesmanowicz, E. C. Wong and J. S. Hyde, "Processing Strategies for Time-Course Data Sets in Functional MRI of the Human Brain", *Magn. Reson. Med.*, Vol. 30, pp. 161-173, 1993.

12. Friston, K. J., P. Jezzard and R. Turner, "The Analysis of Functional MRI Time-Series", *Human Brain Mapping*, Vol. 1, pp. 153-171, 1995.

13. Worsley, K. J. and K. J. Friston, "Analysis Of fMRI Time-Series Revisited–Again", *NeuroImage*, Vol. 2, pp. 173-181, 1995.

14. Glover, G. H., "Deconvolution of Impulse Response in Event-Related BOLD fMRI", *NeuroImage*, Vol. 9, pp. 416-429, 1999.

15. Goutte, C., F. A. Nielsen and L. K. Hansen, "Modeling the Haemodynamic Response in fMRI using Smooth FIR Filters", *IEEE Trans. On Medical Imaging*, Vol. 19, pp. 1188-1201, 2000.

16. Marrelec, G., H. Benali, P. Ciuciu, M. Pélégrini-Issac and J-B. Poline, "Robust Bayesian Estimation of the Hemodynamic Response Function in Event-Related BOLD fMRI Using Basic Physiological Information", *Human Brain Mapping*, Vol. 19, pp. 1-17, 2003.

17. Ogawa, S., T. Lee, A. Kay and D. Tank, "Brain Magnetic Resonance Imaging with Contrast Dependent on Blood Oxygenation", *Proc. Natl. Acad. Sci. USA*, Vol. 87, no. 24, pp. 9868-9872, 1990.

18. Buxton, R. and L. Frank, "A Model for the Coupling between Cerebral Blood Flow and Oxygen Metabolism during Neural Stimulation", *J. Cereb. Blood Flow Metab.*, Vol. 17, No. 1, pp. 64-72, 1997.

19. Logothetis, N. K., J. Pauls, M. Augath, T. Trinath and A. Oeltermann, "Neurophysiological Investigation of the Basis of the fMRI Signal", *Nature*, Vol. 412, No. 6843, pp. 150-157, July 2001.

20. McCarthy, G., M. Luby, J. Gore and P. Goldman-Rakic, "Infrequent Events Transiently Activate Human Prefrontal and Pparietal Cortex as Measured by Functional MRI", *J. Neurophysiology*, Vol. 77, pp. 1630-1634, 1997.

21. Blanco, S., H. Garcia, R. Q. Quiroga, L. Romanelli and O. A. Rosso, "Stationarity of the EEG Series", *IEEE Engineering in Medicine and Biology Magazine*, Vol. 14, pp. 395-399, 1995.

22. Shanmugan, K. S. and A. M. Breipohl, *Random Signals: Detection, Estimation and Data Analysis*, John Wiley & Sons, 1988.

23. D'Agostino, R. B., "Tests for the Normal Distribution", in R. B. D'Agostino and M. A. Stephens (eds.), *Goodness of Fit Techniques*, pp. 367-419, Marcel Dekker, New York, 1986.

24. Bai, J. and S. Ng, "Tests for Skewness, Kurtosis and Normality for Time-series Data", *Boston College Working Papers in Economics*, 501, June 2001.

25. Hinich, M. J., "Testing for Gaussianity and Linearity of a Stationary Time-Series", *Journal of Time-Series Analysis*, Vol. 3, pp. 169-176, 1982.

26. D'Agostino, R. B., "Graphical Analysis", in R. B. D'Agostino and M. A. Stephens (eds.), *Goodness of Fit Techniques*, pp. 7-62, Marcel Dekker, New York, 1986.

27. Stephens, M. A., "Tests for the Uniform Distribution", in R. B. D'Agostino and M. A. Stephens (eds.), *Goodness of Fit Techniques*, pp. 357-360, Marcel Dekker, New York, 1986.

28. Blanco, S., R. Q. Quiroga, O. A. Rosso and S. Kochen, "Time-Frequency Analysis of Electroencephalogram Series", *Physical Review E* , Vol. 51, pp. 2624-2631, March 1995.

29. Başar, E., T. Demiralp, M. Schurmann, C. Başar-Eroğlu and A. Ademoğlu, "Oscillatory Brain Dynamics, Wavelet Analysis and Cognition", *Brain and Language*, Vol. 66, pp. 146-183, 1999.

30. Obrig, H., M. Neufang, R. Wenzel, M. Kohl, J. Steinbrink, K. Einhaupl and A. Villringer, "Spontaneous Low Frequency Oscillations of Cerebral Hemodynamics and Metabolism in Human Adults", *NeuroImage*, Vol. 12, pp. 623-639, 2000.

31. Kim, D. and K. Uğurbil, "Bridging the Gap between Neuroimaging and Neuronal Physiology", *Image Anal. Stereol.*, Vol. 21, pp. 97-105, 2002.

32. Stoica, P. and R. L. Moses, *Introduction to Spectral Analysis*, p. 43, Prentice Hall, Upple-Saddle River, New Jersey, 1997.

33. Kuo, T., C. Chern, W. Sheng, W. Wong and H. Hu, "Frequency Domain Analysis of Cerebral Blood Flow Velocity and its Correlation with Arterial Blood Pressure", *J. Cereb. Blood Flow Metab.*, Vol. 18, pp. 311-318, 1998.

34. Giller, A. C., M. R. Hatab and A. M. Giller, "Oscillations in Cerebral Blood Flow Detected with a Transcranial Doppler Index", *J. Cereb. Blood Flow Metab.*, Vol. 19, pp. 452-459, 1999.

35. Hu, H., T. Kuo, W. Wong, Y. Luk, C. Chern, L. Hsu and W. Sheng, "Transfer Function Analysis of Cerebral Hemodynamics in Patients with Carotid Stenosis", *J. Cereb. Blood Flow Metab.*, Vol. 19, pp. 460-465, 1999.

36. Friedman, D.H., "Pseudo-Maximum-Likelihood Speech Pitch Extraction", *IEEE Trans. on ASSP*, Vol. 25, pp. 213-221, 1977.

37. Hyvärinen, A., J. Karhunen and E. Oja, *Independent Component Analysis*, John Wiley & Sons, 2001.

38. Duda, R. O., P. E. Hart and D. G. Stork, *Pattern Classification*, John Wiley & Sons, 2001.

39. Ferraty, F. and P. Vieu, "Curves Discrimination: a Nonparametric Functional Approach", *Computational Statistics and Data Analysis*, Vol. 44, pp. 161-173, 2003.

40. Unser, M., A. Aldroubi and M. Eden, "B-Spline Signal Processing: Part II-Efficient Design and Applications", IEEE Trans. on Signal Processing, Vol. 41, pp. 834-848, February 1993.

41. Vesanto, J. and E. Alhoniemi, "Clustering of the Self-Organizing Map", *IEEE Transactions on Neural Networks*, Vol. 11, pp. 586-600, 2000.

42. Davies, D. L. and D. W. Bouldin, "A Cluster Separation Measure", *IEEE Trans. on Pattern Analysis Machine Intelligence*, vol. PAMI-1, pp. 224-227, April 1979.

43. Bezdek, J. C. , "Some New Indexes of Cluster Validity", *IEEE Trans. on Syst., Man, Cybernetics*, Part B, Vol. 28, pp. 301-315, 1998.

44. Milligan, G. W. and M. C. Cooper, "An Examination of Procedures for Determining the Number of Clusters in a Data Set", *Psychometrika*, Vol. 50, pp. 159-179, June 1985.

45. Cordes, D., V. M. Haughton, K. Arfanakis, J. D. Carew, P. A. Turski, C. H. Moritz, M. A. Quigley and M. E. Meyerand, "Frequencies Contributing to Functional Connectivity

in the Cerebral Cortex in Resting-State Data", *Am. J. Neuroradiology*, Vol. 22, pp. 1326-1333, 2001.

46. Blanco, S., A. Figliola, R. Q. Quiroga, O. A. Rosso and E. Serrano, "Time-Frequency Analysis of Electroencephalogram Series. III. Wavelet Packets and Information Cost Function", *Physical Review E* , Vol. 57, pp. 932-940, January 1998.

47. Kohonen, T., *Self-Organizing Maps*, Springer-Verlag, Berlin, 1995.

48. Meng, X-L. and D. B. Rubin, "Maximum Likelihood Estimation via the ECM Algorithm: A General Framework", *Biometrika*, Vol. 80, pp. 267-278, 1993.

49. Haykin, S., *Adaptive Filter Theory*, Prentice Hall, Upple-Saddle River, New Jersey, 2002.

50. Djuric, P. M., J. H. Katecha, J. Zhang, Y. Huang, T. Ghirmai, M. Bugallo and J. Miguez, "Particle Filtering", *IEEE Signal Processing Magazine*, Vol. 20, pp. 19-38, September 2003.

51. Wang, Y. M. , R. T. Schultz, R. T. Constable and L. H. Staib, "Nonlinear Estimation and Modeling of fMRI Data using Spatio-Temporal Support Vector Regression", *Information Processing in Medical Imaging*, pp. 647 - 659, Ambleside, UK, July 2003.

52. Wang, Y. M., R. T. Schultz, R. T. Constable and L. H. Staib, "A Unified Framework for Nonlinear Analysis of Functional MRI Data using Support Vector Regression", *Human Brain Mapping*, New York, USA, June 2003.

53. Liu, T. T., L. R. Frank, E. C. Wong and R. B. Buxton, "Detection Power, Estimation Efficiency and Predictability in Event-Related fMRI", *NeuroImage*, Vol. 13, pp. 759-773, 2001.